

Dissertation  
submitted to the  
Combined Faculties for the Natural Sciences and for Mathematics  
of the Ruperto-Carola University of Heidelberg, Germany  
for the degree of  
Doctor of Natural Sciences

put forward by  
**Dipl. Phys. Felix Friedl**  
born in  
**Freiburg im Breisgau**

day of oral exam: February, 6th 2013



**Investigating the Transfer of Oxygen  
at the Wavy Air-Water Interface  
under Wind-Induced Turbulence**

**Referees: Prof. Dr. Bernd Jähne  
Prof. Dr. Ulrich Platt**



## Abstract

Local oxygen ( $O_2$ ) transfer velocities measured in a linear wind-wave tunnel with respect to wind speed and fetch are presented in this thesis. For this, a non-intrusive laser-induced fluorescence (LIF) method was developed to measure vertical  $O_2$  concentration profiles in the water-sided mass boundary layer. The fluorophore used is a water soluble ruthenium complex, which is quenched according to the Stern-Volmer equation. This equation, which originally describes the quenching only for a weak excitation, was generalized for arbitrary laser irradiance. Measurements confirm this generalization and yield a new value for the Stern-Volmer constant.

The LIF method was applied with high spatial and temporal resolution of  $6.2\ \mu\text{m}$  and  $1.2\ \text{kHz}$ , respectively, in order to resolve the mass boundary layer and fast processes. To obtain mean  $O_2$  concentration profiles with high precision, an algorithm was developed to detect the water surface in the recorded images. The measured mean concentration profiles show a transition in the self-similar shape with the onset of waves. The results for a flat water surface are in agreement with the surface renewal model. For a wavy water surface, the small eddy model and the surface renewal model both describe the data equally well. Vanishing  $O_2$  concentration fluctuations at the flat water surface were measured, which is in agreement with existing models for a rigid interface. The local transfer velocities obtained from mean concentration profiles are best parametrized with the friction velocity. In this work, the great potential of LIF measurements to probe transfer velocities locally is demonstrated.

## Zusammenfassung

Lokale Transfergeschwindigkeiten von Sauerstoff ( $O_2$ ), die in Abhängigkeit von der Windgeschwindigkeit und der Windwirklänge in einem linearen Wind-Wellen Kanal gemessen wurden, werden in dieser Arbeit präsentiert. Dazu wurde eine berührungsfreie laserinduzierte Fluoreszenz (LIF) Methode entwickelt, um vertikale  $O_2$  Konzentrationsprofile in der wasserseitigen Massengrenzschicht zu messen. Der verwendete Farbstoff ist ein wasserlöslicher Ruthenium Komplex, dessen Quenchverhalten durch die Stern-Volmer Gleichung beschrieben wird. Diese Gleichung, die ursprünglich das Quenchen nur für eine schwache Anregung beschreibt, wurde für beliebige Laser Bestrahlungsstärken verallgemeinert. Messungen bestätigen die Verallgemeinerung und ergeben einen neuen Wert für die Stern-Volmer Konstante.

Die LIF Methode wurde mit einer hohen räumlichen und zeitlichen Auflösung von  $6.2\ \mu\text{m}$  und  $1.2\ \text{kHz}$  angewendet, um die Massengrenzschicht und schnelle Prozesse auflösen zu können. Um mittlere Konzentrationsprofile mit einer hohen Präzision zu erhalten, wurde ein Algorithmus entwickelt, der die Wasseroberfläche in den aufgenommenen Bildern detektiert. Die mittleren Konzentrationsprofile weisen einen Übergang in ihrer selbstähnlichen Form mit dem Einsetzen von Wellen auf. Die Ergebnisse für eine flache Wasseroberfläche stimmen mit dem Oberflächenenerneuerungsmodell überein. Für eine wellige Wasseroberfläche werden die Daten von dem Oberflächenenerneuerungsmodell und dem Diffusionsmodell gleich gut beschrieben. An der flachen Wasseroberfläche wurden verschwindend geringe Konzentrationsfluktuationen gemessen, was mit gängigen Modellvorhersagen für eine starre Grenzfläche in Einklang ist. Die lokalen Transfergeschwindigkeiten, ermittelt durch mittlere Konzentrationsprofile, werden am besten durch die Schubspannungsgeschwindigkeit parametrisiert. Diese Arbeit zeigt die großen Möglichkeiten von lokalen LIF Messungen auf, um lokale Transfergeschwindigkeiten zu bestimmen.



# Contents

<b>1. Introduction</b>	<b>1</b>
<b>2. Theory</b>	<b>5</b>
2.1. Theory of Gas and Momentum Transfer . . . . .	5
2.1.1. Molecular and Turbulent Diffusion . . . . .	5
2.1.2. Gas Exchange Parameters . . . . .	7
2.1.3. Wind Profiles . . . . .	10
2.2. Gas Exchange Models . . . . .	11
2.2.1. Film Model . . . . .	11
2.2.2. Small Eddy Model . . . . .	12
2.2.3. Surface Renewal Model . . . . .	14
2.2.4. Model for Fluctuation Concentration Profiles . . . . .	16
2.2.5. The Deacon Model . . . . .	18
2.3. Luminescence Theory . . . . .	19
2.3.1. Introduction to Luminescence . . . . .	19
2.3.2. The MLCT Process . . . . .	21
2.3.3. Weak and Strong Excitation . . . . .	23
2.3.4. Quenching . . . . .	23
<b>3. Methods</b>	<b>29</b>
3.1. Oxygen Concentration Imaging . . . . .	29
3.1.1. Oxygen Quenching Method . . . . .	29
3.1.2. Constraint for the Laser Operation Mode . . . . .	30
3.1.3. Effects Influencing the Precision . . . . .	31
3.2. Calibration Method for the LIF Measurements . . . . .	32
3.2.1. Adjusting and Measuring the Oxygen Concentration . . . . .	32
3.2.2. Determination of the Damping Factor . . . . .	32
3.2.3. Determination of the Unquenched Photon Flux . . . . .	34
3.3. Mass Balance Method . . . . .	35
3.4. Measuring Method for the Wind Profiles . . . . .	36

<b>4. Setup</b>	<b>37</b>
4.1. The Wind-Wave Tunnels . . . . .	37
4.1.1. The Heidelberg Linear Wind-Wave Tunnel . . . . .	37
4.1.2. The Test Wind-Wave Tunnel . . . . .	42
4.2. The LIF Setup . . . . .	43
4.2.1. General Description . . . . .	43
4.2.2. The Laser . . . . .	46
4.2.3. The Beam Expander . . . . .	47
4.2.4. The Camera . . . . .	48
4.2.5. The Camera Lens . . . . .	49
<b>5. Characterization of the Ruthenium Complex Indicator</b>	<b>51</b>
5.1. General Properties . . . . .	51
5.2. Quenching Characteristics . . . . .	53
5.2.1. Measurement of the Damping Factor $\epsilon_D$ . . . . .	53
5.2.2. Measurement of the Stern-Volmer Constant . . . . .	57
5.2.3. Measurement of the Temperature Dependence of the Stern-Volmer Constant . . . . .	60
5.3. Photobleaching Test . . . . .	63
<b>6. Calibration</b>	<b>67</b>
6.1. Calibration of the Optical Setup . . . . .	67
6.1.1. Magnification of the Optical System . . . . .	67
6.1.2. Image Sharpness . . . . .	68
6.2. Calibration of the LIF Saturation . . . . .	70
6.3. Calibration of the LIF Signal in Absence of Oxygen . . . . .	71
<b>7. Experiments</b>	<b>73</b>
7.1. Preparatory Experiments . . . . .	73
7.2. Measurement of Forcing Parameters . . . . .	74
7.2.1. Wind Speed and Friction Velocity . . . . .	74
7.2.2. Wave Measurements . . . . .	76
7.3. Gas Exchange Experiments . . . . .	76
7.3.1. LIF Measurements . . . . .	77
7.3.2. Bulk Measurements . . . . .	78
<b>8. Data Processing</b>	<b>79</b>
8.1. Processing of the Wind Profiles . . . . .	79
8.1.1. Wind Profiles in Dimensionless Coordinates . . . . .	79
8.1.2. Determination of the Friction Velocity . . . . .	80

8.2. Processing of the LIF Data . . . . .	82
8.2.1. Calculation of the Oxygen Concentration . . . . .	83
8.2.2. Detection of the Water Surface . . . . .	86
8.2.3. Calculating Mean Concentration Profiles . . . . .	90
8.2.4. Determination of the Boundary Layer Thickness . . . . .	91
8.3. Processing of the Bulk Measurements . . . . .	93
<b>9. Results</b>	<b>95</b>
9.1. Wind and Fetch Dependence of the Friction Velocity . . . . .	95
9.2. Oxygen Concentration Images . . . . .	97
9.3. Results of the Surface Detection Algorithm . . . . .	100
9.4. Mean Oxygen Concentration Profiles . . . . .	101
9.4.1. Fit of the Models to the Data . . . . .	102
9.4.2. Scaling with the Models . . . . .	104
9.5. Fluctuation Concentration Profiles . . . . .	106
9.5.1. Additional Contributions to the Variance . . . . .	108
9.5.2. Fluctuations at a Flat Water Surface . . . . .	108
9.5.3. Fluctuations at a Wavy Water Surface . . . . .	109
9.6. Oxygen Transfer Rates . . . . .	109
9.6.1. Thickness of the Mass Boundary Layer . . . . .	110
9.6.2. Comparison with Mass Balance Measurements . . . . .	110
9.6.3. Parametrizations of the Transfer Velocity . . . . .	111
<b>10. Conclusion and Outlook</b>	<b>115</b>
10.1. Conclusion . . . . .	115
10.2. Outlook . . . . .	117
<b>Bibliography</b>	<b>118</b>
<b>A. Appendix</b>	<b>125</b>
A.1. Synthesis of the Ru Complex . . . . .	125
A.2. The Damping Factor $\epsilon_D$ - Alternative Notation . . . . .	126
A.3. Stern-Volmer Plot - Further Presentation . . . . .	127
A.4. Unforeseen Effects of the Camera . . . . .	127
A.4.1. Two-Level Noise Effect . . . . .	127
A.4.2. Sawtooth Effect . . . . .	128
A.5. Camera Response Calibration . . . . .	129



# 1. Introduction

Gas exchange between the ocean and the atmosphere is an essential component to understand and predict climate on Earth. Constituting a huge reservoir, the ocean acts as a net sink for carbon by taking up 30 % to 40 % of the fossil fuel-produced CO<sub>2</sub> [Donelan and Wanninkhof, 2002]. For over thirty years of gas exchange research it is still unclear which physically-based model gives the best description of the exchange process at the air-water interface for a smooth and wavy water surface. One way to approach this question is to measure the vertical concentration profile in the tiny (smaller than 100 μm) mass boundary layer at the air-water interface. The objective of this thesis is therefore to develop a method to visualize profiles of the oxygen concentration within the top millimeter at the wavy water surface with high precision.

The exchange of gases at the ocean surface is influenced by the interaction of multiple factors. Wind blowing over the water's surface greatly enhances the air-water gas transfer velocity. This growth is associated with shear stress that increases the near-surface turbulence and leads to a decreasing mass boundary layer. The transfer velocity is further enhanced by the generation of waves, leading to an enlarged water surface, breaking waves and bubble entrainment (see e.g. [Wanninkhof et al., 2009]). Semi-empirical relations of the transfer velocity with wind speed are still used as parametrizations in climate models [Ho et al., 2011]. Figure 1.1 shows results from gas exchange experiments performed in the North Sea, the North Atlantic, the Equatorial Pacific, and the Southern Ocean, to name just a few. In this figure, the parametrization with wind speed shows significant variations of the measured transfer velocities. By plotting transfer velocities against wind speed, effects such as surface films and fetch<sup>1</sup> are not taken into account. Additional forcing parameters aside from the wind speed that influence gas transfer include the surface roughness and the friction velocity, which are both more closely related to the turbulence in the water than to the wind speed.

Experiments on the ocean are demanding because of high temporal and spatial variability of the wind speed and the wave field. Not all forcing parameters can be measured on the ocean and the accessible parameters cannot all be measured instantaneously at the same location. However, this is achievable in laboratories using wind-wave tunnels. At low wind speeds, the gas exchange is controlled by effects on small scales that can be examined in a wind-wave tunnel.

Another method to approach the questions in air-sea gas exchange is by using physically-based models describing the exchange mechanisms in the air-water boundary layer. Existing gas

---

<sup>1</sup>fetch: distance over which the wind acts on the water surface

## 1. Introduction

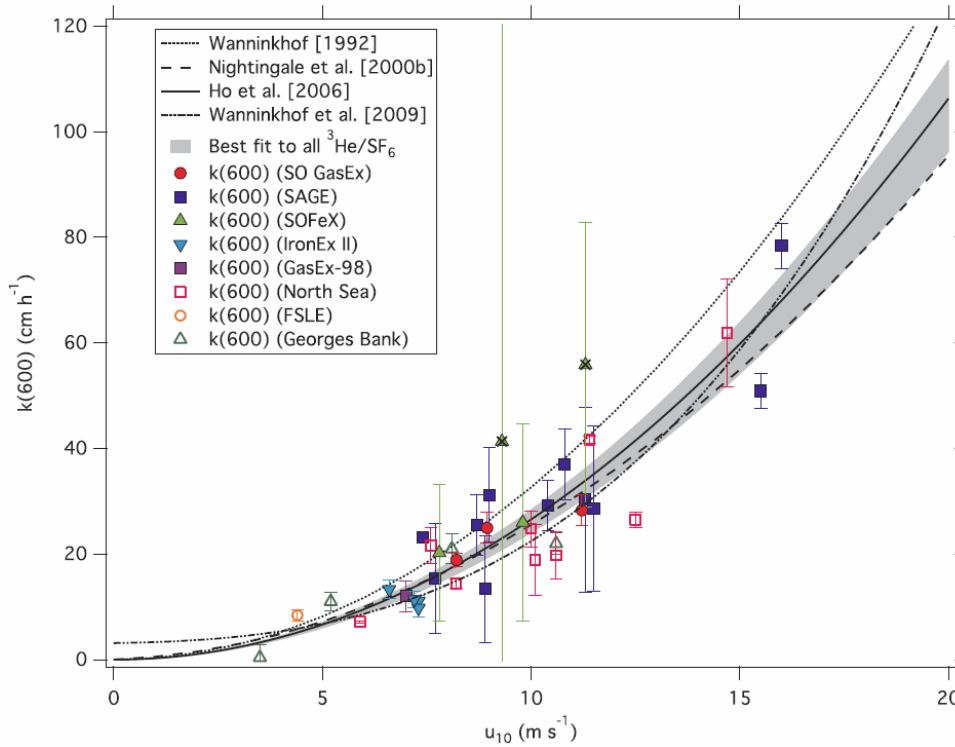


**Figure 1.1.:** Transfer velocities  $k$ , normalized to a Schmidt number of 600, plotted against wind speed. The open symbols are for the experiments in the coastal oceans, while the solid symbols depict the studies in the open ocean. From Ho et al. [2011].

exchange models describe the gas exchange mechanisms for a flat and a wavy water surface. The underlying assumptions on the physical mechanisms are contradictory. Local measurements of vertical concentration profiles in the mass boundary layer can be used to test the models. The first precise measurements of mean concentration profiles at a flat water surface were conducted by Münsterer and Jähne [1998]. They found that the profiles are best described by the surface renewal model for a rigid interface (see Figure 1.2).

The goal of this study is to develop and apply a method to perform measurements of vertical concentration profiles of oxygen with an improved sensitivity and a higher temporal and spatial resolution compared to previous studies. With the data obtained, gas transfer models are tested. In addition, the local transfer velocity as well as forcing parameters such as friction velocity, mean square slope, and wind speed are measured in a wind-wave tunnel for various fetch and wind speed combinations.

Chapter 2 comprises the basic principles that are important in this work and makes a step beyond current knowledge regarding the quenching mechanism. In Chapter 3, the technique to visualize oxygen in water with a laser-induced fluorescence (LIF) method and a new calibration method are presented. The third part of the chapter introduces the mass balance method, needed for the validation of the oxygen quenching technique. The method to measure wind profiles is shown in the last part of this chapter. Chapter 4 presents the experimental setup of

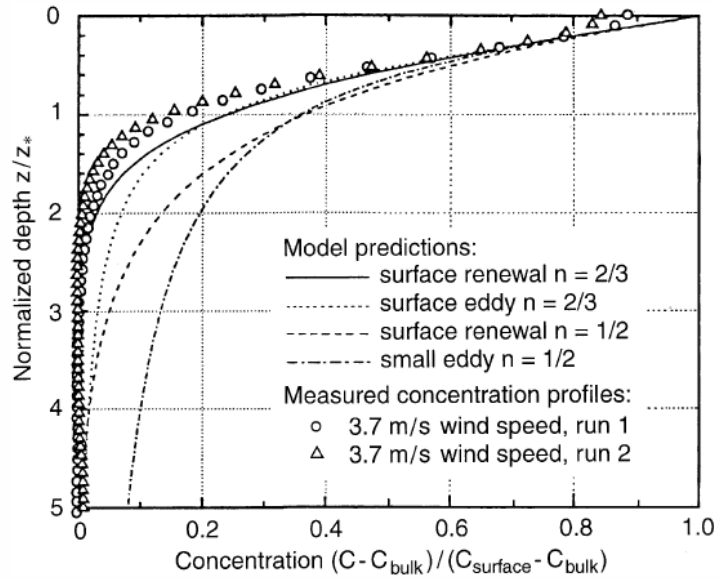


**Figure 1.2.:** Comparison of mean concentration profiles measured with fluorescein with the predictions by the small eddy and the surface renewal model. From [Münsterer and Jähne, 1998].

two wind-wave tunnels and the optical setup. Measurements to confirm the generalization of the Stern-Volmer equation are presented in Chapter 5. The calibration of the optical setup and of laser saturation effects by applying the new calibration method is illustrated in Chapter 6. Chapter 7 presents the experiments that were conducted in this study, including preparatory experiments, measurements of the forcing parameters friction velocity and mean square slope, and the main gas exchange experiments. The data processing for the wind measurements, the LIF measurements, and the mass balance method is shown in Chapter 8. Finally, Chapter 9 presents the results of the oxygen visualization, tests of models, and parametrizations of the local gas transfer velocities. Chapter 10 comprises the conclusion of the obtained results and ends with a short outlook on future experiments.



## 2. Theory

The theory is divided into three parts. Section 2.1 gives an introduction into the theory of gas and momentum exchange at the air-water interface. Section 2.2 presents model predictions for gas concentration profiles. Additionally, a model developed in this thesis to calculate fluctuation concentration profiles is shown. Section 2.3 gives a summary of the basic processes of luminescence theory. The generalization of the Stern-Volmer equation is shown in Section 2.3.4.

### 2.1. Theory of Gas and Momentum Transfer

To give an introduction into the theory of gas and momentum transfer, Section 2.1.1 gives a mathematical description of molecular and turbulent transport. Section 2.1.2 introduces the gas exchange parameters, that are needed in this study. In Section 2.1.3, wind profiles near a wall in different regions are presented.

#### 2.1.1. Molecular and Turbulent Diffusion

The gas exchange at the air-water interface is dominated by two transport mechanisms: molecular diffusion and turbulent transport. The molecular diffusion is due to the Brownian motion of the molecules, while the turbulent transport is driven by statistical fluctuations of the velocity field. Far from the air-water interface, the transport processes are governed by turbulent transport, because the length scale of the turbulent eddies is much larger than the mean free path of the molecules. The length scale of the turbulent eddies scales with the distance to the interface. Therefore, the eddy size decreases with decreasing distance to the air-water interface. Close to the interface, the molecular diffusion exceeds the turbulent transport. This shows that we have to consider both transport mechanisms to understand the gas exchange processes at an interface. The macroscopic diffusive transport for an ensemble is described with Fick's first law

$$\vec{j}_c = -D\nabla c. \quad (2.1)$$

The proportionality constant  $D$  between the concentration gradient  $\nabla c$  and the concentration flux density  $j_c$  is the Diffusion constant. In analogy to the transport of a concentration  $c$ , momentum transport is described with a similar equation

$$\vec{j}_m = -\nu\nabla(\rho\vec{u}), \quad (2.2)$$

## 2. Theory

with the momentum flux density  $j_m$ , the kinematic viscosity  $\nu$ , the density of the medium  $\rho$ , and the velocity field  $\vec{u}$ .

Using Fick's second law and the material derivative, we obtain the transport equation for the concentration  $c$

$$\frac{\partial c}{\partial t} + \vec{u} \cdot \nabla c = D \Delta c. \quad (2.3)$$

The advective term  $\vec{u} \cdot \nabla c$  includes the transport of the concentration by the velocity field  $\vec{u}$ . To solve equation (2.3), the velocity field  $\vec{u}$  has to be known. The transport equation for the momentum is given by the Navier-Stokes equation for incompressible media [Roedel, 2000]

$$\frac{\partial \vec{u}}{\partial t} + (\vec{u} \cdot \nabla) \vec{u} = -\frac{1}{\rho} \nabla p + \vec{f} + \nu \Delta \vec{u}. \quad (2.4)$$

An acceleration of the fluid is caused by pressure gradients  $\nabla p$ , external forces (expressed by the acceleration  $\vec{f}$ ), and shear forces. Assuming no external forces and no pressure gradients

$$\frac{\partial \vec{u}}{\partial t} + (\vec{u} \cdot \nabla) \vec{u} = \nu \Delta \vec{u}, \quad (2.5)$$

we obtain an analogue transport equation for momentum as equation (2.3) for the concentration.

**Reynolds Decomposition** In the following, it will be shown that the turbulent transport can be treated analogous to the diffusive transport. Using Reynolds decomposition, we split the concentration  $c$  and the velocity  $\vec{u}$  into an averaged and a fluctuating part:

$$c = \bar{c} + c' \quad (2.6)$$

$$\vec{u} = \bar{\vec{u}} + \vec{u}' \quad (2.7)$$

By inserting those expressions into the transport equations (2.3) and (2.5) for concentration and momentum, and assuming a stationary, one-dimensional current in  $x$ -direction, we obtain the following differential equations

$$\frac{\partial \bar{c}}{\partial t} = \frac{\partial}{\partial z} \left( D \frac{\partial \bar{c}}{\partial z} - \overline{c' w'} \right) \quad (2.8)$$

$$\frac{\partial \bar{u}}{\partial t} = \frac{\partial}{\partial z} \left( \nu \frac{\partial \bar{u}}{\partial z} - \overline{u' w'} \right) \quad (2.9)$$

with  $u$  and  $w$  denoting the velocity components in stream-wise ( $x$ -) direction and vertical ( $z$ -) direction, respectively (see Figure 4.4). Equation (2.9) is called the Reynolds equation (for the derivation see [Pope, 2009]). Using the equation of continuity and integrating equations (2.8) and (2.9), we obtain a constant scalar flux density for the concentration  $j_c$  and for the momentum  $j_m$ :

$$j_c = -D \frac{\partial \bar{c}}{\partial z} + \overline{c' w'} \quad (2.10)$$

$$j_m = \rho \left( -\nu \frac{\partial \bar{u}}{\partial z} + \overline{u' w'} \right) \quad (2.11)$$

The term  $\rho \overline{u' w'}$  in equation (2.11) is known as the Reynolds stress. A comparison of equations (2.10) and (2.11) with the equations (2.1) and (2.2) for the flux density including only diffusive transport implies that the terms  $\overline{c' w'}$  and  $\overline{u' w'}$  are a measure for the turbulent transport. This gives rise to the definition of a turbulent diffusivity  $K_c$  and a turbulent viscosity  $K_m$ :

$$\overline{c' w'} = -K_c \frac{\partial \bar{c}}{\partial z} \quad (2.12)$$

$$\overline{u' w'} = -K_m \frac{\partial \bar{u}}{\partial z} \quad (2.13)$$

Inserting those expressions into equations (2.10) and (2.11), we obtain equations for the transport mechanism of concentrations and momentum including a diffusive and a turbulent part:

$$j_c = -(D + K_c(z)) \frac{\partial \bar{c}}{\partial z} \quad (2.14)$$

$$j_m = -(\nu + K_m(z)) \frac{\partial \bar{u}}{\partial z} \quad (2.15)$$

### 2.1.2. Gas Exchange Parameters

**Transfer Rate** The flux density  $j_c$  is proportional to the concentration difference  $\Delta c$ . The proportionality constant is the transfer velocity  $k$ .

$$j_c = k \cdot \Delta c \quad (2.16)$$

Integrating equation (2.14) and assuming a constant flux density  $j_c$ , we obtain

$$c(z_2) - c(z_1) = -j_c \int_{z_1}^{z_2} \frac{1}{D + K_c(z)} dz. \quad (2.17)$$

By using equation (2.16), we get the following result for the transfer velocity for the range between depth  $z_1$  and  $z_2$ :

$$k = \frac{1}{\int_{z_1}^{z_2} (K_c(z) + D)^{-1} dz}. \quad (2.18)$$

The only unknown variable for the determination of the transfer velocity  $k$  is the depth dependence of the turbulent diffusivity  $K_c(z)$ . The inverse quantity of the transfer velocity is the transfer resistance  $R$ .

$$R = k^{-1} \quad (2.19)$$

## 2. Theory

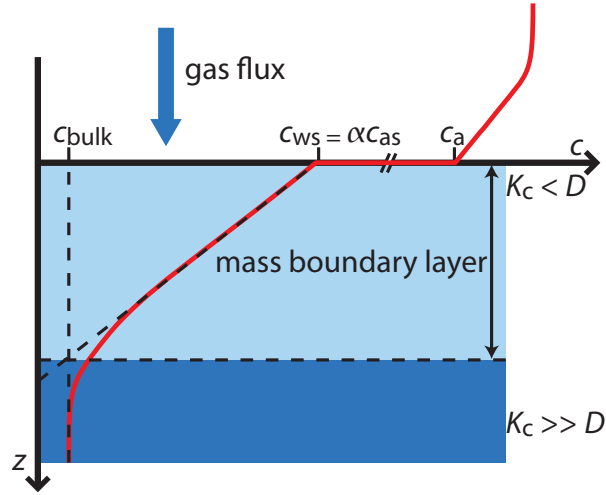


**Figure 2.1.:** Sketch of a concentration profile near the air-water interface for a gas with a low solubility ( $\alpha < 1$ ) during an invasion experiment.

It is often useful to use the transfer resistance  $R$ , because the resistances  $R_i$  of different depth layers sum up to the total resistance, in analogy to the resistances in a serial circuit. The total resistance  $R$  for the exchange process at the air-water interface is partitioned in an air-sided and water-sided resistance (see Kräuter [2011] for more details).

Figure 2.1 shows a concentration profile for the case that the concentration in the air is higher than in the water (an invasion experiment). The concentration at the air-water interface shows a discontinuity and is in thermodynamic equilibrium. According to Henry's law, the ratio of the concentration  $c_{ws}$  and  $c_{as}$  at the water-side and the air-side of the surface, respectively, is specified with the dimensionless solubility  $\alpha$ :

$$c_{ws} = \alpha \cdot c_{as} \quad (2.20)$$

The solubility of oxygen, which is used as a trace gas in this study is about  $\alpha = 0.03$  [Sander, 1999]. This implies that the air-sided resistance of  $O_2$  can be neglected and the total resistance is given by the water-sided resistance.

**Mass Boundary Layer** The thickness of the aqueous mass boundary layer is defined by the ratio of the concentration difference between the water bulk and the water surface and the gradient of the concentration at the water surface.

$$\delta_{mbl} = \frac{\Delta c}{-\left. \frac{\partial c}{\partial z} \right|_{z=0}} \quad (2.21)$$

A graphical description of the thickness  $\delta_{mbl}$  is given in Figure 2.1. The turbulent diffusivity  $K_c$  depends on the depth  $z$  and becomes zero at the interface due to the hydrodynamic boundary

conditions (see [Coantic, 1986]). Using equation (2.14), we obtain for the flux density

$$j_c = -D \left. \frac{\partial \bar{c}}{\partial z} \right|_{z=0}. \quad (2.22)$$

With that expression and equation (2.16), it follows that the thickness of the aqueous mass boundary layer  $\delta_{\text{mbl}}$  is proportional to the inverse transfer velocity.

$$\delta_{\text{mbl}} = \frac{D}{k} \quad (2.23)$$

The characteristic time  $t_*$  that a molecule needs to traverse the mass boundary layer is defined by

$$t_* = \frac{\delta_{\text{mbl}}}{k}. \quad (2.24)$$

**Schmidt Number** The Schmidt number  $Sc$  is a dimensionless quantity that relates gas transfer to momentum transfer.

$$Sc = \frac{\nu}{D} \quad (2.25)$$

Schmidt numbers in the air are about 1. In the water, Schmidt numbers are much bigger and cover a range from values below 100 to values higher than 2000 Jähne [1980]. The Schmidt number of  $\text{O}_2$  at  $20^\circ\text{C}$  in clean water is about  $Sc = 481$ . This value was calculated with the values for the diffusion constant and the viscosity from [Cussler, 2009] and [Yaws, 1999].

Momentum and concentrations are transported by the same fluctuations Jähne [1980]. As a consequence, the turbulent Schmidt number, which is given by the ratio of the turbulent viscosity  $K_m$  and the turbulent diffusivity  $K_c$

$$Sc_t = \frac{K_m}{K_c} \quad (2.26)$$

is on the order of 1.

**Friction Velocity** The shear stress  $\tau$  is equal to the momentum flux density  $j_m$  in equation (2.11) and thus the friction velocity  $u_*$  is defined by the following relation

$$u_* = \sqrt{\frac{|\tau|}{\rho}}. \quad (2.27)$$

It is a measure for vertical momentum transfer, that is transported into the water due to wind-induced shear stress  $\tau$ . Assuming a continuous momentum flux at the air-water interface, which implies no momentum loss due to the creation of waves, we obtain the following relation between the water-sided and the air-sided friction velocity  $u_{*w}$  and  $u_{*a}$ :

$$\rho_w u_{*w}^2 = \rho_a u_{*a}^2, \quad (2.28)$$

## 2. Theory

with the density of water and air  $\rho_w$  and  $\rho_a$ , respectively. It follows that the water-sided friction velocity  $u_{*w}$  is about a factor of 30 smaller than the air-sided friction velocity. In this text, the notation  $u_*$  is used for the air-sided friction velocity, as the friction velocity was measured on the air-side in this study.

### 2.1.3. Wind Profiles

The turbulent flow region near a wall is typically classified in three layers.

**Viscous Sublayer** In the viscous sublayer or the buffer region next to the wall, the Reynolds stress  $\rho \overline{u' w'}$  in equation (2.11) can be neglected.

$$\tau = \rho \nu \frac{\partial u}{\partial z} \quad (2.29)$$

The right hand side is positive because the  $z$ -axis points upwards and is opposite to the definition used in equation (2.11). This convention is used for the wind-profiles presented in this study. Integrating equation (2.29) leads to a linear wind profile in the viscous sublayer:

$$u(z) \propto z \quad (2.30)$$

**Fully-Turbulent Flow Region** In the fully-turbulent flow region, the shear stress is equal to the Reynolds stress, as the viscous contribution to the shear stress can be neglected:

$$\tau = \rho \overline{u' w'} \quad (2.31)$$

The friction velocity is accordingly given with the correlations of the velocity fluctuations.

$$u_* = \sqrt{\overline{u' w'}} \quad (2.32)$$

The wind profile in the fully-turbulent region has a logarithmic form

$$u(z) = \frac{u_*}{\kappa} \cdot \ln\left(\frac{z}{z_0}\right), \quad (2.33)$$

with the universal Von Kármán constant<sup>1</sup>  $\kappa$  and the roughness parameter  $z_0$ . A derivation of the logarithmic wind profile in the fully-turbulent region is given by dimensional considerations in Roedel [2000].

---

<sup>1</sup>Von Kármán constant: In this study, the value of 0.4 (according to Hinze [1975]) was used.

**Outer Layer** For the wind profile in the outer region or the wake part, no theory was developed. Experiments show that wind profiles obey a self-similarity law [Hinze, 1975]

$$\frac{u_{\max} - u(z)}{u_*} = f\left(\frac{z}{\delta}\right), \quad (2.34)$$

with the free-stream velocity  $u_{\max}$  and the thickness  $\delta$ , which is the distance from the surface to the position where the free-stream velocity  $u_{\max}$  is reached (also called the 99 % boundary layer thickness). The self-similarity is useful for measuring the parameters of the turbulent region, when measurements close to the water surface are not possible. The shape of the wind profiles in the wake part is approximated with Hama's empirical formula [Hinze, 1975]

$$u_{\max} - u(z) = \beta \cdot u_* \cdot \left(1 - \frac{z}{\delta}\right)^2. \quad (2.35)$$

Different values were obtained for the parameter  $\beta$ . To determine self-similar wind profiles, it is useful to use  $\beta$  as a fit parameter [Troitskaya et al., 2012].

## 2.2. Gas Exchange Models

Models for mean concentration profiles are introduced in this section. To model the transport processes at the air-water interface, one has to regard the diffusive and turbulent transport mechanisms. The simplest model is the film model (Section 2.2.1), that assumes a constant layer with pure diffusive transport. In Sections 2.2.2 and 2.2.3, more elaborate models are discussed that model the change from diffusive transport at the water surface to turbulent transport in the water bulk. Section 2.2.4 presents a model for fluctuation concentration profiles, which was developed in the framework of this thesis. In Section 2.2.5, the Deacon model [Deacon, 1977] is presented. All considerations in this chapter are made for the water-side of the air-water interface.

### 2.2.1. Film Model

The film model was first published by Lewis and Whitman [1924]. They proposed that the transport of gases across the water surface is caused only by diffusion in a stagnant film at both sides of the interface. Outside of this layer, the transport is dominated by turbulence and the diffusion can be neglected. The concentration profile at the water side is obtained by setting the turbulent diffusivity  $K_c$  to zero and integrating equation (2.14) from the depth  $z = 0$  to the thickness of the mass boundary layer  $\delta_{\text{mbl}}$ . In dimensionless coordinates, with the dimensionless concentration  $c_+$  and the dimensionless depth  $z_+$

$$c_+ = \frac{c - c_b}{c_s - c_b} \quad \text{and} \quad z_+ = \frac{z}{\delta_{\text{mbl}}}, \quad (2.36)$$

## 2. Theory

with the concentration  $c_s$  at the surface and  $c_b$  in the water bulk, we obtain a linear concentration profile:

$$c_+(z_+) = 1 - z_+; \quad 0 \leq z_+ \leq 1 \quad (2.37)$$

Below the film thickness  $\delta_{\text{mbl}}$ , the concentration stays constant, due to the assumption of a well-mixed water bulk for  $z_+ > 1$ . The assumption of a layer with pure diffusion causing a linear concentration profile is a simplification, as turbulence reaches close to the interface as we will see in this study. The transfer velocity  $k$  predicted by the film model is given by integrating equation (2.18) up to the film thickness  $\delta_{\text{mbl}}$ :

$$k = \frac{1}{\int_0^{\delta_{\text{mbl}}} D^{-1} dz} = \frac{D}{\delta_{\text{mbl}}}. \quad (2.38)$$

The transfer velocity predicted by the film model is overestimated because the exponent of the diffusivity is usually smaller than 1 [Jähne et al., 1987].

### 2.2.2. Small Eddy Model

In the small eddy model, a function for a mean concentration profile is derived by describing the transport mechanism with a turbulent diffusivity  $K_c(z)$ , which is assumed to be zero at the water surface and grows with increasing depth. The derivation of the small eddy model is given in [Coantic, 1986]. The essential parts are presented here to point out the basic assumptions for this model. The concentration profile is obtained by solving the averaged transport equation for the concentration (2.8) for a given turbulent diffusivity  $K_c(z)$ :

$$\frac{\partial \bar{c}}{\partial t} = \frac{\partial}{\partial z} \left[ \frac{\partial \bar{c}}{\partial z} (D + K_c(z)) \right] \quad (2.39)$$

We obtain an expression for the turbulent diffusivity  $K_c$  by rewriting equation (2.14)

$$K_c(z) = -\frac{j_c}{\frac{\partial \bar{c}}{\partial z}} - D. \quad (2.40)$$

The turbulent diffusivity  $K_c(z)$  is approximated by inserting a Taylor expansion of the concentration profile at the water surface ( $z = 0$ ) into equation (2.40).

$$\bar{c}(z) = \bar{c}(0) + \sum_{n=1}^{\infty} \frac{1}{n!} \left. \frac{\partial^n \bar{c}}{\partial z^n} \right|_{z=0} z^n \quad (2.41)$$

The first derivative of the concentration profile  $\frac{\partial \bar{c}}{\partial z}$  at  $z = 0$  is described with pure diffusion according to equation (2.22). The higher order terms are obtained by assuming a stationary

state and using successive derivatives of the averaged transport equation (2.8).

$$D \frac{\partial^2 \bar{c}}{\partial z^2} \Big|_{z=0} = \frac{\partial}{\partial z} \overline{c'w'} \Big|_{z=0}. \quad (2.42)$$

To solve the right hand side and higher order derivatives, we have to make assumptions about boundary conditions near the interface.

**Turbulent Diffusivity for a Rigid Interface** For the case of a rigid interface, all components of the velocity fluctuations and the concentration fluctuation vanish at  $z = 0$ .

$$u' = v' = w' = 0 \Big|_{z=0} \quad \text{and} \quad c' = 0 \Big|_{z=0} \quad (2.43)$$

It follows that the derivatives of the velocity fluctuations in  $x$ - and  $y$ - direction are zero. The equation of continuity is also valid for the fluctuations

$$\nabla \cdot \vec{u}' = 0. \quad (2.44)$$

Accordingly, the derivative of the velocity fluctuation in  $z$ - direction is also zero

$$\frac{\partial w'}{\partial z} \Big|_{z=0} = 0. \quad (2.45)$$

With these boundary conditions, it is shown in [Coantic, 1986] that the turbulent diffusivity  $K_c$  grows cubically with the distance to the water surface.

$$K_c(z) \propto z^3 \quad (2.46)$$

**Turbulent Diffusivity for a Free Interface** For the case of a free interface, only the  $z$ - component of the velocity fluctuation and the concentration fluctuation at the interface are zero.

$$w' = 0 \Big|_{z=0} \quad \text{and} \quad c' = 0 \Big|_{z=0} \quad (2.47)$$

Coantic [1986] shows that these boundary conditions lead to a quadratic relation of the turbulent diffusivity  $K_c$  with depth  $z$

$$K_c(z) \propto z^2. \quad (2.48)$$

With the results for the turbulent diffusivity in the general form  $K_c(z) = \alpha_m z^m$  ( $m = 3$  for a rigid interface and  $m = 2$  for a free interface), the averaged transport equation (2.39) can be solved. In dimensionless coordinates, the transport equation has the following form [Jähne et al., 1989]

$$\frac{\partial \bar{c}_+}{\partial t_+} = \frac{\partial}{\partial z_+} \left[ (1 + \alpha_{m+} z_+^m) \frac{\partial \bar{c}_+}{\partial z_+} \right], \quad (2.49)$$

## 2. Theory

where  $t_+ = t/t_*$  denotes the normalized time. The differential equation (2.49) is solved for the steady state with the boundary conditions

$$\bar{c}_+(0) = 1 \quad \text{and} \quad \bar{c}_+(\infty) = 0 \quad \text{and} \quad \left. \frac{\partial c_+(z_+)}{\partial z_+} \right|_{z_+=0} = -1, \quad (2.50)$$

that originate from the definition of the normalized coordinates in equation (2.36) and the assumption that the transport at  $z = 0$  is only due to molecular diffusion. The solution for  $\alpha_{m+}$  is

$$\alpha_{m+} = \left( \frac{\pi}{m \sin(\pi/m)} \right)^m. \quad (2.51)$$

**Rigid Interface ( $m = 3$ )** For a rigid interface we obtain the following concentration profile, by solving the transport equation (2.39) with  $m = 3$  for the steady state and the solution for  $\alpha_{3+}$ .

$$\begin{aligned} \bar{c}_+(z_+) = & \frac{3}{4} + \frac{3}{2\pi} \tan^{-1} \left( \frac{1}{\sqrt{3}} - \frac{4\pi}{9} z_+ \right) \\ & - \frac{\sqrt{3}}{2\pi} \ln(9 + 2\sqrt{3}\pi z_+) + \frac{\sqrt{3}}{4\pi} \ln \left( 3(27 - 6\sqrt{3}\pi z_+ + 4\pi^2 z_+^2) \right) \end{aligned} \quad (2.52)$$

**Free Interface ( $m = 2$ )** For a free interface, the mean concentration profile is obtained by solving the transport equation (2.39) with  $m = 2$  for the steady state and the solution for  $\alpha_{2+}$  [Jähne et al., 1989].

$$\bar{c}_+(z_+) = \frac{2}{\pi} \cdot \cot^{-1} \left( \frac{\pi}{2} z_+ \right) \quad (2.53)$$

**Schmidt Number Dependence** The transfer velocity  $k$  for the small eddy model is calculated in Coantic [1986]. The result is a Schmidt number dependence of  $Sc^{-2/3}$  and  $Sc^{-1/2}$  for a rigid ( $m = 3$ ) and a free interface ( $m = 2$ ), respectively.

$$k \propto u_* Sc^{-1 + \frac{1}{m}} \quad (2.54)$$

This result is in agreement with experiments by Jähne et al. [1987] (see [Krall, 2013] for a recent study in our group).

### 2.2.3. Surface Renewal Model

The surface renewal model assumes that the transport of gases is mainly due to statistical surface renewal events, that transport water volumes from the surface to the bulk. After a renewal event, the concentration at the water surface is the same as the concentration in the water bulk  $c_b$ , as Figure 2.2 shows. In the time between two surface renewal events, the gas transport is caused by diffusion. A model with periodical renewal events was first proposed by Higbie [1935]. A more realistic random renewal rate was later proposed by Danckwerts [1951] and Harriott [1962]. In

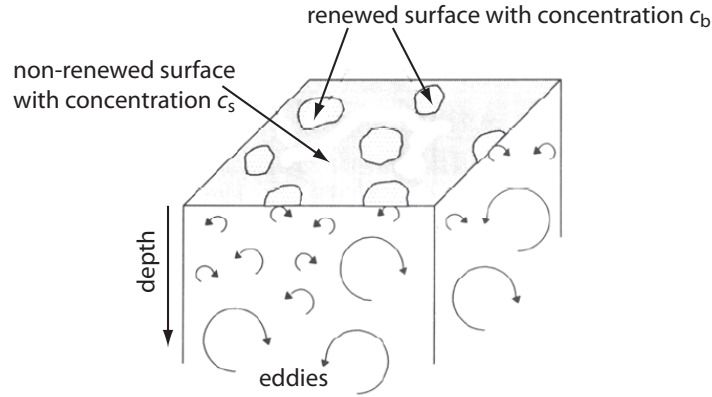


**Figure 2.2.:** Schematic drawing of surface renewal events (from Asher and Pankow [1991]).

the general form, the renewal rate  $\lambda$  is proportional to the depth  $z$  to the power of  $p$  [Jähne, 1985]

$$\lambda = \gamma_p z^p. \quad (2.55)$$

For  $p = 0$ , the renewal rate shows no depth dependence, as assumed by Danckwerts [1951] and Harriott [1962]. This is a contradiction to the hydrodynamical assumption that the fluctuations  $w'$  and  $c'$  at wall are zero. For  $p = 1$ , the renewal rate grows linear with depth. A mathematical description of the surface renewal model is obtained by expressing the turbulent term in the averaged transport equation (2.8) with the product of renewal rate  $\lambda$  and concentration  $c$ :

$$\frac{\partial \bar{c}}{\partial t} = D \frac{\partial^2 \bar{c}}{\partial z^2} - \lambda c. \quad (2.56)$$

In dimensionless variables, we obtain

$$\frac{\partial \bar{c}_+}{\partial t_+} = \frac{\partial^2 \bar{c}_+}{\partial z_+^2} - \gamma_p z_+^p c_+. \quad (2.57)$$

The Schmidt number dependence of the transfer velocity  $k$  was calculated with the surface renewal model by Jähne [1985]. For  $p=0$  and  $p=1$ , a dependence of  $Sc^{-1/2}$  and  $Sc^{-2/3}$ , respectively, was obtained:

$$k \propto u_* Sc^{-\frac{p+1}{p+2}} \quad (2.58)$$

The Schmidt number dependence suggests that the  $p=0$  and  $p=1$  case represents a free and a rigid interface, respectively. To solve the differential equation (2.57), the same boundary conditions (equation (2.50)) as for the small eddy model are used.

**Rigid Interface ( $p = 1$ )** For a rigid interface the mean concentration profile was first published in [Jähne et al., 1989]:

$$\bar{c}_+(z_+) = \frac{1}{\text{Ai}(0)} \text{Ai}\left(-\frac{\text{Ai}(0)}{\text{Ai}'(0)} z_+\right) \quad (2.59)$$

## 2. Theory

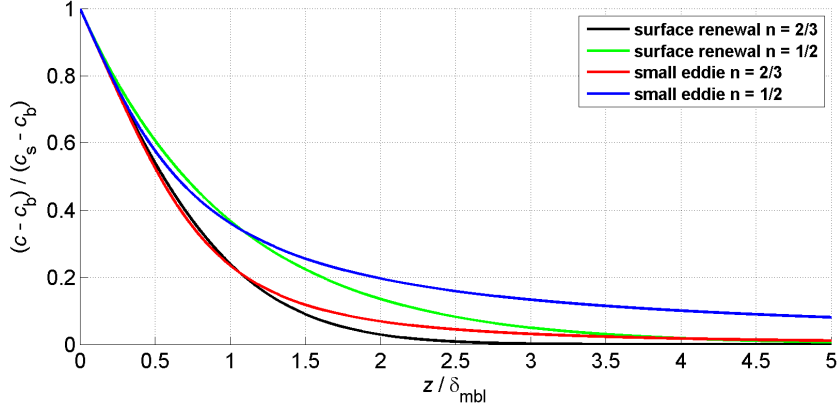


**Figure 2.3.:** Mean concentration profiles from the model prediction with the small eddy model and the surface renewal model for the boundary condition of a rigid interface ( $n = 2/3$ ) and a free interface ( $n = 1/2$ ).

**Free Interface ( $p = 0$ )** For a free interface we obtain the following mean concentration profile:

$$\bar{c}_+(z_+) = \exp(-z_+) \quad (2.60)$$

Figure 2.3 shows the concentration profiles in dimensionless units  $c_+$  and  $z_+$  predicted by the small eddy model and surface renewal model for a Schmidt number exponent of  $n$  of  $2/3$  and  $1/2$ . The concentration  $c_+(z_+)$  at the surface and in the water bulk, as well as the derivative of the concentration profile at the surface are the same for all model functions according to the boundary conditions of the models in equation (2.50). However, the model functions for  $n = 1/2$  have a similar shape, as will be shown in Section 9.4.2.

### 2.2.4. Model for Fluctuation Concentration Profiles

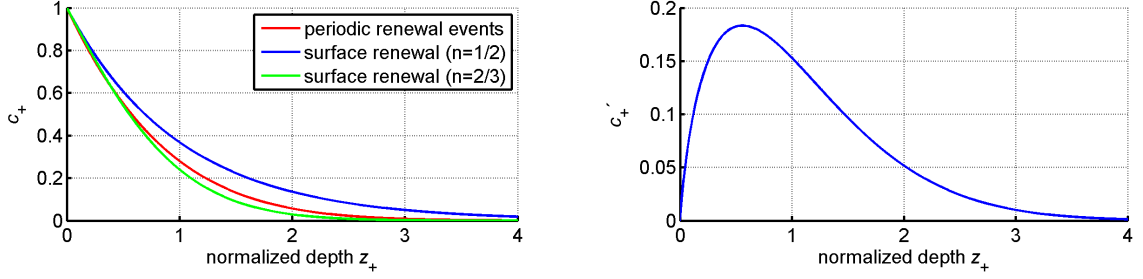
Here, a model is presented that is able to predict fluctuation concentration profiles. It is based on the assumption that the transport process of gas concentrations at an interface is controlled by diffusion and periodical renewal events, such as the surface renewal model in the previous section. The model is formulated in one dimension, as the transport process is assumed to be homogeneous in the  $x$ - and  $y$ -direction. The transport equation for diffusion is described with Fick's second law:

$$\frac{\partial c(z, t)}{\partial t} = D \frac{\partial^2 c(z, t)}{\partial z^2} \quad (2.61)$$

The boundary condition for the concentration at the water surface is a constant concentration  $c_s$ , which is always in equilibrium with the air concentration according to Henry's law:

$$c(z = 0, t) = c_s \quad (2.62)$$

The second boundary condition is that the concentration at time  $t = 0$  has the constant value  $c_b$  in the water bulk. The concentration profile at time  $t = 0$  is described with the Heaviside



(a) Concentration profiles from surface renewal predictions and the model developed here. (b) Fluctuation concentration profiles with the model developed here.

**Figure 2.4.:** Mean concentration profile and fluctuation concentration profile in normalized units that were calculated with the model developed in this section.

step function  $\Theta$ :

$$c(z, t = 0) = 2(c_s - c_b)\Theta(-z) + c_b \quad (2.63)$$

A solution for the transport equation (2.61) with the given boundary conditions is the complementary error function erfc:

$$c(z, t) = (c_s - c_b) \cdot \operatorname{erfc}\left(\frac{z}{2\sqrt{Dt}}\right) + c_b \quad (2.64)$$

In dimensionless coordinates, we obtain the solution:

$$c_+(z_+, t_+) = \operatorname{erfc}\left(\frac{z_+}{2\sqrt{t_+}}\right) \quad (2.65)$$

At time  $t_+ = 0$ , the dimensionless concentration  $c_+$  in the water is zero for  $z_+ > 0$ . For  $t_+ > 0$ , a concentration profile establishes that drops to zero for  $z_+ \rightarrow \infty$ . With increasing time, the concentration gradient at the water surface decreases. After the time interval  $\tau$  (the dimensionless renewal time), a surface renewal event occurs and the concentration  $c_+$  for  $z_+ > 0$  is again zero. In the model presented here, it is assumed that those renewal events occur in periodic time intervals  $\tau$ . According to the boundary conditions of the surface renewal model in equation (2.50), the renewal time  $\tau$  is set to unity.

The mean concentration profile  $\bar{c}_+(z_+)$  is obtained by calculating the expectation value of equation (2.65). The integral was solved with the program Mathematica<sup>®</sup>.

$$\begin{aligned} \bar{c}_+(z_+) &= \int_0^1 \operatorname{erfc}\left(\frac{z_+}{2\sqrt{t_+}}\right) dt_+ \\ &= -\frac{z_+}{\sqrt{\pi}} \exp\left(-\frac{z_+^2}{4}\right) + \frac{1}{2}(2 + z_+^2) \cdot \operatorname{erfc}\left(\frac{z_+}{2}\right) \end{aligned} \quad (2.66)$$

The obtained function for the mean concentration profile is shown in Figure 2.4(a). For comparison, the predicted concentration profiles with the surface renewal model for a Schmidt number

## 2. Theory

exponent of 1/2 and 2/3 are plotted. The derivative of the concentration profile at the water surface is the same for all three models according to the boundary conditions. The solution of the calculated profile is between the two model predictions of the surface renewal model for a rigid and a free interface. The benefit of the model developed here is that concentration fluctuations can also be calculated, as we developed a description for the temporal development of the concentration. The rms fluctuation concentration is computed according to the definition of the variance  $\text{Var}$  of a variable  $X$

$$\text{Var}(X) = E(X^2) - E(X)^2, \quad (2.67)$$

with the expectation value  $E(X)$ . Accordingly, we obtain for the root mean concentration fluctuation the expression

$$c_+^{\prime 2}(z_+) = \int_0^1 \text{erfc}^2\left(\frac{z_+}{2\sqrt{t_+}}\right) dz_+ - \left(\int_0^1 \text{erfc}\left(\frac{z_+}{2\sqrt{t_+}}\right) dz_+\right)^2. \quad (2.68)$$

An analytic function was not found for the integrals. The numerical solution, calculated with Mathematica<sup>®</sup>, is shown in Figure 2.4(b). The peak position at about  $z_+ = 0.557$  and maximum of about  $c' = 0.183$  will be used for a comparison to the measured fluctuation concentration profiles in Section 9.5.

### 2.2.5. The Deacon Model

The Deacon model [Deacon, 1977] yields an expression for the gas transfer velocity with respect to the friction velocity, valid for a smooth water surface. The model is based on the interpolation formula of Reichardt [1951], that describes the transition of the turbulent diffusivity  $K_m(z)$  from the cubic to the linear region. This approximation is only applicable for a rigid interface (in analogy to equation (2.42)) and accordingly a smooth water surface. For the derivation of the transfer velocity, the turbulent Schmidt number  $Sc_t = \frac{K_m}{K_c}$  is assumed to be unity. The transfer velocity  $k$  is obtained by integration equation (2.18) numerically, yielding

$$k = 0.082 \left(\frac{\rho_a}{\rho_w}\right)^{0.5} Sc^{-2/3} u_*, \quad (2.69)$$

where  $\frac{\rho_a}{\rho_w}$  denotes the ratio of the density of water and of air. The Deacon model is used as a lower limit for the gas transfer velocity.

## 2.3. Luminescence Theory

This section provides a summary of the basic processes of luminescence which are needed in this study, following Lakowicz [2006]. Section 2.3.1 introduces luminescence. The difference between a weak and a strong excitation is described in Section 2.3.3. Section 2.3.4 focuses on the effect of quenching, which is crucial for this study's measuring method. It also presents the generalized Stern-Volmer equation<sup>2</sup> which plays an important role in understanding the dynamic quenching process. This knowledge is specifically needed in Chapter 5.

### 2.3.1. Introduction to Luminescence

Luminescence is the emission of light by an atom due to the transition of an electron from an excited state into a state of lower energy. The luminescent process can be classified depending on the process of excitation. This study deploys photoluminescence which is excitation caused by light absorption. The terms chemo-, thermo-, and electroluminescence are used when the excited state is reached by a chemical reaction, thermal energy, and a voltage difference, respectively.

**Fluorescence and Phosphorescence** Luminescence is divided into two classes, depending on the nature of the excited state: fluorescence and phosphorescence. The electron in the excited energy state can either have its spin opposite or in the same direction as the other electron in the ground state orbital. The excited state is called a singlet state or a triplet state, if the spins are aligned in the same or opposite direction, respectively.

Fluorescence is a transition from a singlet state to the ground state, which is spin-allowed according to the rules of quantum mechanics. This results quickened decay and an emission of a photon. Phosphorescence occurs when a triplet state decays into the ground state. This transition is quantum mechanically forbidden and results in a long lifetime.

**Luminescent Processes** The luminescence processes can be illustrated with a Jablonski diagram, named after A. Jablonski. A typical Jablonski diagram is shown in Figure 2.5. The  $y$ -axis depicts energy states, singlet states ( $S$ ) are on the left side, triplet states ( $T$ ) on the right. In each state, the electron can exist in multiple vibrational levels shown as three levels in the diagram.

The process of photoluminescence starts with the absorption of a photon that has sufficient energy to reach one of the singlet states  $S_1$  or  $S_2$ . This absorption is quasi-instantaneous, occurring in about  $10^{-15}$  s. Three decay paths are illustrated in Figure 2.5: internal conversion (IC), fluorescence, and intersystem crossing (ISC). The fastest decay in condensed matter is usually IC, which has a lifetime of about  $10^{-12}$  s. Because this lifetime is much shorter than the lifetime of fluorescence, which is on the order of  $10^{-8}$  s, the excited electron decays to the

---

<sup>2</sup>The generalized Stern-Volmer equation was derived in the process of this study. It presents the generalization of the known Stern-Volmer equation (see Stern and Volmer [1919]) for arbitrary laser irradiance.

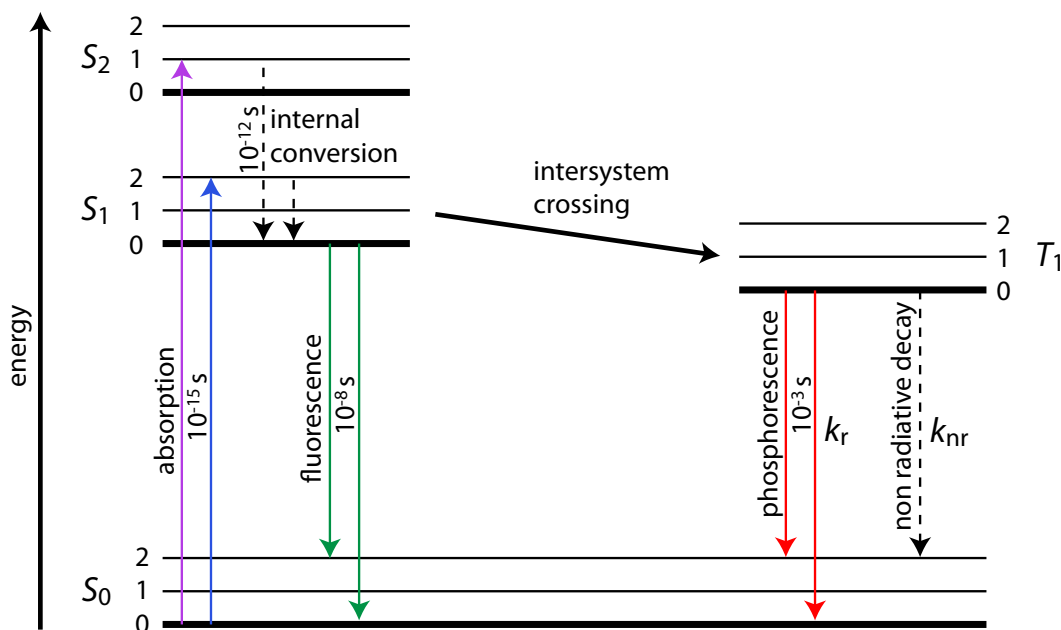


**Figure 2.5.:** Jablonski diagram: Singlet states (on the left) are depicted with an  $S$ , the first triplet state (on the right) with a  $T_1$ . Each state splits into multiple vibrational energy levels, depicted here with 0, 1, 2. Fluorescence occurs when a singlet state decays into the ground state, and phosphorescence describes the transition from a triplet state to the ground state. The typical lifetimes of the processes are indicated. The decay rate of phosphorescence is denoted with a  $k_r$ , the non-radiative decay rate from the  $T_1$  state with a  $k_{nr}$ .

lowest vibrational energy level before the fluorescent decay occurs. In conclusion, the decay of a fluorescent process starts at the lowest vibrational energy level of a singlet state and ends at any vibrational level of the ground state  $S_0$ . In Figure 2.5, two possible fluorescence decay paths are illustrated as an example.

In phosphorescent molecules, the decay path of ISC is faster than that of fluorescence. The excited electron can undergo a spin conversion and decay into the triplet state  $T_1$  due to spin-orbit coupling. As mentioned above, the transition from the triplet to a singlet state is forbidden. This fact results in a typical phosphorescence lifetime of about  $10^{-3}$  s.<sup>3</sup>

Aside from fluorescent and phosphorescent decay, there are non-radiative decay processes, such as collisional quenching, that can cause an excited state to decay to the ground state  $S_0$ . The phosphorescent decay rate  $k_r$  and the decay rate of all the non-radiative processes  $k_{nr}$ , from the triplet to the ground state, are illustrated in Figure 2.5.

**Stokes Shift** The energy emitted from a luminescent species is typically lower than the absorbed energy. This Stokes shift was named after G. G. Stokes who first observed the effect in the 19<sup>th</sup> century. The reasons for this effect become evident in the Jablonski diagram. Absorption usually starts at the lowest vibrational level of the ground state, as the electron population

<sup>3</sup>In Section 2.3.2 it will be shown that there are also phosphorescent molecules with a much shorter lifetime on the order of  $10^{-6}$  s. This is the case for the metal-ligand complex (MLC) used in this study.

density is highest in that state. After excitation, the excited state rapidly decays via IC into the lowest vibrational level. The excited electron can decay into any vibrational level of the ground state  $S_0$ . The lowest vibrational level of the ground state is reached by the IC process. Due to the decay of the electron via IC processes in both, the ground and the excited state, the energy of the emitted photon is lower than the energy of the absorbed photon. To visualize this effect, Figure 2.5 shows that the possible energy gaps (length of arrows) for fluorescence and phosphorescence are smaller or equal than the required absorption energies.

Solvent relaxation can lead to substantial Stokes shifts. This effect occurs in water through interactions between the fluorophore<sup>4</sup> and the dipole moment of water. The interactions between the fluorophore and the water molecules are different in the ground and the excited state due to different dipole moments of the fluorophore in the two states. After excitation, the water molecules rearrange to minimize the energy of the excited state. This leads to a lowering of the energy of the excited state and an elevation of the energy of the ground state. After the excited electron decays to the lifted ground state, the water molecules must rearrange again to adapt to the changed dipole moment of the fluorophore and to reach the initial ground state where the process started. The two solvent relaxation processes in both, the excited and the ground state, lead to a lower energy of the emitted photon than the absorbed photon.

**Lifetime and Quantum Yield** The lifetime and quantum yield of a fluorophore are expressions containing the radiative decay rate  $k_r$  and the non-radiative decay rate  $k_{nr}$ . The quantum yield  $\eta$  is the number of emitted photons relative to the number of absorbed photons. In equilibrium, the absorption rate  $k_a$  must be equal to the sum of the radiative decay rate  $k_r$  and the non-radiative decay rate  $k_{nr}$ .

$$\eta = \frac{k_r}{k_a} = \frac{k_r}{k_r + k_{nr}} \quad (2.70)$$

Very high quantum yields that are close to unity can be observed when the non-radiative decay rate is small. The quantum yield of phosphorescence is typically low because the decay rate  $k_r$  is small compared to the non-radiative decay rate  $k_{nr}$  ( $k_r \ll k_{nr}$ ).

The lifetime  $\tau_0$  is defined as the average time the electron spends in the excited state. It is given as the reciprocal of the total decay rate  $\gamma = k_r + k_{nr}$ .

$$\tau_0 = \frac{1}{\gamma} \quad (2.71)$$

### 2.3.2. The MLCT Process

This section introduces the effect of the metal-to-ligand charge transfer (MLCT), which is the mechanism how the fluorophore used in this study, the Ru complex, is excited. The Ru complex, which is characterized in Chapter 5, consists of a transition metal and a ligand. This group

---

<sup>4</sup>A fluorescent molecule is also called fluorophore. In this text the word fluorophore will be used for fluorescent as well as phosphorescent molecules.

## 2. Theory

of fluorophores is called metal-ligand complexes (MLCs), and it is typified by the expression [metal(ligand)]. The metal is typically one of the elements rhenium (Re), ruthenium (Ru), osmium (Os), and iridium (Ir). Decay times of MLCs typically range from  $10^{-7}$  s to  $10^{-5}$  s.

The luminescent properties of MLC complexes are due to unique electronic states. The presence of the ligand splits the five  $d$ -orbital energy levels of the outermost shell of the metal into three lower ( $d_l$ ) and two higher ( $d_h$ ) states with an energy gap  $\Delta$  (see Figure 2.6). Ru has six

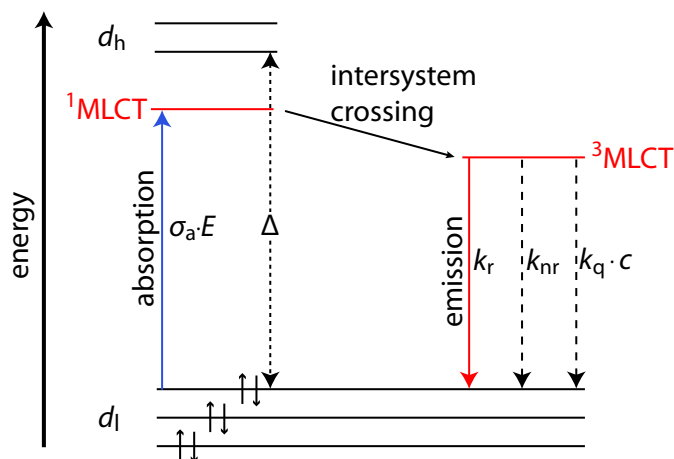


**Figure 2.6.:** Jablonski diagram depicting the metal-to-ligand charge transfer (MLCT) in a Ru complex. The  $d_l$ - and  $d_h$ - orbitals are indicated by the letters  $d_l$  and  $d_h$ , respectively. The six  $d$ -electrons of Ru are drawn in pairs as arrows with an opposite spin direction. Due photon absorption, an electron is promoted from the metal to the ligand, into the singlet MLCT state. Intersystem crossing to the triplet MLCT state occurs in less than 300 fs. The excited complex in the triplet MLCT state decays by phosphorescent emission, non-radiative decay processes, and quenching with the decay rates  $k_r$ ,  $k_{nr}$ , and  $k_q \cdot c$ , mentioned in Section 2.3.4. Modified from Lakowicz [2006].

$d$ -electrons in the outer orbit, which is depicted in Figure 2.6 with three pairs of arrows in opposite spin direction. The transition from the  $d_l$ -orbital to the  $d_h$ -orbital is forbidden (Lakowicz [2006]). Even if an absorption into the  $d_h$ -orbital occurs, the emission is quenched with a high probability, which is enabled by the long lifetime. The ligand offers another possibility for a transition, the so called metal-to-ligand charge transfer (MLCT). By the absorption of light, an electron can be promoted from the metal to the ligand. The reaction equation for the Ru complex shows that the metal Ru is oxidized and the ligand  $dpp^5$  reduced:



After reaching the singlet MLCT state, intersystem crossing to the triplet MLCT state occurs in less than 300 fs (see Figure 2.6). According to Demas and Taylor [1979], the quantum yield for the formation of the triplet MLCT state is near unity. From the triplet MLCT state, the excited complex decays by phosphorescent emission. Decay times are shorter than normal phosphorescence. In the book of Lakowicz [2006, Chapter “Long-Lifetime Metal-Ligand Complexes”], this is attributed to be due to spin-orbit coupling of the ligand with the transition metal atom.

<sup>5</sup>dpp is a short form for 4,7-diphenyl-1,10-phenanthroline.

### 2.3.3. Weak and Strong Excitation

Depending on the irradiance of the exciting laser, the excitation can be either weak or strong. As the implications are important for this study, a short derivation is given here.

The fluorophore is regarded as a two-level system with concentration  $n$  (in  $\text{m}^{-3}$ ) in the ground state and  $n^*$  in the excited state. This simplification is reasonable here, because the result only depends on the concentrations in the ground state and excited state, regardless of the vibrational levels. In equilibrium, the number of decaying atoms per time and volume ( $n^* \cdot \gamma$ ) equal the number of excited atoms per time and volume ( $n \cdot E \cdot \sigma_a$ )

$$n \cdot E \cdot \sigma_a = n^* \cdot \gamma \quad (2.73)$$

where  $\sigma_a$  is the absorption cross section,  $\gamma$  the total decay rate, and  $E$  the irradiance (in photons  $\text{s}^{-1} \text{m}^{-2}$ ) of the exciting laser. Using the total concentration of the fluorophore  $N = n + n^*$ , it follows that

$$\frac{n^*}{N} = \frac{E}{\frac{\gamma}{\sigma_a} + E} \quad (2.74)$$

Defining the saturation irradiance  $E_{\text{sat}}$

$$E_{\text{sat}} := \frac{\gamma}{\sigma_a} \quad (2.75)$$

equation (2.74) becomes

$$\frac{n^*}{N} = \frac{E}{E_{\text{sat}} + E} \quad (2.76)$$

For low laser irradiance ( $E \ll E_{\text{sat}}$ ), the excitation is called weak and the density  $n^*$  is proportional to the laser irradiance.

$$\frac{n^*}{N} = \frac{E}{E_{\text{sat}}} \quad (2.77)$$

This approximation will not be valid throughout this study. In the case of high laser irradiance ( $E \gg E_{\text{sat}}$ ), the excitation is called strong and the concentration of fluorophore molecules in the excited state  $n^*$  no longer depends on laser irradiance.

$$\frac{n^*}{N} = 1 \quad (2.78)$$

### 2.3.4. Quenching

The emission intensity of a fluorophore can decrease in the presence of other molecules. The interaction that leads to a decrease in intensity is called quenching, which is divided into two classes: static and dynamic quenching.

Static quenching occurs if the fluorophore in the ground state forms a non-fluorescent complex with the quencher<sup>6</sup>, leading to a decrease in the intensity of the emitted light. The lifetime of

---

<sup>6</sup>A quencher is a molecule that leads to quenching effects.

## 2. Theory

the excited state remains unchanged as the decay rates  $k_r$  and  $k_{nr}$  stay unaffected.

In the case of dynamic quenching, the quencher leads to a non-radiative decay of the fluorophore. Dynamic quenching is caused by different effects such as collisional quenching, energy transfer (known as FRET<sup>7</sup>), and excited-state reactions. Common to all mechanisms is that energy is transferred from the excited fluorophore to the quencher. The most prominent collisional quencher is oxygen, which is used in this study.

The quenching effect can be illustrated with the simple two-level system in Figure 2.7. The possible absorption and decay paths can be seen without (Figure 2.7(a)) and with the quenching term (Figure 2.7(b)). The ground and excited state concentrations are denoted with  $n$  and  $n^*$ , respectively. The subscript 0 indicates that there is no quencher.

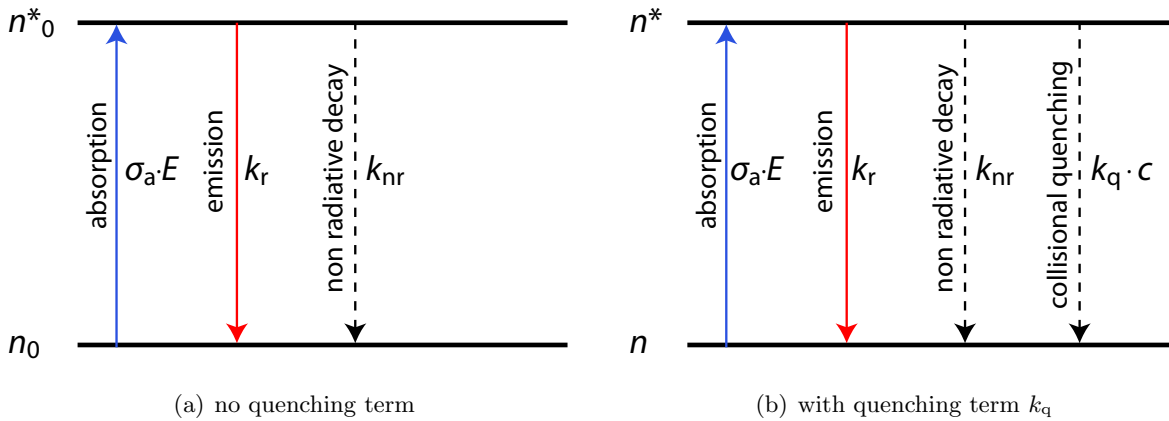


**Figure 2.7.:** Two-level system with ground and excited state concentrations of the fluorophore  $n$  and  $n^*$ , respectively. If there is no quencher, the states are denoted with the subscript 0. The terms  $k_r$  and  $k_{nr}$  depict the decay rate of phosphorescent emission and non-radiative decay processes. The expression  $\sigma_a \cdot E$  is the absorption rate. The decay rate of phosphorescent quenching is the product of the bimolecular quenching constant  $k_q$  and the quencher concentration  $c$ .

Figure 2.7(a) shows the absorption rate  $\sigma_a \cdot E$ , the emission rate  $k_r$ , and the non-radiative decay rate  $k_{nr}$  including all non-radiative processes other than quenching. The absorption rate is the product of the laser irradiance  $E$  and the absorption cross section  $\sigma_a$ . In Figure 2.7(b) the collisional quenching rate is added which is the product of the bimolecular quenching constant  $k_q$  and the quencher concentration  $c$ . In conclusion, the concentration in the excited state with quenching term  $n^*$  is smaller than the concentration without quenching  $n_0^*$ . Therefore, the emission intensity decreases with increasing quencher concentration  $c$ . This is expressed by the Stern-Volmer equation [Stern and Volmer, 1919].

**Derivation of the Generalized Stern-Volmer Equation for Dynamic Quenching** This study uses the effect of dynamic quenching. Therefore, only the derivation of the Stern-Volmer equation for dynamic quenching is given.

The effect of a strong excitation of the fluorophore has not been regarded so far with the

<sup>7</sup>FRET: Förster-resonance energy transfer or fluorescence-resonance energy transfer

Stern-Volmer equation. The Stern-Volmer equation was first documented by Stern and Volmer [1919]. They observed that the fluorescence of iodine vapour decreased with pressure. In the original publication, the approximation of a weak excitation was made. This was valid because sunlight was used to excite the iodine vapour, leading to a low excitation. With the invention of the laser in the late fifties, a source with a high irradiance became available. When a focused laser is used in fluorescence measurements, the approximation of a weak excitation is no more valid because high laser irradiance values can be reached.

Standard works about fluorescence were written before fluorescence measurements with lasers were conducted. None of them discusses the effect of a strong excitation on the Stern-Volmer equation. The books of Förster [1951] and Pringsheim [1949] discuss fluorescence quenching in detail, without mentioning the effect of a strong excitation on the Stern-Volmer equation. Recent books dealing with fluorescence quenching, such as Lakowicz [2006] still kept using the assumption of a weak excitation.

Here, I demonstrate that a high laser irradiance will have a significant impact on the Stern-Volmer constant. In the following, the general Stern-Volmer equation is derived for arbitrary laser irradiance.

When the system is in equilibrium and the quencher is present, the concentration of the excited state  $n^*$  remains constant over time, and the number of excited atoms per time and volume equal the number of decaying atoms per time and volume.

$$\frac{dn^*}{dt} = n \cdot E \cdot \sigma_a - (\gamma + k_q \cdot c) \cdot n^* = 0 \quad (2.79)$$

The relationship between the concentration  $n^*$  and the incident laser irradiance  $E$  is calculated analogous to equation (2.73). The result is similar to equation (2.74). The decay rate through collisional quenching  $k_q \cdot c$  is added as a further decay channel to the total rate  $\gamma$ .

$$\frac{n^*}{N} = \frac{E}{\frac{\gamma + k_q \cdot c}{\sigma_a} + E} \quad (2.80)$$

Without the quencher, equation (2.74) applies for the concentration in the excited state  $n_0^*$ .

$$\frac{n_0^*}{N} = \frac{E}{\frac{\gamma}{\sigma_a} + E} \quad (2.81)$$

The ratio of  $n_0^*$  and  $n^*$  is obtained by dividing equation (2.81) and (2.80).

$$\frac{n_0^*}{n^*} = 1 + \frac{k_q \cdot c}{\sigma_a} \cdot \frac{1}{\frac{\gamma}{\sigma_a} + E} \quad (2.82)$$

The photon flux  $\Phi$  (in photons  $\cdot$  s $^{-1}$ ) and  $\Phi_0$  of the emitted light for the quenched and the unquenched fluorophore out of the volume element  $\Delta V$  is proportional to the concentrations in the excited state  $n^*$  and  $n_0^*$ , respectively, the radiative decay rate  $k_r$  and the size of the volume

## 2. Theory

element.

$$\begin{aligned}\Phi &= k_r \cdot n^* \cdot \Delta V \\ \Phi_0 &= k_r \cdot n_0^* \cdot \Delta V\end{aligned}\tag{2.83}$$

In conclusion, the ratio between the photon flux  $\Phi_0$  and  $\Phi$  can be calculated from equation (2.82):

$$\frac{\Phi_0}{\Phi} = \frac{n_0^*}{n^*} = 1 + \frac{k_q \cdot c}{\sigma_a} \cdot \frac{1}{\frac{\gamma}{\sigma_a} + E}\tag{2.84}$$

This equation can be simplified by using equations (2.71) and (2.75) and the Stern-Volmer constant

$$K_{SV} := k_q \cdot \tau_0,\tag{2.85}$$

which is defined as the product of the bimolecular quenching constant  $k_q$  and the lifetime  $\tau_0$  of the unquenched fluorophore. The resulting equation is the generalized Stern-Volmer equation for arbitrary laser irradiance  $E$ .

$$\frac{\Phi_0}{\Phi} = 1 + K_{SV} \cdot c \cdot \frac{E_{sat}}{E + E_{sat}}\tag{2.86}$$

For simplification, a new term, the damping factor  $\epsilon_D$  of the Stern-Volmer equation, is introduced:

$$\epsilon_D := \frac{E_{sat}}{E + E_{sat}}\tag{2.87}$$

By definition  $0 < \epsilon_D \leq 1$  and:

$$\frac{\Phi_0}{\Phi} = 1 + K_{SV} \cdot c \cdot \begin{cases} 1 & E \ll E_{sat} \\ 0.5 & E = E_{sat} \\ 0 & E \gg E_{sat} \end{cases}\tag{2.88}$$

In case of a weak excitation ( $E \ll E_{sat}$ ), the generalized Stern-Volmer equation simplifies, and the Stern-Volmer equation is obtained.

$$\frac{\Phi_0}{\Phi} = 1 + K_{SV} \cdot c\tag{2.89}$$

A comparison between the generalized (2.86) and weak excitation (2.89) Stern-Volmer equations shows that a strong excitation leads to a reduction of the quenching term. A descriptive explanation of the effect is given here, by taking a closer look at the two limiting cases of a weak and a strong excitation.

In the case of weak excitation ( $E \ll E_{sat}$ ) nearly all atoms of the fluorophore are in the ground state ( $n \approx N$ ). In conclusion, the rate of excitations per volume

$$r_{ex} := n \cdot E \cdot \sigma_a \approx N \cdot E \cdot \sigma_a$$

is a constant for constant laser power. In equilibrium, the decay rate per volume ( $n^* \cdot \gamma + n^* \cdot k_q \cdot c$ ), including the collisional quenching process, must be equal to the excitation rate per volume. Therefore, the decay rate per volume is also constant:

$$n^* \cdot (\gamma + k_q \cdot c) \approx r_{\text{ex}} \quad (2.90)$$

A higher quencher concentration  $c$  enhances the collisional quenching rate ( $k_q \cdot c$ ) and decreases the concentration in the excited state  $n^*$ . Using equations (2.83) and (2.90), we see that the photon flux  $\Phi$  decreases with increasing quencher concentration:

$$\Phi \approx k_r \cdot \Delta V \cdot r_{\text{ex}} \cdot \frac{1}{\gamma + k_r \cdot c} \quad (2.91)$$

This term can be converted into the Stern-Volmer equation (2.89).

For the case of a strong excitation rate ( $E \gg E_{\text{sat}}$ ) we can assume that all atoms of the fluorophore are in the excited state ( $n^* \approx N$ , see equation (2.78)). The photon flux  $\Phi$  can be calculated directly with equation (2.83):

$$\Phi = k_r \cdot n^* \cdot \Delta V \approx k_r \cdot N \cdot \Delta V \quad (2.92)$$

This expression is independent of the quencher concentration, and the generalized Stern-Volmer equation (2.86) with  $\epsilon_D \approx 0$  has to be used in this case. Figure 2.7(b) also visualizes this fact. With increasing quencher concentration  $c$ , the number of fluorophores per time and volume decaying by collisional quenching  $n^* \cdot k_q \cdot c$  grows. The absorption rate per volume increases with the same amount, because every decaying atom is instantaneously excited again as a result of the infinite high laser irradiance  $E \gg E_{\text{sat}}$ . Therefore, the number of fluorophores per time and per volume taking the radiative decay path and hence the photon flux  $\Phi$  stay unaffected.

When a calibration of the Stern-Volmer constant  $K_{\text{SV}}$  is performed, the damping factor  $\epsilon_D$  must be known. This term deviates from unity for a high laser irradiance  $E$  and a long lifetime  $\tau_0$  of the fluorophore. This fact has important implications on the measuring technique. If the laser irradiance is too high, the damping factor  $\epsilon_D$  decreases, leading to a lower signal-to-noise ratio (SNR) of the measured  $\text{O}_2$  concentrations. For the case of a low laser irradiance, the damping factor  $\epsilon_D$  is close to unity, but the photon flux  $\Phi$  decreases, leading also to a low SNR ratio. The optimal laser irradiance lies between those limiting cases.

**Differences between Static and Dynamic Quenching** The Stern-Volmer equation describes the quenching process for both static and dynamic quenching. Lifetime and temperature effects distinguish between the two kinds.

For static quenching the lifetimes of the quenched and unquenched fluorophore are the same because the decay rates  $k_r$  and  $k_{\text{nr}}$  are unaffected. In the case of dynamic quenching, the lifetime

## 2. Theory

of the quenched fluorophore can be written as the reciprocal value of all decay rates.

$$\tau = \frac{1}{k_r + k_{nr} + k_q \cdot c} \quad (2.93)$$

A division of equation (2.93) with the lifetime of the unquenched fluorophore (2.71) expresses the change of the lifetime.

$$\frac{\tau_0}{\tau} = 1 + K_{SV} \cdot c \quad (2.94)$$

A comparison of the equations (2.94) and (2.89) shows that the effect of a quencher on the lifetime  $\tau$  and the photon flux  $\Phi$  is the same for the case of a weak excitation:

$$\frac{\tau_0}{\tau} = \frac{\Phi_0}{\Phi} \quad (2.95)$$

Another difference between the two kinds of quenching is the temperature dependence of the Stern-Volmer constant  $K_{SV}$  (Figure 2.8). For static quenching the weakly bound non-fluorescing complex dissociates under higher temperatures. In this case, the quenching effect is smaller for high temperatures, resulting in a smaller Stern-Volmer constant  $K_{SV}$ . In the case of dynamic quenching, a higher temperature increases the diffusion rate. The enhanced collision rate results in a higher Stern-Volmer constant  $K_{SV}$ .

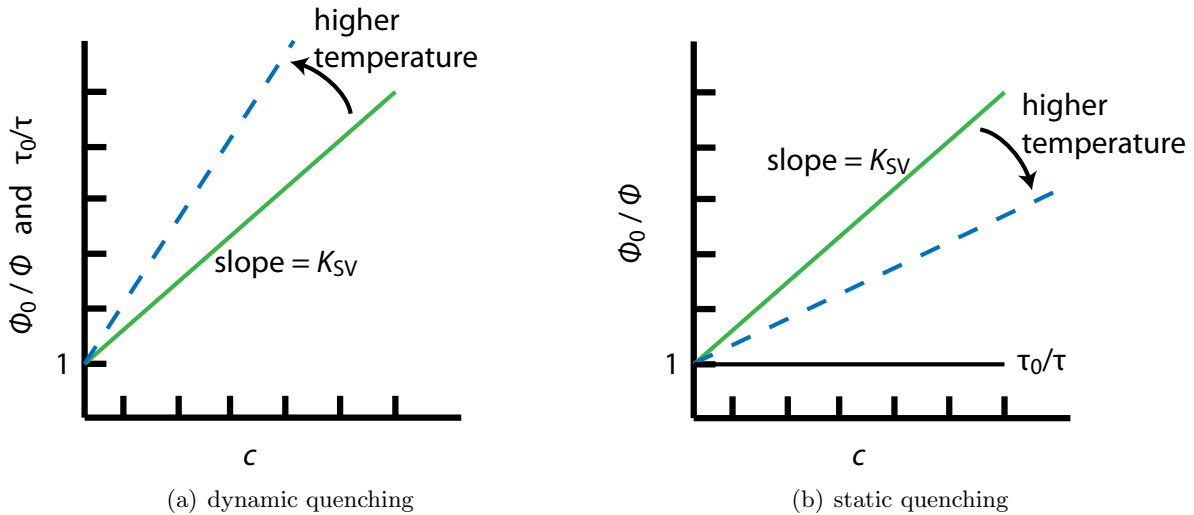


**Figure 2.8.:** Schematic drawing of two Stern-Volmer plots for dynamic (a) and static (b) quenching. The x-axis shows the quencher concentration  $c$ , the y-axis demonstrates the ratio of unquenched to quenched luminescence signal. Modified from Lakowicz [2006].

## 3. Methods

The first section of this chapter gives a short overview of two methods to visualize gas concentrations in water, especially the method used in this study to visualize local oxygen ( $O_2$ ) concentrations. Section 3.2 deals with the calibration of this technique. A mass balance method to measure the transfer velocity  $k_b$  of oxygen is described in Section 3.3. The method to measure the wind profiles is presented in Section 3.4.

### 3.1. Oxygen Concentration Imaging

There are two non-intrusive methods to visualize gas concentrations in the water-sided mass boundary layer: the pH-indicator method and the quenching method. Both methods are laser-induced fluorescence (LIF) techniques, where a laser excites a fluorophore which is solved in water. The excited molecules of the fluorophore emit luminescent light, which is observed with a detector such as a camera. A precursor experiment to the LIF technique was conducted by Hiby et al. [1967] to measure the distribution of gas concentrations in falling films.

The pH-indicator method finds its application in the detection of trace gases that react with water or the pH-indicator itself, resulting in a change of the photon flux emitted by the fluorophore. First gas exchange experiments using the pH-indicator method were conducted by Pankow et al. [1984]. Early visualizations in a wind-wave tank were presented by Jähne [1991] at the Second International Symposium on Gas Transfer at Water Surfaces. More recent results are documented in Münsterer and Jähne [1998], Asher and Litchendorf [2009], Herzog [2010], and Asher et al. [2012].

In this study, the quenching (Section 2.3.4) method is used, which is applied to detect gases, like  $O_2$ , that repress the phosphorescence of the excited fluorophore. This method is explained in detail in the next section.

#### 3.1.1. Oxygen Quenching Method

First measurements with the oxygen quenching method were presented by Wolff et al. [1991] and Duke and Hanratty [1995] at the Second and Third International Symposium on Gas Transfer at Water Surfaces, respectively. More recent measurements were conducted by Falkenroth [2007] and Walker and Peirson [2008] in wind-wave tanks and by Herlina and Jirka [2008] in a grid-stirred tank.

### 3. Methods

The O<sub>2</sub> quenching method takes advantage of the fact that the photon flux  $\Phi$  emitted by the fluorophore decreases in the presence of O<sub>2</sub> molecules. A description of the theoretical details of the quenching process was given in Section 2.3.4. The fluorophore used in this study is a Ruthenium (Ru) complex, described in Chapter 5.

The generalized Stern-Volmer equation (2.86) describes how the photon flux  $\Phi$  decreases with increasing O<sub>2</sub> concentration. The local O<sub>2</sub> concentration  $c$  is obtained from equation (2.86)

$$c = \left( \frac{\Phi_0}{\Phi} - 1 \right) \cdot \frac{1}{K_{SV} \cdot \epsilon_D} \quad (3.1)$$

by measuring the photon flux  $\Phi$ . The photon flux in absence of O<sub>2</sub> is denoted with  $\Phi_0$  and  $K_{SV}$  denotes the Stern-Volmer constant for the Ru complex and the quencher O<sub>2</sub>, which was measured in this study (Section 5.2.2). The damping factor  $\epsilon_D$  has to be determined by a calibration procedure, given in Section 3.2.2.

Not the absolute value of the photon flux  $\Phi$  but a value proportional to the photon flux  $\Phi$  is measured with the camera (Section 4.2.4). The proportionality factor is not determined as only the quotient of the photon flux without quencher  $\Phi_0$  and the photon flux  $\Phi$  has to be known. The term photon flux  $\Phi$  is used for the measured difference of the gray value and the dark value of the camera throughout this study.

An advantage of the quenching method over the pH-indicator method is that the absorbance of the fluorophore stays unchanged regardless of the concentration of the tracer. This simplifies the calculation of the local tracer concentration as the laser irradiance is independent of the tracer concentration in the preceding light path. A further advantage is that the quenching method constitutes a direct way to calculate the concentration of a tracer as no assumptions about diffusion constants of combined complexes have to be made (see [Herzog, 2010]).

#### 3.1.2. Constraint for the Laser Operation Mode

First experiments with the LIF technique were carried out with the laser in cw (continuous wave) mode. At a high laser irradiance  $E$ , the photon flux  $\Phi$  emitted by the fluorophore showed relative root mean square (RMS) fluctuations  $\Phi'_{RMS}/\bar{\Phi}$  on the order of 10%. This effect is presumably due to a temperature effect (see next section) and is unacceptable for our experiments. Measurements with a pulsed laser showed that the RMS fluctuations of the photon flux  $\Phi$  can be decreased to an acceptable level of  $\Phi'_{RMS}/\bar{\Phi}$  below 1%. Figure 3.1 shows two time series of the photon flux  $\Phi$  for the laser in the cw and in the pulsed mode with a duty cycle of 0.4% and a pulse length of 2 ms. The RMS fluctuation  $\Phi'_{RMS}/\bar{\Phi}$  are around 7% and 0.5% for the laser in cw mode and pulsed mode, respectively. This shows that pulsing the laser is a measure to avoid the unwanted fluctuations of the photon flux  $\Phi$ . This method was also used by Saylor [1995] to avoid photobleaching effects for any non-zero fluid velocity. The time interval between two

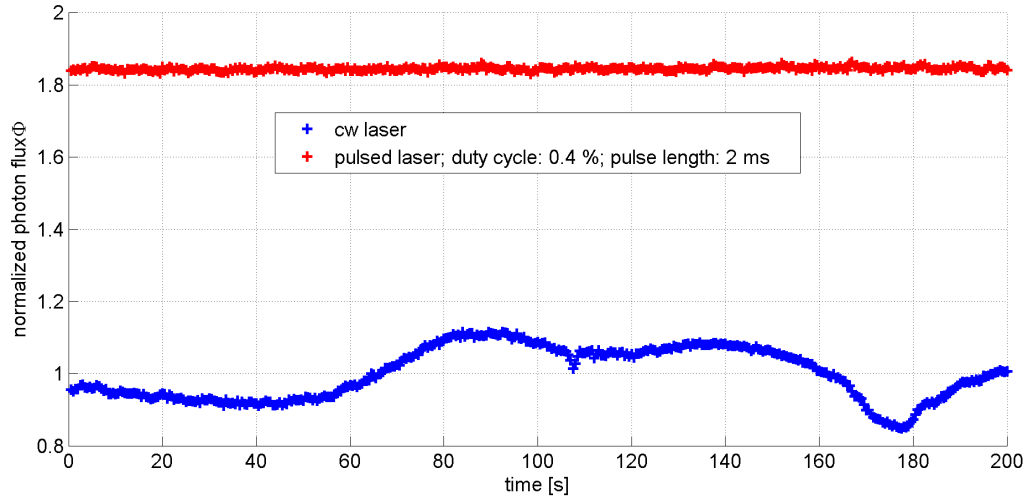


**Figure 3.1.:** Time series of the photon flux  $\Phi$  for the laser in the cw (continuous wave) mode and in the pulsed mode, measured with the LIF setup. Both time series are normalized on the mean photon flux  $\bar{\Phi}$  of the cw signal. For both measurements a non-zero fluid velocity was established in the water.

successive pulses  $\tau_{\text{off}}$

$$\tau_{\text{off}} > \frac{d}{v_1} \quad (3.2)$$

should be greater than the time that a fluid particle spends in the laser region where  $d$  denotes the laser beam diameter in flow direction and  $v_1$  denotes the local fluid velocity. A small beam diameter  $d$  is useful to keep the time interval  $\tau_{\text{off}}$  low. The appropriate time interval  $\tau_{\text{off}}$  depends on the local flow velocity and thus on the wind speed which drives the flow of the water. The higher the wind speed, the higher the flow velocity  $v_1$  and accordingly the time  $\tau_{\text{off}}$ .

In conclusion, pulsing the laser is necessary to avoid fluctuations of the photon flux  $\Phi$ . For a given pulse length  $\tau_{\text{on}}$  of the laser, the duty cycle of the laser has to be low enough to satisfy equation (3.2). In some cases, especially at low wind conditions equation (3.2) may not be satisfied locally. This leads to a lower photon flux  $\Phi$  than one would measure at a high flow velocity of the water, resulting in an overestimated  $\text{O}_2$  concentration, according to equation (3.1).

### 3.1.3. Effects Influencing the Precision

This section presents the effects that reduce the precision of the LIF method leading to errors in the averaged  $\text{O}_2$  concentration profiles.

**Temperature Effect** The water absorbing the laser light is locally heated. This leads to a change of the Stern-Volmer constant on the order of 3% per Kelvin (see Section 5.2.3). As the local temperature is not measured with the LIF method, the determined  $\text{O}_2$  concentration with equation (3.1) is defective. The influence of this effect is reduced to a minimum by pulsing the laser, as explained in the previous section.

### 3. Methods

**Defective Surface Detection** The surface position in every single LIF image is detected with an algorithm described in Section 8.2.2. The algorithm is capable of determining the position of the water surface with the precision of one pixel, corresponding to about  $6.2\ \mu\text{m}$  (Section 6.1.1). This leads to an error in the averaged concentration profiles. This effect only plays a role close to the water surface, when small-scale effects are being resolved. An example are the fluctuation concentration profiles in Section 9.5.

**Camera Noise** The camera used (Section 4.2.4) showed noise effects, additional to the usual camera SNR. Both effects are described in Section A.4.

## 3.2. Calibration Method for the LIF Measurements

The damping factor  $\epsilon_D$  and the photon flux  $\Phi_0$  in absence of  $\text{O}_2$  are both measured through a calibration procedure, which is explained in the Sections 3.2.2 and 3.2.3. For the calibration, the  $\text{O}_2$  concentration in the whole measuring section has to be set to a constant value and has to be determined with an established method (see Section 3.2.1).

### 3.2.1. Adjusting and Measuring the Oxygen Concentration

The  $\text{O}_2$  concentration in the water is changed directly with the equilibrator, described in Section 4.1.1. It is additionally changed indirectly by lowering the  $\text{O}_2$  concentration in the air. This is done by adding nitrogen ( $\text{N}_2$ ) to the air-space to replace the  $\text{O}_2$  molecules. Consequently, the  $\text{O}_2$  concentration in the water drops exponentially as it is proportional to the concentration in the air according to Henry's law (see equation (2.20)). The temporal and spatial mean  $\text{O}_2$  concentration in the water is measured using an oxygen probe, described in Section 4.1.1.

In the first step of every calibration, the equilibrator is switched on and  $\text{N}_2$  is added to the air space of the closed wind-wave tank until the  $\text{O}_2$  concentration in the water is close to zero. When the  $\text{O}_2$  concentration is low enough and stays constant, the first calibration measurement is performed. At each calibration measurement, the photon flux  $\Phi$  is observed with a camera (see Section 4.2), and the  $\text{O}_2$  concentration measured by the oxygen probe is documented.

By flushing small amounts of ambient air with equilibrium  $\text{O}_2$  concentration through the wind-wave tunnel, the concentration of  $\text{O}_2$  is stepwise increased. The time intervals between the flushing events must be long enough so that the water reaches equilibrium with the air concentration. Accordingly, the  $\text{O}_2$  concentration in the water also increases stepwise. Each time the  $\text{O}_2$  concentration in the water reaches a constant value, a calibration measurement is performed.

### 3.2.2. Determination of the Damping Factor

The maximum photon flux  $\Phi_{\text{max}}$  out of the volume element  $\Delta V$  is reached, when all molecules of the fluorophore are in the excited state ( $n^* = N$ ) and can be calculated analogous to equation

(2.83).

$$\Phi_{\max} = k_r \cdot N \cdot \Delta V \quad (3.3)$$

We obtain the photon flux  $\Phi$  relative to the maximum photon flux  $\Phi_{\max}$  by dividing the upper part of the equations (2.83) and (3.3) and including equation (2.80):

$$\frac{\Phi}{\Phi_{\max}} = \frac{E}{\frac{\gamma + k_q \cdot c}{\sigma_a} + E} \quad (3.4)$$

For simplification, the term  $E_{\text{sat}}^q$  is introduced here as the saturation irradiance with a quencher.

$$E_{\text{sat}}^q := \frac{\gamma + k_q \cdot c}{\sigma_a} \quad (3.5)$$

The relation between the saturation irradiance  $E_{\text{sat}}^q$ , with a quencher, and  $E_{\text{sat}}$ , without a quencher, can be calculated using equation (2.75):

$$E_{\text{sat}}^q = E_{\text{sat}} + \frac{k_q}{\sigma_a} \cdot c \quad (3.6)$$

Using equation (3.4) and definition (3.5), the photon flux  $\Phi$  can be written as

$$\Phi = \Phi_{\max} \cdot \frac{E}{E_{\text{sat}}^q + E}. \quad (3.7)$$

The laser power  $P$  of the laser diode is proportional to the laser irradiance  $E$ , with a proportionality factor of  $\alpha_P$  (in  $\text{J m}^2$ ).

$$P = \alpha_P \cdot E \quad (3.8)$$

The laser power  $P$  is available from a calibration, see Section 4.2.2. In order to calculate the laser irradiance  $E$ , the factor  $\alpha_P$  or rather the cross-sectional area of the laser power in the measuring section has to be known with a high precision. Since the laser irradiance  $E$  can only be calculated with a high uncertainty but the laser power data  $P$  is available, the equations (3.6) and (3.7) are rewritten using the laser power  $P$  instead of the laser irradiance  $E$ . With equation (3.8), we obtain out of equation (3.6) the  $\text{O}_2$  dependent saturation laser power  $P_{\text{sat}}^q$

$$P_{\text{sat}}^q = P_{\text{sat}} + \alpha_P \cdot \frac{k_q}{\sigma_a} \cdot c \quad (3.9)$$

and by rewriting (3.7) the photon flux  $\Phi$  depending on the laser power  $P$

$$\Phi = \Phi_{\max} \cdot \frac{P}{P_{\text{sat}}^q + P}. \quad (3.10)$$

As a first step to determine the damping factor  $\epsilon_D$ , the saturation laser power with quencher  $P_{\text{sat}}^q$  is measured for different  $\text{O}_2$  concentrations. This is done by applying different laser power

### 3. Methods

values  $P$  at every specific  $O_2$  concentration and measuring the photon flux  $\Phi$ . The saturation power  $P_{\text{sat}}^q$  and the maximum photon flux  $\Phi_{\text{max}}$  for each  $O_2$  concentration are obtained by fitting equation (3.10) to the measured data. A plot to visualize this procedure for one specific  $O_2$  concentration can be seen in Figure 5.3.

The next step in the calibration procedure of the damping factor  $\epsilon_D$  is the determination of the laser saturation power  $P_{\text{sat}}$  at a concentration of  $c = 0 \text{ mg L}^{-1}$ . The concentration of  $O_2$  in the wind-wave tank cannot be set to a value of absolute zero. One reason is that the  $O_2$  concentration in the air drops exponentially while the wind-wave tunnel is flushed with  $N_2$ . To reach a concentration of zero within the measurement precision, large quantities of  $N_2$  would be necessary. Another reason is that  $O_2$  is transported through leaks of the wind-wave tunnel into the air space (for the leakage rate refer to [Winter, 2011]). Therefore, the laser saturation power with quencher  $P_{\text{sat}}^q$  is determined for different concentrations of  $O_2$ , as previously described, and equation (3.9) is fitted to the data. The laser saturation power  $P_{\text{sat}}$  without quencher is gained as the offset of the linear fit function. The benefit of this method is that the value of the Stern-Volmer constant  $K_{\text{SV}}$  is not needed. To illustrate this step, a plot with the laser saturation power with quencher  $P_{\text{sat}}^q$  versus the  $O_2$  concentration is depicted in Figure 5.4. It should be noticed that the  $P_{\text{sat}}^q$  values are only needed to calculate the laser saturation power  $P_{\text{sat}}$  without  $O_2$ .

The damping factor  $\epsilon_D$  is obtained by rewriting equation (2.87) with laser power  $P$  instead of laser irradiance  $E$ :

$$\epsilon_D = \frac{P_{\text{sat}}}{P + P_{\text{sat}}} \quad (3.11)$$

#### 3.2.3. Determination of the Unquenched Photon Flux

Since the  $O_2$  concentration can not be set to a value of  $c = 0 \text{ mg L}^{-1}$  (see Section 3.2.2) another calibration method has to be used to get the photon flux  $\Phi_0$  in absence of  $O_2$ . The calibration photon flux  $\Phi_{\text{cal}}$  is measured at different  $O_2$  concentrations  $c_{\text{cal}}$ . An expression for the photon flux  $\Phi_0$  is obtained using the generalized Stern-Volmer equation (2.86) and inserting the calibration photon flux  $\Phi_{\text{cal}}$  and the calibration  $O_2$  concentrations  $c_{\text{cal}}$ :

$$\frac{1}{\Phi_{\text{cal}}} = \frac{1}{\Phi_0} \cdot (1 + K_{\text{SV}} \cdot \epsilon_D \cdot c_{\text{cal}}) \quad (3.12)$$

Fitting this equation to the measured inverse calibration photon flux  $\Phi_{\text{cal}}^{-1}$  over the calibration  $O_2$  concentration  $c_{\text{cal}}$  yields the photon flux  $\Phi_0$  as the inverse offset of the linear fit function.

This method is able to determine the photon flux  $\Phi_0$  without knowing the Stern-Volmer constant  $K_{\text{SV}}$  and the damping factor  $\epsilon_D$ . This fact leads to a high precision of  $\Phi_0$  as the errors of  $K_{\text{SV}}$  and  $\epsilon_D$  are not transmitted to the photon flux  $\Phi_0$ .

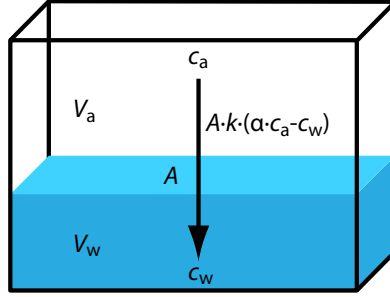


**Figure 3.2.:** Box model for an invasion experiment for the gas exchange between the air space with volume  $V_a$  and  $O_2$  concentration  $c_a$  and the water space with volume  $V_w$  and  $O_2$  concentration  $c_w$ . The transport of  $O_2$  takes place through the water surface area  $A$ . The amount of transported oxygen per time is indicated next to the arrow.

### 3.3. Mass Balance Method

The mass balance method to measure the transfer velocity  $k_b$ , integrated over fetch, in the linear wind-wave tunnel is presented in this section. We model the wind-wave tank with two boxes, one box being the water space with volume  $V_w$ , and the other being the air space with volume  $V_a$ , separated by the water surface  $A$ , see Figure 3.2. The  $O_2$  concentrations  $c_w$  and  $c_a$  are regarded being well mixed within the boxes. We assume a constant  $O_2$  concentration  $c_a$  in the air, because the amount of  $O_2$  molecules in the air space  $c_a \cdot V_a$  is much bigger than the amount  $c_w \cdot V_w$  in the water space. This is justified with the fact that the air volume is about a factor of 30 bigger than the water space (see Section 4.1.1), and that the solubility  $\alpha$  of  $O_2$  in water is on the order of 3% [Sander, 1999], leading to

$$\frac{V_a}{V_w \cdot \alpha} \gg 1. \quad (3.13)$$

Using this condition and the balance condition  $c_w = \alpha \cdot c_a$  (equation (2.20)), we obtain the stated condition

$$c_a \cdot V_a \gg c_w \cdot V_w. \quad (3.14)$$

The box model is described in [Jähne, 1980] for the nonsteady case with two coupled differential equations. Here, these equations can be uncoupled because of the condition  $\dot{c}_a = 0$  and we obtain an ordinary linear first order differential equation for the mass balance

$$V_w \cdot \dot{c}_w = k \cdot A \cdot (\alpha \cdot c_a - c_w). \quad (3.15)$$

With the initial condition that the concentration at time  $t = 0$  is  $c_0$ , the solution to the mass balance equation is

$$c_w(t) = \alpha \cdot c_a + (c_0 - \alpha \cdot c_a) \cdot \exp\left(-\frac{k}{h_{\text{eff}}} \cdot t\right), \quad (3.16)$$

with the effective height  $h_{\text{eff}} = \frac{V_w}{A}$  of the wind-wave tunnel.

### 3. Methods

#### 3.4. Measuring Method for the Wind Profiles

Wind profiles were measured at the Heidelberg linear wind-wave tunnel (Section 4.1.1) by an L-shaped Pitot tube with a differential pressure transducer<sup>1</sup>. The Pitot tube was moved in the vertical direction with a translation stage<sup>2</sup>. The wind velocity  $u$  is determined by the differential pressure of the Pitot tube  $p_{\text{diff}}$  and the air density  $\rho_{\text{air}}$  with the equation

$$u = \sqrt{\frac{2 \cdot p_{\text{diff}}}{\rho_{\text{air}}}}. \quad (3.17)$$

During the measurements, the air temperature and pressure was measured to calculate the precise air density  $\rho_{\text{air}}$ .

For the wind measurements, the top cover of the wind-wave tank was replaced by a cover plate with a slit along the wind direction in the center where the Pitot tube was passed through, allowing wind measurements at fetch positions between 40 cm and 240 cm. In order to have an undisturbed wind field, the open parts of the slit were sealed with inlays.

---

<sup>1</sup>differential pressure transducer: *DIFF-CAP* by Special Instruments with the specified measuring range of 0.5 mbar and accuracy of 0.25 % of full scale.

<sup>2</sup>translation stage by Owis

## 4. Setup

A description of the wind-wave tunnels used in this study is given in Section 4.1. The setup to measure oxygen ( $O_2$ ) concentrations in water is shown in Section 4.2.

### 4.1. The Wind-Wave Tunnels

Experiments presented in this study were performed in two different wind-wave tunnels at the Institute of Environmental Physics at the University of Heidelberg. The Heidelberg linear wind-wave tunnel was used for the LIF measurements (Section 7.3.1). The linear visualization-test wind-wave tunnel was used for the measurement of the Stern-Volmer constant  $K_{SV}$  (Section 5.2.2).

#### 4.1.1. The Heidelberg Linear Wind-Wave Tunnel

The Heidelberg linear wind-wave tunnel<sup>1</sup> was built by Dr. Alexandra Herzog and is described in detail in her thesis [Herzog, 2010]. This setup was further upgraded in the framework of this thesis. Figure 4.1 shows a schematic drawing of the side view of the tunnel. The linear tunnel satisfies experimental demands that none of the existing tunnels in the Heidelberg gas exchange lab does. The linear shape of the water segment leads to a logarithmic wind profile, which enables us to measure the friction velocity. The glass windows at the water segment allow perfect access for optical measurements from the bottom, the top, or the side of the water basin. The materials used at the inner side of the tunnel are all chemical resistant which allows for the use of acid gases. The current instrumentation and the properties of the tunnel are presented in this section.

#### General Properties

The tunnel has a length of 7.7 m and is 1.5 m high, including the air circulation system, as shown in Figure 4.1. The closed system of the tunnel has an air volume of about  $3.3\text{ m}^3$  and a water volume of about 115 L including the water in the bypasses. The elements of the wind guiding system are fabricated out of foamed PVC<sup>2</sup>, covered with PTFE<sup>3</sup> foil, leading to a light weight and chemical resistant device.

---

<sup>1</sup>The tunnel was formally known as LIZARD (linear strong acid resistant device).

<sup>2</sup>PVC is the acronym for Polyvinylchlorid which is a widely used plastic. Here, the brand *Kömacel* by the manufacturer Kömerling Plastics was used.

<sup>3</sup>PTFE stands for Polytetrafluoroethylene and is best known for the brand name *Teflon*.

4. Setup

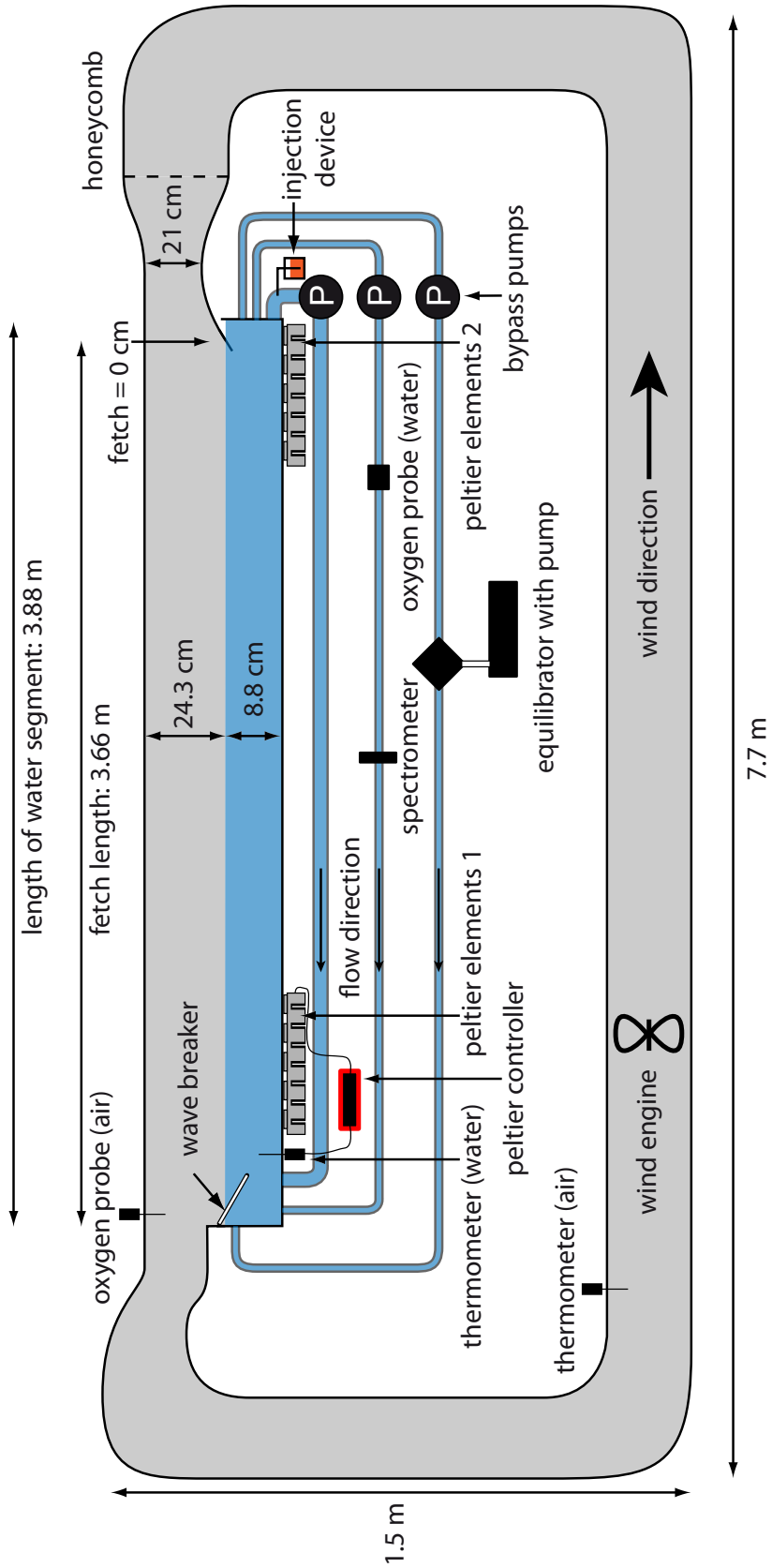
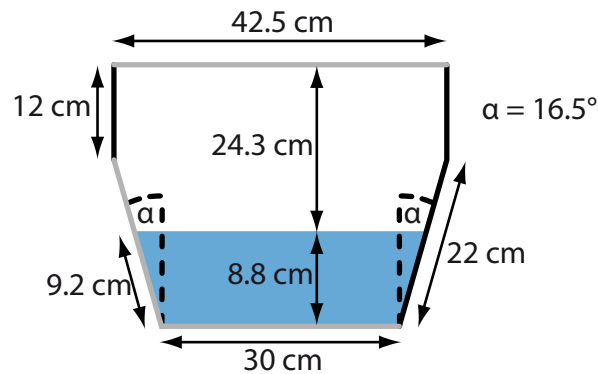


Figure 4.1.: Sketch of the side view of the Heidelberg linear wind-wave tunnel.



**Figure 4.2.:** Cross section of the side view normal to the air flow of the water segment of the tank. The gray sidewalls are out of glass, the black ones out of nontransparent foamed PVC material.

### The Wind Engine and Wind Guidance

The wind engine is a seven-blade axial rotor *HF A 400-D* manufactured by Hürner Funken. The parts having contact with the inner air space of the tunnel are made out of the chemical resistant synthetic material PPS<sup>4</sup>. An electronic frequency converter<sup>5</sup>, adjusts the rotation frequency  $F$  of the wind engine in a range from 0 Hz to 50 Hz. In the following text the term wind engine frequency is used for the rotation frequency.

The air flow is guided to the water segment via the flow bending units. Unwanted fluctuations normal to the mean air flow are reduced in the honeycomb, named for the inner cell-structure of the element, with a cell size of 3 cm. After the honeycomb, the air flow is contracted in the jet inlet leading to an acceleration of the flow, with a contraction ratio of 3.35. The purpose of the jet inlet is to reduce inhomogeneities of the flow by contraction of the stream lines.

### The Water Segment

The water segment without the bypasses contains 111.2 L of water<sup>6</sup> with a surface area of about 1.28 m<sup>2</sup>. The maximum fetch measures 3.66 m, but the glass windows allow optical measurements only between 35 cm and 255 cm. The sidewalls of the water segment consist of transparent and nontransparent sections, which are fabricated out of borosilicate glass<sup>7</sup> with a thickness of 6.5 mm and out of nontransparent foamed PVC material, covered with PTFE foliage, respectively. A sketch of the cross section of the water segment is depicted in Figure 4.2. The sketch shows the transparent (in gray) and the nontransparent (in black) parts of the walls. One of the sidewalls is out of glass and tilted so that the optical axis of an oblique mounted camera is perpendicular to the glass window. The reason for this setup becomes obvious in Section 4.2.1. A wave breaker

<sup>4</sup>PPS is the acronym for Polyphenylene sulfide, a heat and chemical resistant plastic.

<sup>5</sup>frequency converter: type *Sinamics G110* by Siemens

<sup>6</sup>The water volume given is for the standard fill depth of the tank, indicated with a mark and reproducible through a level drain. This standard depth was used throughout this study, including the wind and the wave measurements.

<sup>7</sup>borosilicate glass: type *Borofloat 33* by Schott

#### 4. Setup

at the end of the water segment made out of PTFE tubes suppresses the reflection of waves.

#### The Bypasses

Three bypasses are depicted in Figure 4.1. The uppermost bypass is the mixing bypass with a water volume of about 3.5 L. The purpose of this bypass is to generate a recirculation in the channel so that tracers and the injected fluorophore (the Ru complex, see Section 5) get equally distributed in the water. In the case of an operating Peltier temperature control, the circulation of the water is important in order to equilibrate the temperature in the tunnel. Liquid tracers and other substances can be injected by a dedicated device in the bypass right before the pump to achieve a fast mixing with the water in the basin. To drive the flow in the mixing bypass a centrifugal pump<sup>8</sup> is used, having a discharge flow of  $80 \text{ L min}^{-1}$ . The same electronic frequency converter as used for the wind engine adjusts the rotation frequency of the pump. Arrows in the mixing bypasses in Figure 4.1 indicate the flow direction.

Each of the two smaller bypasses contains a water volume of about 350 mL. One of them contains two important measuring devices, the oxygen probe and an absorption spectrometer, the other one is the deoxygenation bypass containing an equilibrator with a pump. The purpose of this bypass is to deoxygenate the water in the wind-wave tunnel. The three later devices are described in the following paragraph. Both of the smaller bypasses contain a magnetically coupled rotary pump<sup>9</sup> with a discharge flow of  $14 \text{ L min}^{-1}$ .

#### Instrumentation on the Water Side

The four instruments installed on the water side of the tunnel are described in this section. Except for the thermometer, all devices are installed in the bypasses.

**Thermometer (water side)** The temperature of the water is measured with two precision thermometers<sup>10</sup>, one upstream and one downstream. The sensors used are *PT100* diving detectors with a tolerance of  $\pm 0.03 \text{ K}$  at  $0^\circ\text{C}$ . The thermometers are connected with a peripheral interface adapter<sup>11</sup>, that can be read out via the serial interface.

**Oxygen Probe (water side)** The oxygen probe<sup>12</sup> is integrated in the measuring bypass to measure the  $\text{O}_2$  concentration. The detection limit is  $0.01 \%$   $\text{O}_2$  (volume percent) and the range of the measurement varies from  $0.05 \%$  to  $300 \%$  air saturation. The temperature in the probe is measured simultaneously to correct for the temperature dependence of the solubility of  $\text{O}_2$ . Interestingly, the measurement principle of the probe relies on the same method (the  $\text{O}_2$  quenching method (Section 3.1.1)) as used in this thesis to measure  $\text{O}_2$  concentrations. It should be noted here that the commercial oxygen probe only measures

---

<sup>8</sup>centrifugal pump: type *MPN 101* by Schweiker

<sup>9</sup>rotary pump: RS-Components

<sup>10</sup>precision thermometers: type *GMH 3710* by Greisinger

<sup>11</sup>peripheral interface adapter: type *GRS 3105* by Greisinger

<sup>12</sup>oxygen probe: type *Visiferm DO 120* manufactured by Hamilton

the temporal and spatial mean  $O_2$  concentration, whereas the LIF method (see Section 3.1) is able to measure with a high temporal and spatial resolution. Nevertheless, the commercial oxygen probe is essential for the calibration of the photon flux  $\Phi_0$  in absence of  $O_2$  in Section 6.3.

**Spectrometer** The absorption spectrometer is installed in the measuring bypass in order to measure the absorption spectrum of the water. With this setup, the absorbance of the fluorophore, the Ru complex (Section 5.1), is measured in order to adjust the optimal concentration (see Section 4.2.1). The setup consists of a blue LED having a FWHM (full width at half maximum) emission between 400 nm and 470 nm. The light is focused and passes through a cuvette, which is flushed by the water stream in the bypass, with an absorption path in the water of 5 cm. After passing through the cuvette, the light is focused with a second lens on a spectrometer<sup>13</sup> covering the visible region. The absorbance is computed using the law of Lambert-Beer, see equation (4.2).

**Equilibrator** The original application of the equilibrator<sup>14</sup> membrane oxygenator is in the medical field to enrich the blood with  $O_2$  and to extract carbon dioxide. Its function is based on a hydrophobic membrane in the equilibrator with a surface area of  $1.8 \text{ m}^2$  that is permeable for gases but not for liquids. By reducing the pressure in the gas phase of the equilibrator with a membrane pump<sup>15</sup>, the dissolved gases diffuse from the water-side to the air-side. In the tunnel, the equilibrator is used to deoxygenate the water.

### Instrumentation on the Air Side

The three sensors for the air-related analysis are described here. They are read out together with two devices on the water side (the thermometer and the oxygen probe) using a peripheral interface adapter<sup>16</sup> with five channels.

**Thermometer (air side)** The temperature of the air space in the tunnel is measured with the same precision thermometer that is used on the water-side. The sensor used is a *PT100*. The air temperature is needed to calculate a precise air density for the measurement of the wind speed in Section 7.2.1.

**Oxygen Probe (air side)** The oxygen probe<sup>17</sup> installed on the air-side with an  $O_2$  sensor<sup>18</sup> has a range from 0% to 100% air-sided  $O_2$  partial pressure. The  $O_2$  concentration in the air is needed for the calibration of the LIF method (see Section 3.2). To adjust different  $O_2$  values in the water, the air-sided  $O_2$  concentration has to be varied and monitored.

---

<sup>13</sup>spectrometer: Ocean Optics *USB4000*

<sup>14</sup>equilibrator: Jostra Quadrox, Maquet

<sup>15</sup>membrane pump: type *N 820.3*, KNF Neuberger

<sup>16</sup>peripheral interface adapter: type *GRS3105*, Greisinger

<sup>17</sup>oxygen probe: *GMH3690*, Greisinger

<sup>18</sup>oxygen sensor: type *GGO370*, Greisinger

## 4. Setup

**Pressure Sensor** The pressure sensor<sup>19</sup> measures the static pressure inside the wind-wave tunnel with a resolution of 1 mbar. The static pressure inside the tunnel is crucial for the calculation of the air density for the wind speed measurement in Section 7.2.1.

### Peltier Temperature Control

On the bottom of the water segment, two Peltier temperature control units are attached to control the water temperature, one at fetch = 0 cm and the other at the end of the water segment (see Figure 4.1). The bottom of the tank at the positions where the cooling units are mounted consists of aluminium to provide a sufficient thermal conduction. The peltier elements are pressed against the aluminium with a cooling element ( $380 \times 280 \times 50 \text{ mm}^3$ ). On both sides of the peltier elements, heat conducting foils optimize the heat transport to the aluminium plate on one side and to the cooling element on the other side. A tangential fan generates air flow through the ribs of the cooling element to improve the heat exchange with the room temperature.

Each of the two Peltier temperature units contains 24 Peltier elements<sup>20</sup>. Six Peltier elements are connected in series forming one line. Four lines are parallel connected on both of the two Peltier units. A Peltier controller<sup>21</sup> supplies the 48 peltier elements on the two cooling units, using a PID (proportional-integral-derivative) controller. Data sheets to the Peltier elements can be found in the appendix of Winter [2011]. The Peltier temperature control is able to keep the temperature of the water in the tank constant with a precision of  $\pm 0.1 \text{ K}$ .

### 4.1.2. The Test Wind-Wave Tunnel

The test wind-wave tunnel allows tests of new measurement techniques because of its good optical access from each side of the water segment through the glass walls. It was used for the measurement of the Stern-Volmer constant  $K_{SV}$  (see Section 5.2.2), because of its small water volume of 22 L and air volume of about 220 L. Those small volumes allow a faster mixing of water and air space, the usage of smaller amounts of added gases, and the adjustment of a wider temperature range compared to the Heidelberg linear wind-wave tunnel. A detailed and complete description of the test wind-wave tunnel is given in Winter [2011] and a German version in Warken [2010]. To provide an idea of the tunnel's geometry, a technical drawing of the tunnel and its water segment is given in Figure 4.3. The wind-wave tunnel has a length of 4 m, a width of 1 m, and a height of 1.5 m.

The temperature Peltier cooling of the test tunnel was built during the course of this study. The cooling unit is able to adjust the temperature to a precision of  $\pm 0.1 \text{ K}$  and reach temperatures between  $17^\circ\text{C}$  and  $27^\circ\text{C}$  for a room temperature of about  $22^\circ\text{C}$ . The limits of the cooling unit are important for the measurement of the temperature dependence of the Stern-Volmer constant  $K_{SV}$  (see Section 5.2.3).

---

<sup>19</sup>pressure sensor: type *GMSD 1.3 BA* with *GMH3110*, Greisinger

<sup>20</sup>Peltier elements: type *QC-127-2.0-15.0M*, Cooltronic

<sup>21</sup>Peltier controller: type *TC2812*, Cooltronic

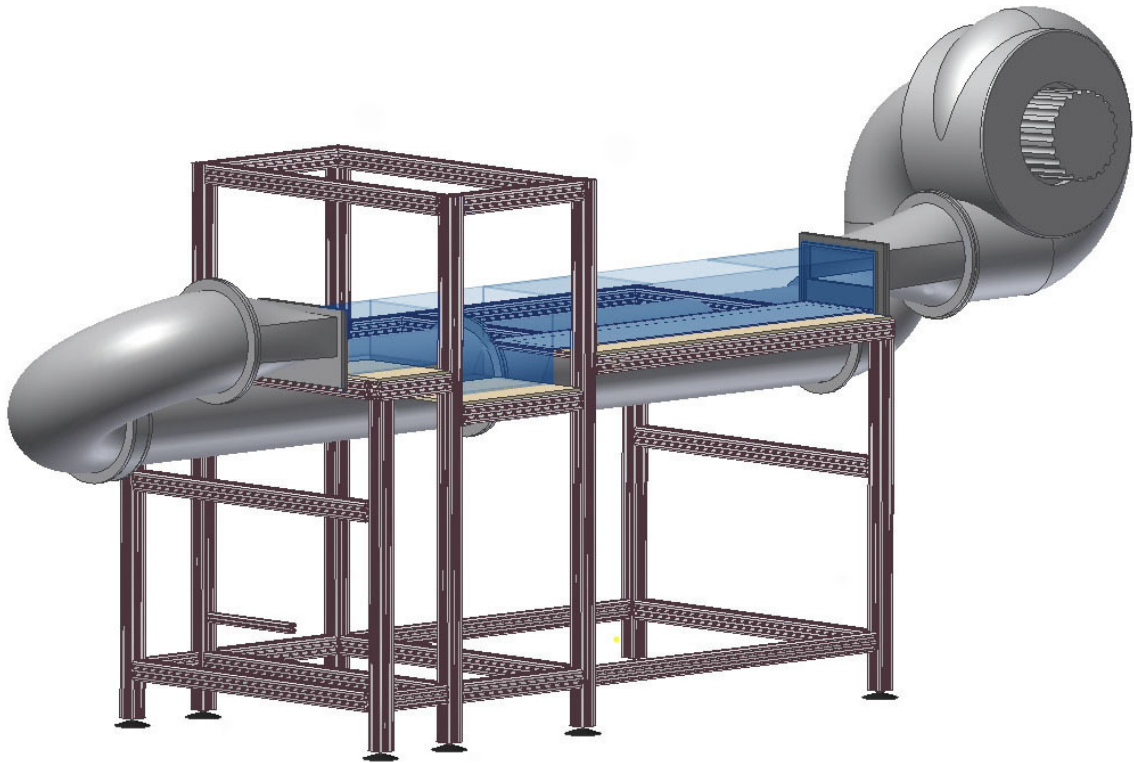


Figure 4.3.: 3-D sketch of the test wind-wave tunnel with the water segment depicted in blue, from Warken [2010].

## 4.2. The LIF Setup

The setup of the laser-induced fluorescence (LIF) method (see Chapter 3.1) is described in this section. It was used at both wind-wave tunnels mentioned in Section 4.1. The most important constituents in the LIF setup are the laser (see Section 4.2.2), the water with the solved fluorophore (the Ru complex, see Section 5.1), and a camera (see Section 4.2.4).

### 4.2.1. General Description

Figure 4.4 shows a sketch of the LIF setup as it was mounted at the Heidelberg linear wind-wave tunnel during the measurements. The laser beam (blue line) is focused with a beam expander (see Section 4.2.3), deflected with a mirror into the water segment, and absorbed by the Ru complex, which is solved in the water. The excited molecules of the Ru complex emit phosphorescence photons (red line in Figure 4.4) which are detected with a camera. The presence of  $O_2$  molecules next to excited molecules of the fluorophore leads to a reduction of the photon flux  $\Phi$  due to collisional quenching (see Section 2.3.4). Employing this quenching effect, local  $O_2$  concentrations along the laser beam are measured, using the general Stern-Volmer equation (2.86) and the measured Stern-Volmer constant (see Section 5.2.2).

**Laser from Below the Tank** The laser beam enters the water segment from below the tank. An illumination from below guarantees that the laser beam is always at the same position in

#### 4. Setup

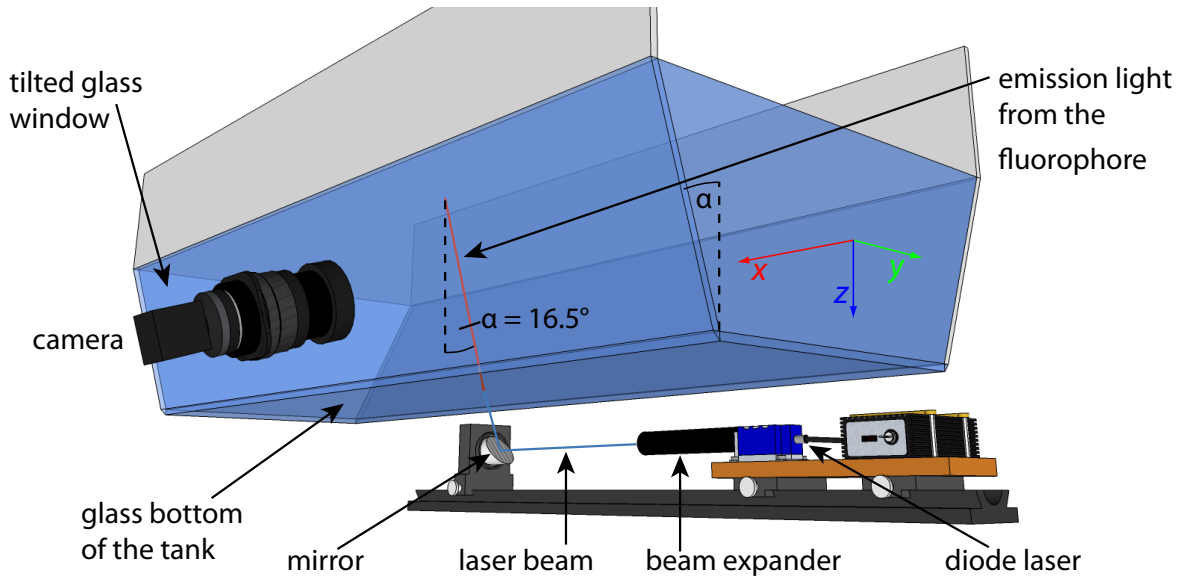


**Figure 4.4.:** Sketch of the LIF setup, showing a part of the water segment of the Heidelberg linear wind-wave tunnel, the laser, and the camera. The coordinate system used in this study is shown. The  $x$ -,  $y$ -, and  $z$ -axes depict the wind-direction, the horizontal cross-wind direction, and the depth, respectively. Parts of this figure are modified from Warken [2010].

the water segment and in the depth of focus of the camera. The laser line in the water is tilted about  $16.5^\circ$  in the  $y$ -direction so that it is parallel to the side window. This is necessary as the laser line has to be in the focal plane of the camera which is also tilted. The reason for the tilted camera becomes obvious in the next paragraph.

If the laser was mounted above the water surface, as realized in Herzog [2010], the laser beam would be diffracted at the water surface due to waves. This would cause the laser beam to be out of the camera focus and in cases of a high surface slope out of the camera's field of view.

**Tilted Side Window** The side window of the wind-wave tank with optical access to the camera is tilted (see Figure 4.4). The reason for this setup is that the camera must observe the  $O_2$  concentration profile from a tilted angle in order to see the intersection point of the water surface and the profile even at wavy conditions up to a maximum angle, described in the next paragraph. The camera lens has to be parallel to the glass window of the wind-wave tank in order to avoid optical aberrations.

**Surface Slope Limit** If the surface slope  $s_y$  at the intersection point of the surface and the illuminated concentration profile in the  $y$ -direction is too high, the upper part of the concentration profile is not visible (see Figure 4.5). The camera is tilted by the angle  $\delta$ . The necessary condition that the concentration profile up to the surface can be seen is:

$$s_y < \delta \quad (4.1)$$

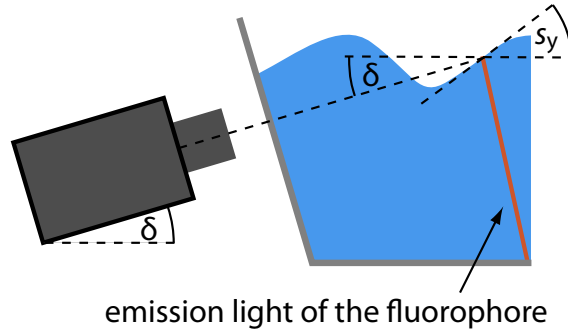


**Figure 4.5.:** Sketch of the limiting case where the surface is not visible. The surface is hidden if the slope  $s_y$  of the surface at the intersection point of the laser and the water surface is greater than the camera angle  $\delta$ .

Even if this condition is fulfilled, the surface might not be visible, if the water surface crosses the optical axis of the camera before the concentration profile. Regarding this case, the sufficient condition to see the concentration profile up to the water surface is that equation (4.1) is fulfilled for all points on the water surface.

**Optimal Fluorophore Concentration** As the laser beam enters the tank from below, the laser irradiance  $E$  decreases due to absorption by the fluorophore along the beam path  $z_b$ , starting with a maximum laser irradiance  $E_0$  at the exit of the laser diode. The exponential decay of the laser irradiance is described by the law of Lambert-Beer with the exponential extinction coefficient  $\epsilon_{\text{exp}}$  of the fluorophore and the concentration  $c$  of the fluorophore.

$$E(c, z_b) = E_0 \cdot \exp^{-\epsilon_{\text{exp}} \cdot c \cdot z_b} \quad (4.2)$$

In order to have a maximum signal at the water surface, the concentration  $c$  of the fluorophore has to be optimized. To derive the ideal concentration of the fluorophore, the concentration dependence of the photon flux  $\Phi$  is calculated. The photon flux  $\Phi$  is proportional to the number of absorbed laser photons:

$$\Phi(c, z) \propto \frac{\partial E(c, z)}{\partial z} = -\epsilon_{\text{exp}} \cdot c \cdot E_0 \cdot \exp^{-\epsilon_{\text{exp}} \cdot c \cdot z} \quad (4.3)$$

The maximum photon flux  $\Phi$  at the surface after distance  $z_0$  is reached when the partial derivative of the photon flux by the concentration is zero:

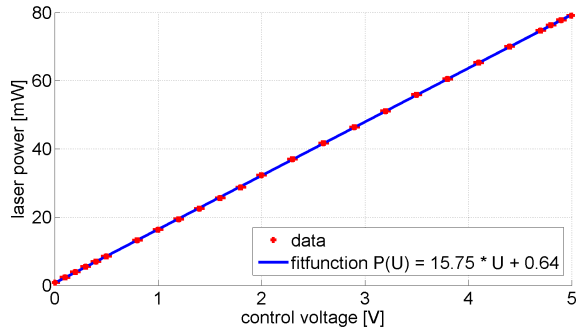
$$\frac{\partial \Phi(c, z = z_0)}{\partial c} \propto 1 - \epsilon_{\text{exp}} \cdot c \cdot z_0 \quad (4.4)$$

The result for the optimal concentration  $c_{\text{opt}}$  to maximize the laser irradiance at the water surface is

$$c_{\text{opt}} = \epsilon_{\text{exp}}^{-1} \cdot z_0^{-1}. \quad (4.5)$$

This implies that the laser irradiance  $E(c_{\text{opt}}, z_0)$  at the water surface has decreased to a value of  $E_0 \cdot \exp^{-1}$ .

#### 4. Setup



(a) laser power calibration



(b) the NOVAPRO laser module

**Figure 4.6.:** (a) Laser power calibration measured with a laser power meter by *NEWPORT*. (b) Picture of the laser head and the laser controller (from the laser data sheet).

The product of the concentration  $c$  and the exponential extinction coefficient  $\epsilon_{\text{exp}}$  is measured with the absorption spectrometer installed in the measuring bypass of the tunnel.

#### 4.2.2. The Laser

The laser used in this study is a diode laser<sup>22</sup> with a wavelength of  $445 \pm 5$  nm, a maximum laser power of about 79 mW, and a divergence angle smaller than 0.9 mrad. The laser output power is regulated by a controller with an input control voltage between 0 V and 5 V.

Figure 4.6(a) shows the linear relation between the output power and the control voltage. The laser head ( $60 \times 31 \times 31.5$  mm<sup>3</sup>) and the controller ( $85 \times 60 \times 28$  mm<sup>3</sup>) are shown in Figure 4.6(b). The compact design of the laser allows the usage of the laser at places which are difficult to access. To ensure a stable output wavelength and beam shape, the laser is equipped with a temperature control unit.

The control voltage at the input of the laser controller can be modulated with a frequency up to 200 kHz. During the measurements, the laser was pulsed using a signal generator with pulse rates between 0.5 kHz and 1.2 kHz to avoid unwanted signal variations (see Section 3.1.2).

Figure 4.7 shows the beam shape without any focusing element at a distance of 24 cm from the beam exit. The beam profile was measured by positioning the laser in front of a CMOS camera<sup>23</sup> without camera lens and mounting two mirrors, one reflecting mirror and one absorbing mirror, in front of the camera detector. The beam has a Gaussian shape in the  $y$ -dimension and a non-Gaussian shape in the  $x$ -dimension. The following section shows that the laser beam can be well focused to a FWHM value below 70  $\mu\text{m}$  and 31  $\mu\text{m}$  in the two dimensions with a beam expander.

<sup>22</sup>diode laser: type *NOVAPRO-450-75* by RGB Lasersysteme

<sup>23</sup>camera: Basler *aca2500-14gm*; pixel size 2.2  $\mu\text{m}$

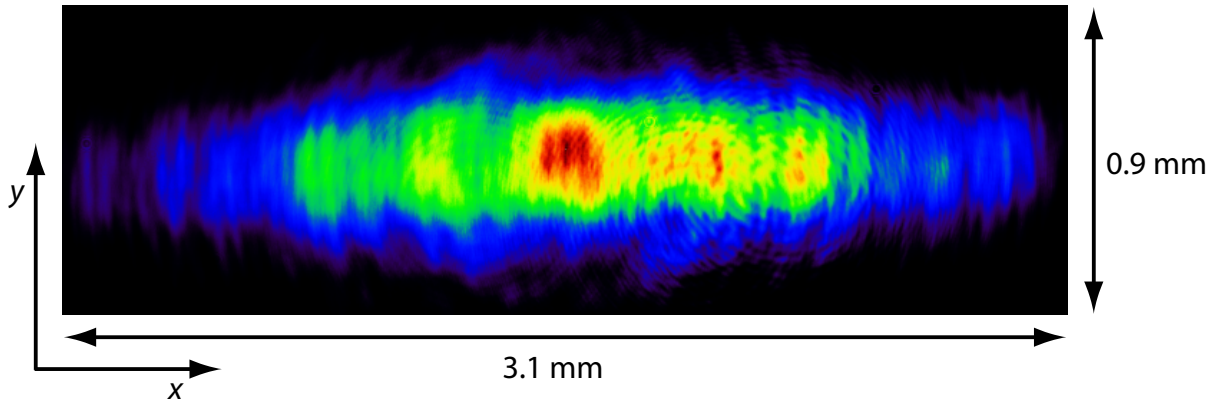


Figure 4.7.: Cross section of the laser beam measured with a self-build beam profiler.

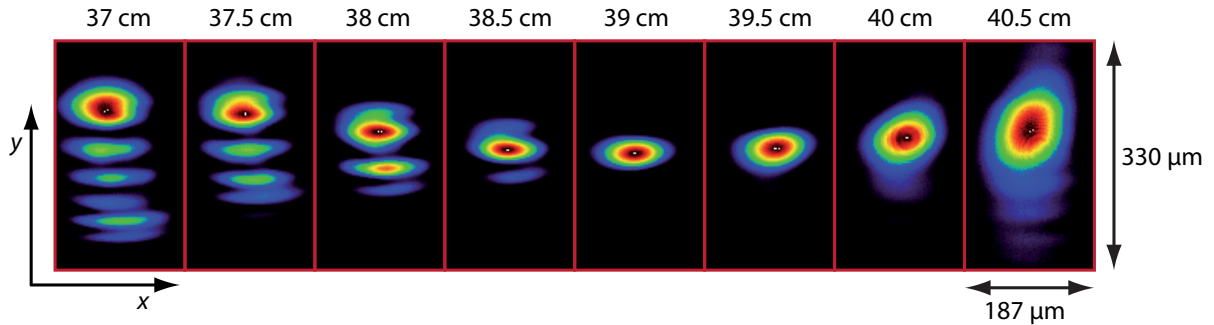


Figure 4.8.: Cross sections of the laser beam collimated with the beam expander at different distances on the optical axis. The distances measured from the exit of the beam expander are written above the images. The pictures shown are all normalized to the value of the peak. The cross sections were recorded with the same beam profiler as described in Section 4.2.2.

### 4.2.3. The Beam Expander

The purpose of the beam expander is to focus the laser in the measuring section between the water surface and about 1 cm beneath the surface. This is important for three reasons: i) The laser beam has to be focused to achieve a high depth resolution. For an unfocused beam, the depth resolution is low because the signal in one camera pixel originates from different water depths. ii) Focusing is important to reach a high laser irradiance leading to a good signal-to-noise ratio (SNR) of the measured photon flux  $\Phi$ . iii) Further, the water surface is much easier to detect with a focused beam in contrast to a wide beam (see Section 8.2.2).

The beam expander which is mounted on the laser exit consists of two achromatic lenses in a Kepler telescope [Hecht, 2009] setup. The laser light first passes through a lens with a focal distance of  $f = 30$  mm. At a distance of 10.5 cm from the first lens, the second lens with  $f = 60$  mm is mounted. This setup enables to vary the position of the beam waist from infinity down to 6 cm after the second lens by changing the distance between the two lenses. Figure 4.8 shows the cross section of the laser beam at different distances from the beam expander in steps of 5 mm starting at 37 cm. Compared to Figure 4.7, the pictures in this figure are turned by 90 degrees. The figure shows that the  $x$ -dimension has a Gaussian shape with a nearly constant

#### 4. Setup

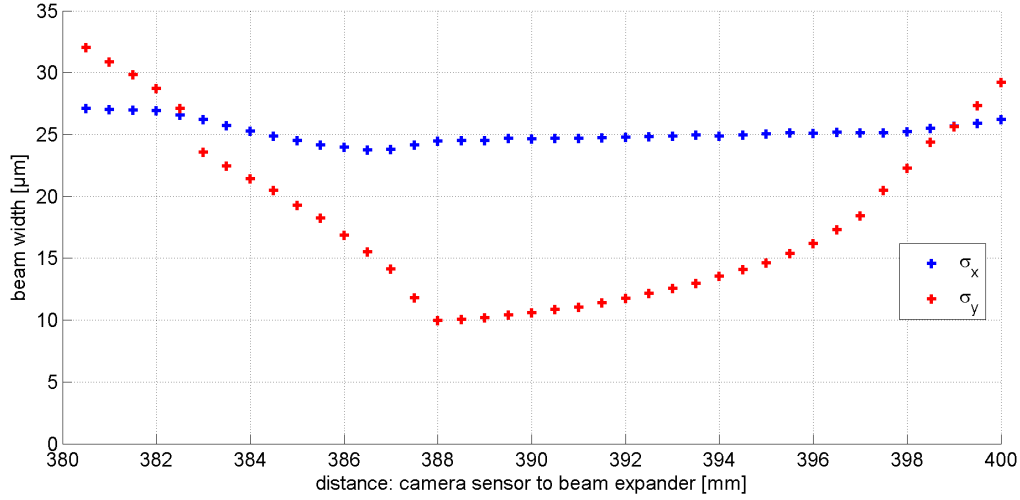


**Figure 4.9.:** Plot of the standard deviation of the beam cross section measured at different distances to the beam expander. The  $x$ -dimension is the Gaussian mode, the  $y$ -dimension the non-Gaussian mode. For the measurements, the part from about 386 mm to about 396 mm was used.

width for the depicted pictures. The  $y$ -dimension shows a stripe structure at a distance of 37 cm, which is focused on a single spot at a distance of 39 cm.

Cross sections as the ones shown in Figure 4.8 of the beam were recorded at 0.5 mm intervals. This was performed by shifting the beam profiler described in Section 4.2.2 with a translation stage over the specified range. The standard deviation  $\sigma$  of the two main axes was determined using the image processing software Heurisko<sup>®</sup>. The result of this measurement for distances from 38 cm to 40 cm is shown in Figure 4.9. The standard deviations at the beam waist correspond to FWHM values of 70  $\mu\text{m}$  and 31  $\mu\text{m}$  for the  $x$ - and the  $y$ -dimension, respectively. The section between 386 mm and 396 mm shows a standard deviation  $\sigma_y$  and  $\sigma_x$  below 20  $\mu\text{m}$  and 25  $\mu\text{m}$ , respectively. This range was used for the measurements, setting the beam waist to the water surface. The laser was oriented so that the camera sees the Gaussian mode with a constant width over the measuring volume. Measuring the laser beam width over the distance from the beam expander was crucial for the optimization of the beam expander and to estimate the error in the height of the concentration profiles.

#### 4.2.4. The Camera

The *acA2000-340km* manufactured by Basler is a monochrome CMOS camera. It was chosen for several reasons listed below.

**Pixel Size** The size of the camera's pixels is 5.5  $\mu\text{m} \times 5.5 \mu\text{m}$ . Together with the camera macro lens used (see Section 4.2.5), this leads to an optical pixel resolution of the same order.

**Number of Pixels** The camera's *progressive scan CMV2000* CMOS sensor features a resolution of 1088 pixels  $\times$  2048 pixels. The full width of the 2048 pixels each line is used for the

measurements. Only 50 out of the 1088 lines are read out for the measurements, because a region of this size is sufficient to image the laser line, which is used in this experiment.

**Speed** The refresh rate of the camera at full frame is 340 fps (frames per second). The rate grows by decreasing the number of vertical rows to read out. Using 50 lines, a maximum refresh rate of 1.9 kHz was achieved.

**Global Shutter** The global shutter of the camera guarantees that the exposure time for all pixels is the same. In contrast to a rolling shutter, there is no time delay between the recorded information of different pixels.

**External Trigger** Besides the free-run mode and a software-based trigger, the camera features an external trigger input. This option was used for the measurements. The camera was triggered with a signal generator that also triggered the laser so that the acquisition time of the camera overlaps with the laser pulses.

**Size** The camera's compact size of  $43.5 \times 29 \times 29 \text{ mm}^3$  enables the user to install the camera at sites that are difficult to access if the lens is small enough.

The pictures were saved with a pixel bit depth of 10 bits. The relation between the gray value that the camera observes and the irradiation (in photons per pixel) shows a good linearity with a deviation from the linear curve below 0.4% (see A.5). Measurements of the linear response were conducted at the HCI (Heidelberg Collaboratory for Image Processing) according to the EMVA 1288 standard [Group, 2010].

#### 4.2.5. The Camera Lens

The camera lens used for the measurements is a *AF Micro-Nikkor 200 mm 1:4 D*. It was chosen because of its good resolution and a large working distance of 260 mm for a macro lens. The measurements of the resolution are shown in Section 6.1.2. A working distance greater than about 150 mm was necessary in order to be able to measure at the center of the water segment, as Figure 4.2 visualizes.



# 5. Characterization of the Ruthenium Complex Indicator

This chapter shows results of measurements to verify the influence of saturation effects of the fluorophore used in this study on the quenching efficiency. Here, a ruthenium (Ru) complex was used to measure water-sided oxygen ( $O_2$ ) concentrations. The general properties of the Ru complex are presented in Section 5.1. To determine precise  $O_2$  concentrations, the quenching characteristics of the Ru complex were measured (Section 5.2). The efficiency of the quenching effect depends on the laser irradiance, as could be confirmed experimentally in Section 5.2.2. The generalized Stern-Volmer equation (2.86), which describes the dependency of the photon flux  $\Phi$  of an excited fluorophore on the concentration  $c$  of a quencher, was tested with the measured data, see Section 5.2.2. The Stern-Volmer constant  $K_{SV}$  and its dependence on temperature was measured, see Sections 5.2.2 and 5.2.3. Section 5.3 shows a measurement of the vulnerability of the Ru complex to photobleaching effects.

## 5.1. General Properties

In this study, the complex  $[Ru(dpp(SO_3Na)_2)_3]Cl_2$ , a water-soluble fluorophore, is used. Three ligands  $dpp(SO_3Na)_2$  are attached to the metal Ru. The ligand  $dpp(SO_3Na)_2$  is a disulfonated derivate of 4,7-diphenyl-1,10-phenanthroline (dpp). A schematic drawing of the complex is shown in Figure 5.1. The water soluble sulfonated derivate  $[Ru(dpp(SO_3Na)_2)_3]Cl_2$  of the oxygen probe  $[Ru(dpp_3)]Cl_2$  was first reported by Castellano and Lakowicz [1998], and is now widely used as an oxygen indicator. They report a lifetime of the unquenched Ru complex of 3.7  $\mu s$ . The Stern-Volmer constant  $K_{SV} = k_q \cdot \tau_0$  depends on the lifetime of the unquenched fluorophore, as described in equation (2.85). This intermediate lifetime between fluorescence and phosphorescence is long enough to have significant quenching effects and short enough to have significant emission light. Hence, the Ru complex is an ideal  $O_2$  indicator in water.

The measured absorption and emission spectra of the Ru complex are shown in Figure 5.2. During the measurement of the absorption spectrum<sup>1</sup>, the  $O_2$  concentration in the solution was in equilibrium with the room concentration. The existence of  $O_2$  in the water does not change the absorption spectrum.

For the measurement of the emission spectrum<sup>2</sup>, the Ru complex was excited by a laser with

---

<sup>1</sup>used spectrometer for the absorption spectrum: HP 8453 E UV-visible

<sup>2</sup>used spectrometer for the emission spectrum: Ocean Optics 2000+

## 5. Characterization of the Ruthenium Complex Indicator

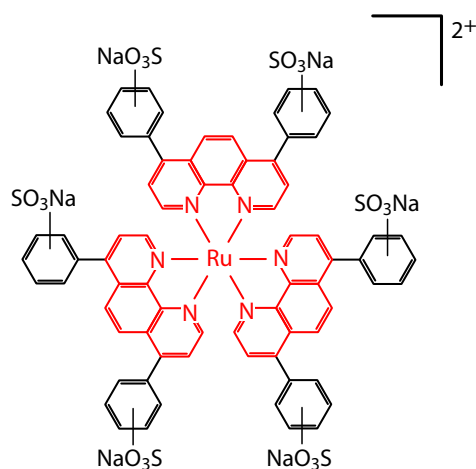


**Figure 5.1.:** Schematic drawing of the water soluble MLC  $[\text{Ru}(\text{dpp}(\text{SO}_3\text{Na})_2)_3]\text{Cl}_2$  used in this study. The metal Ruthenium (Ru) is indicated in the centre. The ligand 4,7-diphenyl-1,10-phenanthroline (dpp) is shown in red around the centre. Water solubility is reached due to the  $\text{SO}_3\text{Na}$  groups. Modified from Lakowicz [2006].

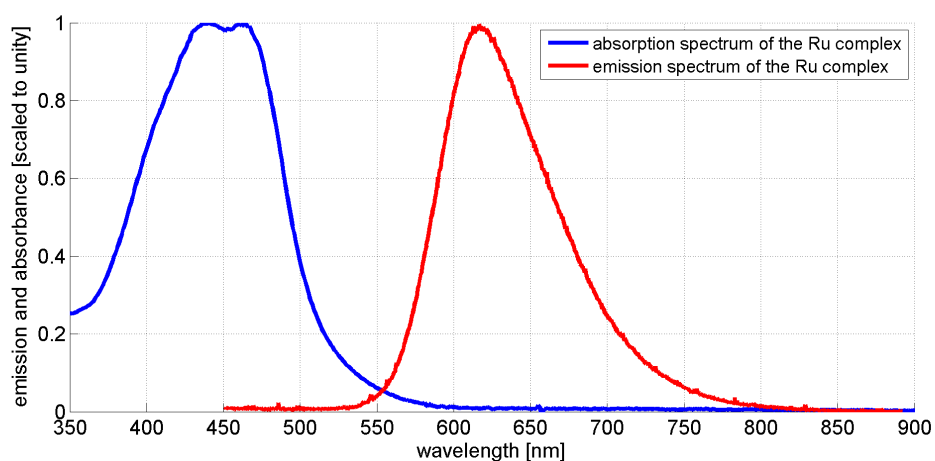


**Figure 5.2.:** Emission and absorption spectra of the Ru complex. For the emission spectrum, the Ru complex was excited by the laser described in Section 4.2.2 with a wavelength of 445 nm.

a wavelength of 445 nm (see Section 4.2.2), so that the emission light could be observed at a 90 degree angle with respect to the incident laser light. The maximum emission wavelength is at about 616 nm, the maximum of the absorbance ranges from 440 nm to 465 nm. The Stokes shift between the wavelength of the laser and the maximum emission wavelength is about 171 nm. This large Stokes shift allows for a spectral separation of the laser light and the emission light of the Ru complex and ensures that the self-absorption of the Ru complex can be neglected. The synthesis of the water soluble Ru complex ( $[\text{Ru}(\text{dpp}(\text{SO}_3\text{Na})_2)_3]\text{Cl}_2$ ) was performed by a student assistant as described in Appendix A.1.

## 5.2. Quenching Characteristics

In this section the general Stern-Volmer equation (2.86), derived in Section 2.3.4, is experimentally verified, and the Stern-Volmer constant  $K_{\text{SV}}$  of the Ru complex is determined for different temperatures.

For convenience, a new term, the effective Stern-Volmer constant  $K_{\text{eff}}$ , is introduced here:

$$K_{\text{eff}} := K_{\text{SV}} \cdot \epsilon_{\text{D}}. \quad (5.1)$$

Using the damping factor  $\epsilon_{\text{D}}$  (see equation (2.87)) the general Stern-Volmer equation (2.86) is rewritten:

$$\frac{\Phi_0}{\Phi} = 1 + K_{\text{SV}} \cdot \epsilon_{\text{D}} \cdot c \quad (5.2)$$

To show that equation (5.2) is correct, the photon flux  $\Phi$  is measured with respect to the  $\text{O}_2$  concentration  $c$  for different damping factors  $\epsilon_{\text{D}}$ . The damping factor  $\epsilon_{\text{D}}$  is varied by using different laser power values. With this set of data, equation (5.2) is tested in Section 5.2.2. The photon flux  $\Phi$  is measured with a camera. The method is described in Section 3.2.1.

The photon flux without quencher  $\Phi_0$  and the effective Stern-Volmer constant  $K_{\text{eff}}$  are determined by fitting equation (5.2) to the measured data presented in Section 5.2.2. The damping factor  $\epsilon_{\text{D}}$  is determined independently in Section 5.2.1. The Stern-Volmer constant  $K_{\text{SV}}$  is calculated for each damping factor, using the definition (5.1). It is shown that the measured values of  $K_{\text{SV}}$  are independent of the damping factor, as expected (see equation (2.85)).

The measurements presented in this section were performed in a linear visualization-test wind-wave tank described in Section 4.1.2. The small air and water volumes of this tank allow a fast change of the  $\text{O}_2$  concentration in water and in air.

### 5.2.1. Measurement of the Damping Factor $\epsilon_{\text{D}}$

In this section, the damping factor  $\epsilon_{\text{D}}$  (3.11)

$$\epsilon_{\text{D}} = \frac{P_{\text{sat}}}{P + P_{\text{sat}}} \quad (5.3)$$

is determined as a function of the laser power  $P$  and the saturation laser power  $P_{\text{sat}}$  at the oxygen concentration  $c$  of zero. In Section 3.2.2, a method to determine the damping factor  $\epsilon_{\text{D}}$  was described. To calculate the damping factor  $\epsilon_{\text{D}}$  with equation (5.3), the saturation laser power  $P_{\text{sat}}$  at the  $\text{O}_2$  concentration  $c$  of zero has to be determined. As this is hard to realize, the photon flux  $P_{\text{sat}}^q$  is measured at different  $\text{O}_2$  concentrations. The photon flux  $P_{\text{sat}}$  at the  $\text{O}_2$  concentration of zero is obtained by an extrapolation of the data. As a result, we obtain the damping factor  $\epsilon_{\text{D}}$  as a function of the laser power  $P$ . Knowing the damping factor for different values of  $P$  was essential to confirm the generalized Stern-Volmer equation (2.86) and to make an optimal choice for the laser power  $P$  for the systematic  $\text{O}_2$  profile measurements.

## 5. Characterization of the Ruthenium Complex Indicator

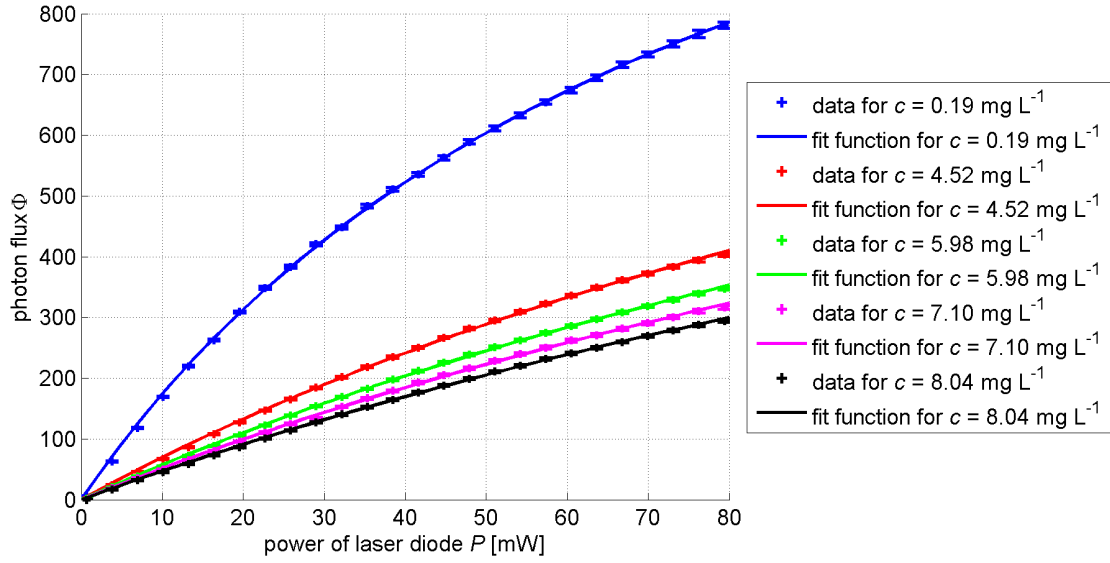


**Figure 5.3.:** Photon flux  $\Phi$  with respect to the laser power  $P$  for five different  $O_2$  concentrations from  $c = 0.19 \text{ mg L}^{-1}$  to  $c = 8.04 \text{ mg L}^{-1}$ . Equation (3.10) is fitted to each data sets and yields the fit parameters maximum photon flux  $\Phi_{\text{max}}$  and saturation laser power  $P_{\text{sat}}^q$ . The values of  $P_{\text{sat}}^q$  are needed to calculate the saturation laser power  $P_{\text{sat}}$  and are listed here:  $P_{\text{sat}}^q = [81.4; 185.2; 218.9; 239.6; 260.0] \text{ mW}$ .

In the first step of the measurement of the damping factor  $\epsilon_D$ , the saturation laser power with quencher  $P_{\text{sat}}^q$  is measured for five different  $O_2$  concentrations. Figure 5.3 shows the photon flux  $\Phi$  with respect to the laser power  $P$  for five different  $O_2$  concentrations from  $c = 0.19 \text{ mg L}^{-1}$  to  $c = 8.04 \text{ mg L}^{-1}$ . The saturation irradiance  $P_{\text{sat}}^q$  is obtained by fitting equation (3.10)

$$\Phi = \Phi_{\text{max}} \cdot \frac{P}{P_{\text{sat}}^q + P} \quad (5.4)$$

to the data. Figure 5.3 shows that the photon flux  $\Phi$  is non-linear with respect to the laser power  $P$ . This means that the approximation of a weak excitation (see equation (2.77)) is not valid for a laser power of 80 mW. The fit functions to the data at the five different  $O_2$  concentrations yield five values of the saturation laser power with quencher  $P_{\text{sat}}^q$ , listed in the caption of Figure 5.3. The bimolecular quenching constant  $k_q$  and consequently also  $P_{\text{sat}}^q$  depend on the temperature (see equation (3.9)). Here, all calibration measurements were performed at  $20^\circ\text{C}$ , which is the same temperature as used for the measurements in the following section 5.2.2, where the Stern-Volmer constant  $K_{\text{SV}}$  is measured. The laser saturation power  $P_{\text{sat}}$  for of  $c = 0 \text{ mg L}^{-1}$  is obtained by fitting equation (3.9)

$$P_{\text{sat}}^q = P_{\text{sat}} + \alpha_P \cdot \frac{k_q}{\sigma_a} \cdot c \quad (5.5)$$

to the determined values of  $P_{\text{sat}}^q$ , see Figure 5.4. The offset of the linear fit function yields the saturation laser power  $P_{\text{sat}} = (77 \pm 1) \text{ mW}$  for  $c = 0 \text{ mg L}^{-1}$ . The damping factor  $\epsilon_D$  can then be calculated using equation (5.3). For the determination of the Stern-Volmer constant  $K_{\text{SV}}$  in

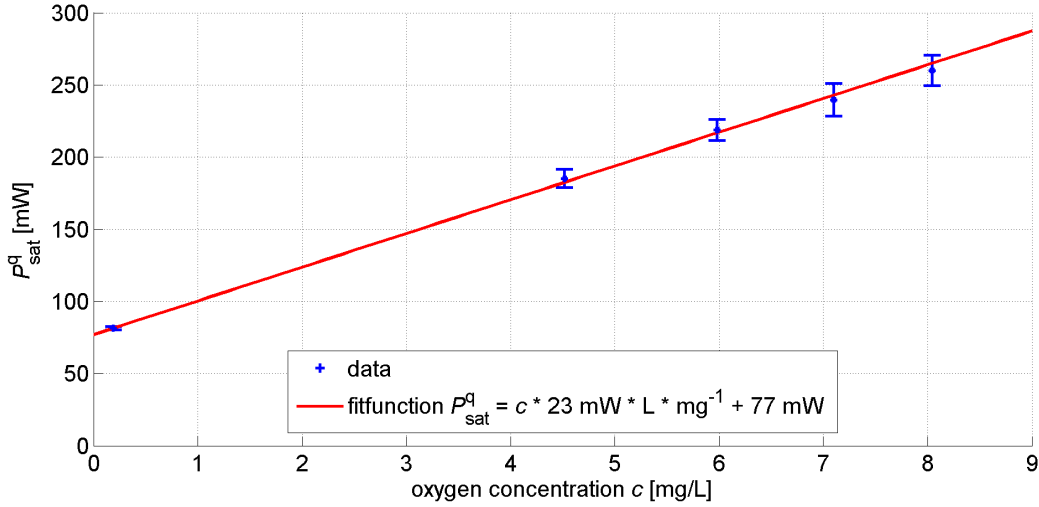


**Figure 5.4.:** Laser saturation power with quencher  $P_{\text{sat}}^q$  with respect to the  $\text{O}_2$  concentration  $c$ . The five data points are obtained from the fit functions, shown in Figure 5.3, at the given  $\text{O}_2$  concentrations. The linear correlation between  $P_{\text{sat}}^q$  and  $c$  is shown in equation (3.9). From the offset of the linear fit to the data, the saturation laser power  $P_{\text{sat}} = (77 \pm 1) \text{ mW}$  at an  $\text{O}_2$  concentration of  $c = 0 \text{ mg L}^{-1}$  is obtained.

**Table 5.1.:** Laser power modes and the corresponding damping factors  $\epsilon_D$  that are used for the measurement of the Stern-Volmer constant  $K_{\text{SV}}$  in Section 5.2.2.

laser control voltage [V]	laser power $P$ [mW]	damping factor $\epsilon_D$
0.6	$10.091 \pm 0.004$	$0.884 \pm 0.002$
2.6	$41.590 \pm 0.005$	$0.649 \pm 0.005$
5.0	$79.389 \pm 0.007$	$0.492 \pm 0.004$

Section 5.2.2, three different values of the laser power were used. The corresponding values of the damping factor  $\epsilon_D$  are given in Table 5.1.

**Comparison of the Measured Laser Saturation Power with a Theoretical Value** A comparison of the experimentally determined value of the laser saturation power  $P_{\text{sat}}$  and a theoretical value is shown in the following. The purpose is to check if the literature values for the lifetime  $\tau_0$  and the cross section  $\sigma_a$  of the Ru complex agree with the measured laser saturation power  $P_{\text{sat}}$ . To calculate the theoretical value of the laser saturation irradiance, equation (2.75)

$$E_{\text{sat}} = \frac{1}{\tau_0 \cdot \sigma_a} \quad (5.6)$$

is used. Two values of the lifetime  $\tau_0$  of the Ru complex were found, one in the literature ( $3.7 \mu\text{s}$  in [Castellano and Lakowicz, 1998]), and one unpublished from previous lab studies ( $3.9 \mu\text{s}$  [Jähne, 2012, personal communication]). For both values, no error estimates are given. So we use the mean value of  $\tau_0 = 3.8 \mu\text{s}$  with an error of  $0.1 \mu\text{s}$  in the following. A value of  $\epsilon = (35000 \pm 1000) \frac{\text{L}}{\text{mol}} \frac{1}{\text{cm}}$  is used for the extinction coefficient, also unpublished and obtained from previous lab studies [Jähne, 2012, personal communication]. The cross section  $\sigma_a$  can be calculated from

## 5. Characterization of the Ruthenium Complex Indicator

the extinction coefficient  $\epsilon$  using Lambert-Beer's law:

$$E = E_0 \cdot 10^{-\epsilon \cdot c \cdot z} = E_0 \cdot \exp(-\sigma_a \cdot \rho \cdot z), \quad (5.7)$$

with the irradiance  $E_0$  at the entry of the medium, the concentration of the absorbing species  $c$ , the path length  $z$  in the absorbing medium, and the density of the absorbing species  $\rho$ . The cross section follows from equation (5.7) and :

$$\sigma_a = \epsilon \cdot \ln 10 \cdot N_A^{-1} \text{ mol} \quad (5.8)$$

With the extinction coefficient  $\epsilon$  given above, the cross section is  $\sigma_a = (1.34 \pm 0.04) \cdot 10^{-16} \text{ cm}^2$ . Using equation (5.6), the corresponding laser saturation irradiance is

$$E_{\text{sat}}^{\text{theo}} = (1.96 \pm 0.08) \cdot 10^{21} \text{ s}^{-1} \text{ cm}^{-2}.$$

Now, the experimentally determined value of the laser saturation power of  $P_{\text{sat}} = (77 \pm 1) \text{ mW}$  is converted into a laser saturation irradiance  $E_{\text{sat}}^{\text{exp}}$ , that can be compared with  $E_{\text{sat}}^{\text{theo}}$ . The absorption of the laser light in the water volume due to absorption by the Ru complex has to be taken into account, as the laser power used so far is the power at the exit of the laser diode. The light path of the laser beam to the measuring section in the water body was about  $z = 6 \text{ cm}$ . The product of the extinction coefficient and the concentration was measured with a spectrometer<sup>3</sup> to be  $\epsilon \cdot c = (6.80 \pm 0.01) \cdot 10^{-2} \text{ cm}^{-1}$ . The remaining laser power after 6 cm absorption path is then

$$P_{\text{sat}}^{6 \text{ cm}} = P_{\text{sat}} \cdot 10^{-0.068 \cdot 6} = (30.1 \pm 0.4) \text{ mW}.$$

The photon flux  $\Phi_{\text{photon}}$  in the measuring section is obtained from the laser power  $P_{\text{sat}}^{6 \text{ cm}}$  by

$$\Phi_{\text{photon}} = \frac{P_{\text{sat}}^{6 \text{ cm}}}{h \cdot \frac{c}{\lambda}} = (6.79 \pm 0.09) \cdot 10^{16} \text{ s}^{-1}, \quad (5.9)$$

where  $h$  is the Planck constant,  $c$  the speed of light, and  $\lambda = 445 \text{ nm}$  the wavelength of the laser. To convert the photon flux  $\Phi_{\text{photon}}$  into a photon irradiance  $E_{\text{sat}}^{\text{exp}}$ , the area over which the laser is distributed needs to be known. The laser cross section was measured for this purpose (see Section 4.2.2). The distribution of the photon flux can be approximated with a two-dimensional Gaussian beam with the standard deviation in x- and y-direction of  $\sigma_x = 20 \mu\text{m}$  and  $\sigma_y = 12 \mu\text{m}$ . As the photon flux is not evenly distributed, only an approximation of the average photon irradiance  $E_{\text{sat}}^{\text{exp-av}}$  is given here. The area  $A$ , over which the photon flux is distributed, can be approximated as the two-dimensional  $\pm 2\sigma$  region ( $A \approx 80 \mu\text{m} \cdot 48 \mu\text{m}$ ). For the average

---

<sup>3</sup>spectrometer: HP 8453 E UV-visible

photon irradiance  $E_{\text{sat}}^{\text{exp-av}}$  follows

$$E_{\text{sat}}^{\text{exp-av}} = \frac{\Phi_{\text{photon}}}{A} \approx 1.8 \cdot 10^{21} \text{ s}^{-1} \text{ cm}^{-2}.$$

The experimentally determined saturation irradiance  $E_{\text{sat}}^{\text{exp-av}}$  is about a factor of 0.9 lower than the theoretical saturation irradiance  $E_{\text{sat}}^{\text{theo}}$ . The deviation is not surprising, as a simplistic approximation of the average laser irradiance was used. However, we see that laser saturation irradiance is compatible with the known cross section  $\sigma_a$  and the lifetime  $\tau_0$  of the Ru complex.

### 5.2.2. Measurement of the Stern-Volmer Constant

A precise determination of the Stern-Volmer constant  $K_{\text{SV}}$  is crucial for precise  $\text{O}_2$  concentration measurements by the LIF method. In the literature, only one value for  $K_{\text{SV}}$  could be found [Castellano and Lakowicz, 1998], but the reduction of the effective Stern-Volmer constant  $K_{\text{eff}}$  due to high laser irradiance was not investigated by these authors. Here, the Stern-Volmer constant  $K_{\text{SV}}$  is determined for three laser power values considering the damping factors  $\epsilon_{\text{D}}$  listed in Table 5.1. The resulting values of the Stern-Volmer constants  $K_{\text{SV}}$  are independent of the laser power. With these measurements the generalized Stern-Volmer equation (2.86) was confirmed.

In order to measure the Stern-Volmer constant  $K_{\text{SV}}$ , the photon flux  $\Phi$  with respect to the  $\text{O}_2$  concentration was measured, see Figure 5.5. The generalized Stern-Volmer equation (5.2)

$$\frac{\Phi_0}{\Phi} = 1 + K_{\text{SV}} \cdot \epsilon_{\text{D}} \cdot c$$

is fitted to the data to obtain  $K_{\text{SV}}$ . The parameters determined by the fit are the photon flux  $\Phi_0$  and the effective Stern-Volmer constant  $K_{\text{eff}} = K_{\text{SV}} \cdot \epsilon_{\text{D}}$ . Figure 5.5 shows the Stern-Volmer plot for the three laser power values. The results of the effective Stern-Volmer constants  $K_{\text{eff}}$  are listed in Table 5.2. As predicted with the generalized Stern-Volmer equation (2.86), the effective Stern-Volmer constant  $K_{\text{eff}}$  depends on the laser irradiance  $E$  and accordingly the laser power  $P$ . The higher the laser power, the lower is the value of the effective Stern-Volmer constant  $K_{\text{eff}}$ , and so is the slope of the fitted lines in Figure (5.5). This is an indication that the correction term  $\epsilon_{\text{D}}$ , introduced in this thesis, has to be added to the known Stern-Volmer equation (2.89). The data of the Stern-Volmer measurements is also presented in a different form in the Appendix A.3 for direct comparison with former measurements by Falkenroth [2007] and Münsterer [1996].

**Table 5.2.:** Laser power modes, the determined effective Stern-Volmer constants  $K_{\text{eff}}$ , and Stern-Volmer constants  $K_{\text{SV}}$ .

laser power $P$ [mW]	$K_{\text{eff}}$ [L mg <sup>-1</sup> ]	$K_{\text{SV}}$ [L mg <sup>-1</sup> ]
10.091 ± 0.004	0.3883 ± 0.0019	0.439 ± 0.003
41.590 ± 0.005	0.2837 ± 0.0009	0.437 ± 0.005
79.389 ± 0.007	0.2556 ± 0.0008	0.458 ± 0.008

## 5. Characterization of the Ruthenium Complex Indicator

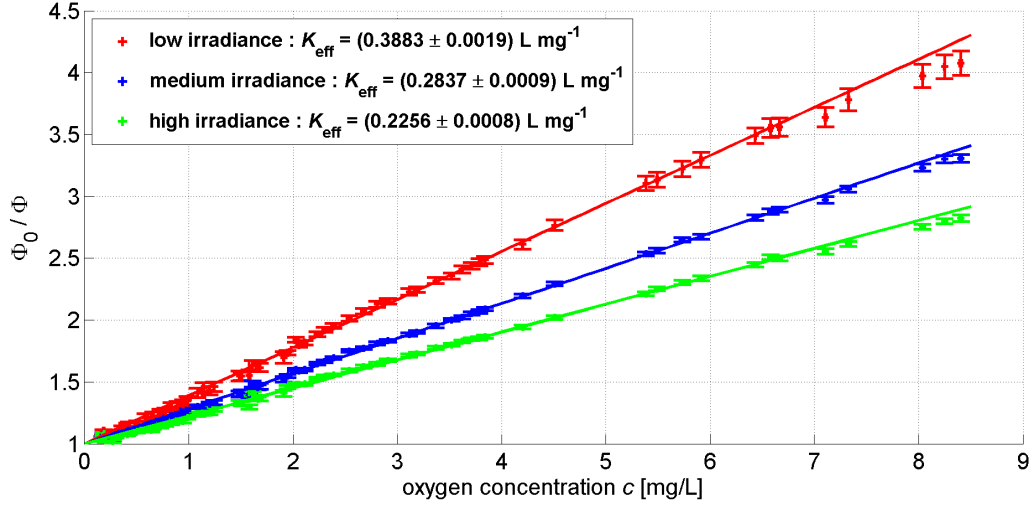


**Figure 5.5.:** Stern-Volmer plot for three different laser irradiance values. The photon flux  $\Phi_0$  in absence of  $\text{O}_2$  divided by the photon flux  $\Phi$  is plotted with respect to the  $\text{O}_2$  concentration in the water phase. The temperature was  $20^\circ\text{C}$ . Equation (5.2) is fitted to the three data sets. The fitting procedure yields three values for the effective Stern-Volmer constant  $K_{\text{eff}}$ , as indicated in Table 5.2.

The data for the Stern-Volmer plot, Figure 5.5, was measured by realizing multiple concentrations of  $\text{O}_2$  between  $0.17\text{ mg L}^{-1}$  and  $8.4\text{ mg L}^{-1}$  (equilibrium concentration with air) in the water as described in Section 3.2.1. To obtain the data, the photon flux  $\Phi$  was measured at three laser power values (see Table 5.2) and the  $\text{O}_2$  concentration was documented. The whole Stern-Volmer measurement took seven days. During the measurement, the temperature was kept constant at  $20^\circ\text{C}$  in the wind-wave tank. This temperature was chosen for comparison because the measured Stern-Volmer constant  $K_{\text{SV}}$  of Castellano and Lakowicz [1998] of the Ru complex was also measured at this temperature. The temperature regulation produced oscillations of  $\pm 0.1^\circ\text{C}$ . To minimize temperature effects during the measurement, data was only taken when the temperature was within  $(20 \pm 0.03)^\circ\text{C}$ .

To calculate the Stern-Volmer constant  $K_{\text{SV}}$  for the Ru complex, the obtained effective Stern-Volmer constants  $K_{\text{eff}}$  in Table 5.2 have to be divided by the corresponding damping factors  $\epsilon_{\text{D}}$  according to equation (5.1). By representing the Stern-Volmer measurement in the form of the rewritten equation (5.2)

$$\left(\frac{\Phi_0}{\Phi} - 1\right) \cdot \epsilon_{\text{D}}^{-1} = K_{\text{SV}} \cdot c, \quad (5.10)$$

the similarity of the three results for the Stern-Volmer constants  $K_{\text{SV}}$  is visualized in Figure 5.6. To scale the data, the independently measured damping factors  $\epsilon_{\text{D}}$  from Table 5.1 were used. The results for the Stern-Volmer constants  $K_{\text{SV}}$  are listed in Table 5.2. The values of the Stern-Volmer constants  $K_{\text{SV}}$  all agree within the  $\pm 2\sigma$  region. This shows that equation (2.89) describes the dependence of the quenching mechanism with the laser irradiance  $E$  in the right way. The small deviations of the three Stern-Volmer constants  $K_{\text{SV}}$  can be explained with the uncertainties of the damping factors  $\epsilon_{\text{D}}$ .

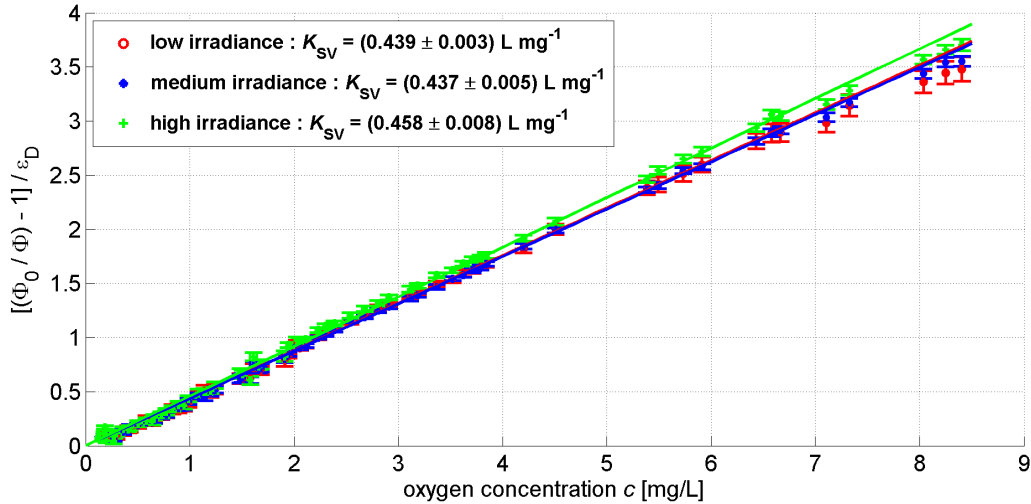


**Figure 5.6.:** Scaled Stern-Volmer plot according to equation (5.10). The data from the Stern-Volmer measurement is scaled with the damping factors  $\epsilon_D$  (see Table 5.1).

The damping factor  $\epsilon_D$

$$\epsilon_D = \frac{n_0}{N},$$

(equation (A.5)) specifies the fraction of the Ru complex molecules in the ground state. The higher the laser irradiance  $E$ , the less molecules of the Ru complex are in the ground state. This explains that the damping factor  $\epsilon_D$  decreases with increasing laser irradiance  $E$ . The Stern-Volmer constant  $K_{SV}$  does not depend on the laser irradiance  $E$  according to the definition in equation (2.85):  $K_{SV} = k_q \cdot \tau_0$ . The bimolecular quenching constant  $k_q$  is determined by the collision probability between the molecules of the fluorophore and the quencher, but independent of the laser irradiance  $E$ .

The result for the Stern-Volmer constant of the Ru complex at a temperature of 20 °C is obtained by calculating the weighted mean  $K_{SV}$  of the values from Table 5.2:

$$K_{SV} = (0.444 \pm 0.007) \text{ L mg}^{-1}$$

The value of the Stern-Volmer constant documented in the paper of Castellano and Lakowicz [1998] is  $K_{SV} = 0.354 \text{ L mg}^{-1}$ . The difference can possibly be explained with the fact that they measured at a high laser irradiance and the  $\epsilon_D$  value was consequently smaller than unity. The value of  $K_{SV}$  that Castellano and Lakowicz [1998] reported was supposedly the effective Stern-Volmer constant  $K_{\text{eff}}$ .

The Stern-Volmer constant  $K_{SV}$  of the Ru complex is about 22 times higher than the Stern-Volmer constant of pyrenebutyric acid (PBA), which is commonly used for LIF experiments [Walker and Peirson, 2008; Wolff and Hanratty, 1994].

To conclude, the generalized Stern-Volmer equation (2.86) describes the quenching effect at different laser irradiance values sufficiently well. We have seen that introducing the damping

## 5. Characterization of the Ruthenium Complex Indicator

factor  $\epsilon_D$  in equation (2.86) helps to correctly model the experimental data. For the determination of the Stern-Volmer constant  $K_{SV}$  of a fluorophore, the damping factor  $\epsilon_D$  has to be known. Otherwise, only the effective Stern-Volmer constant  $K_{\text{eff}}$  can be measured.

### 5.2.3. Measurement of the Temperature Dependence of the Stern-Volmer Constant

The temperature dependence of the Stern-Volmer constant  $K_{SV}$  of the Ru complex must be known for two reasons. The Stern-Volmer constant  $K_{SV}$  still has to be known if the experiments are performed at a water temperature differing from 20 °C. Secondly, the precision of the measurement depends on the variation of  $K_{SV}$  with temperature. There are temperature fluctuations in the tank induced by pumps and the wind turbine. A deviation in the measuring section from the mean water temperature leads to an error in the determination of the O<sub>2</sub> concentration  $c$ .

To measure the temperature dependence of the Stern-Volmer constant  $K_{SV}$ , the same measurement setup as in the previous two sections was used. During the measurement, the laser was pulsed to minimize the warming of the measuring volume due to laser heating. The laser was triggered to give a pulse of 0.3 ms for each camera exposure. With the camera frame rate of 10 Hz the resulting duty cycle is 0.3%. The pump of the bypass with a discharge flow of 14 L min<sup>-1</sup> was switched on during the measurement. The resulting flow of the water leads to a transport of the heat pulses in flow direction. When the laser is switched on, the heat pulse of the preceding laser pulse is already transported out of the measuring volume due to the low laser pulse rate.

The O<sub>2</sub> concentration was kept constant at  $c = 7.57 \text{ mg L}^{-1}$  and the water temperature  $T$  was varied between 17 °C and 27 °C in steps of 0.5 °C by a peltier temperature controller installed in the linear visualization-test wind-wave tunnel, see Section 4.1.2. The result of the measurement is shown in Figure 5.7, where the photon flux  $\Phi$  is plotted with respect to the temperature of the water. The measurement was performed at a high laser irradiance corresponding to a damping factor of  $\epsilon_D = 0.492$ . A linear decrease of the photon flux  $\Phi$  with rising temperature can be observed in the figure. This effect is explained with a rise of the bimolecular quenching constant  $k_q$  with increasing temperature due to a higher collision probability between the molecules of the quencher and the Ru complex.

To calculate the temperature dependence of the Stern-Volmer constant  $K_{SV}$  from the data in Figure 5.7, we start with

$$K_{SV}(T) = \left( \frac{\Phi_0}{\Phi(T)} - 1 \right) \cdot \frac{1}{\epsilon_D \cdot c}, \quad (5.11)$$

see equation (5.2). We assume that  $\Phi_0$ , the photon flux in absence of oxygen, and the damping factor  $\epsilon_D$  do not depend on the temperature  $T$ . This was tested with two measurements. To

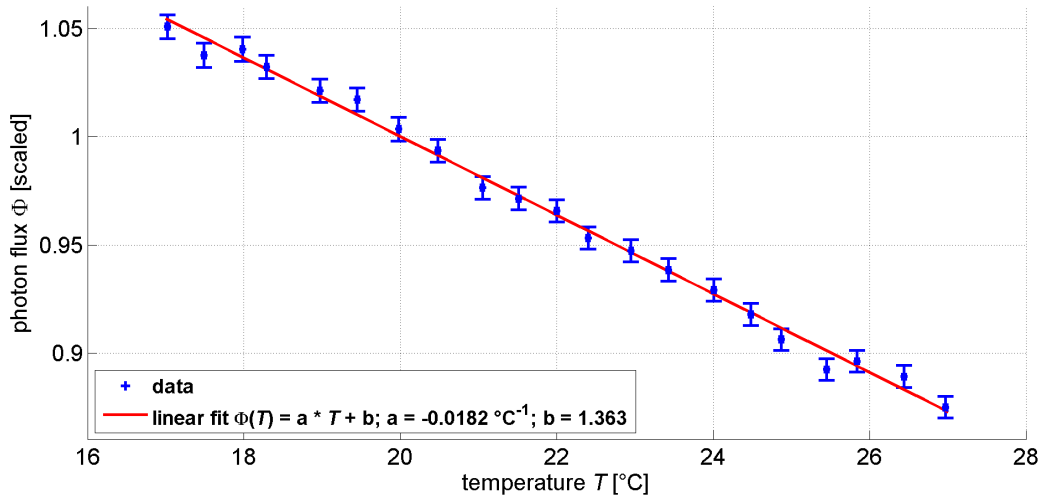


**Figure 5.7.:** Temperature dependence of the photon flux  $\Phi$ , scaled to unity at a temperature of 20 °C. The data was taken at a high laser irradiance, corresponding to a damping factor of  $\epsilon_D = 0.492$ , and at an  $O_2$  concentration of the water space of  $c = 7.57 \text{ mg L}^{-1}$ . The photon flux  $\Phi$  decreases linearly with temperature in the measured temperature range at about 1.8 % per Kelvin at a temperature of 20 °C, as the linear fit function shows.

check if the damping factor

$$\epsilon_D = \frac{E_{\text{sat}}}{E(\text{abs}) + E_{\text{sat}}}$$

shows a temperature dependence, the absorbance *abs* of the Ru complex in water was measured with a spectrometer<sup>4</sup> for temperatures in the range between 25 °C and 38 °C. The absorbance showed no significant change with temperature leading to the assumption of a temperature independent damping factor  $\epsilon_D$ . To test if the photon flux  $\Phi_0$  varies with temperature, the same measurement as the one shown in Figure 5.7 was performed at  $c = 0.17 \text{ mg L}^{-1}$ . The change of the photon flux  $\Phi$  with respect to the temperature  $T$  is in agreement with the measured change of the Stern-Volmer constant  $K_{\text{SV}}$  presented at the end of this section. This justifies the assumption of negligible temperature changes of  $\Phi_0$  and  $\epsilon_D$ .

The photon flux  $\Phi_0$  in absence of  $O_2$  is obtained from equation (5.11)

$$\Phi_0 = \Phi(20^\circ\text{C}, c) \cdot (1 + K_{\text{SV}}(20^\circ\text{C}) \cdot \epsilon_D \cdot c), \quad (5.12)$$

where  $c$  is the  $O_2$  concentration which was measured when  $\Phi$  was recorded. The concentration  $c$  was measured using an oxygen probe, described in Section 4.1.1.

The temperature dependence was measured at three different laser irradiance values to test if the result for the temperature dependence is the same for different damping factors  $\epsilon_D$ . Moreover, combining the measurements obtained for different laser irradiance values yields a more robust estimate of the temperature dependence of the Stern Volmer constant  $K_{\text{SV}}$ . The measured temperature variation of the calculated Stern-Volmer constant  $K_{\text{SV}}$  is shown in Figure 5.8. The

<sup>4</sup>spectrometer: HP 8453 E UV-visible

## 5. Characterization of the Ruthenium Complex Indicator

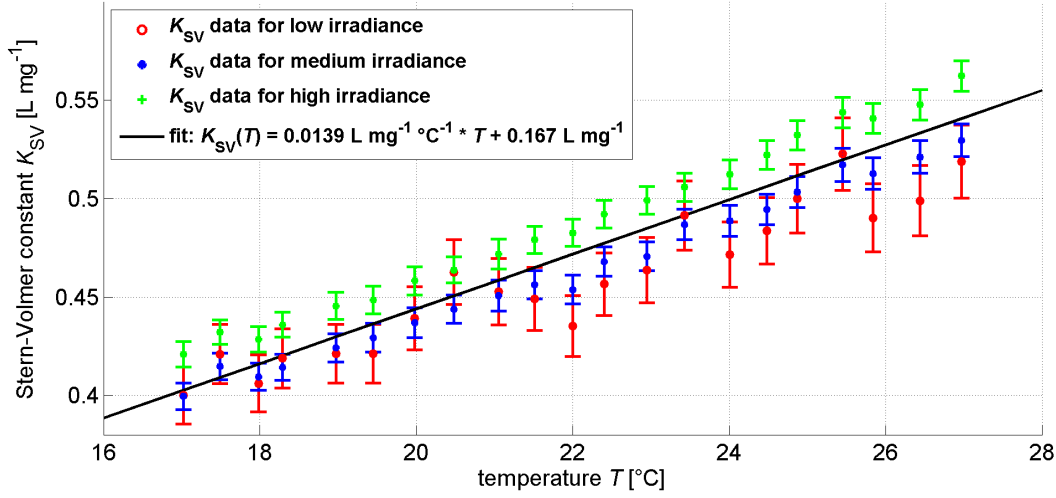


**Figure 5.8.:** Temperature dependence of the Stern-Volmer constant  $K_{SV}$  measured for the three different laser power values listed in Table 5.1.

values were calculated using equations (5.11) and (5.12). A linear fit was performed with the prior knowledge that the Stern-Volmer constant  $K_{SV}$  at 20 °C reaches the value of 0.444 mg L<sup>-1</sup> presented in Section 5.2.2. This restriction can be made because the result of  $K_{SV}$  in the last section (5.2.2) was obtained with a higher precision than here. This is due to better statistics of the measurement in the last section (see the amount of data points in Figure 5.5) and the higher precision of each single value in Table 5.2 compared to values in Figure 5.8.

The values of the Stern-Volmer constant  $K_{SV}$  measured at a high laser irradiance are systematically higher than the values measured at a lower laser irradiance. The errors of the  $K_{SV}$  values for low irradiance are greater compared to the two other data sets because the SNR (signal-to-noise ratio) of the photon flux  $\Phi$  is bigger due to the lower signal. The data points agree well within the  $\pm 2\sigma$  region, most within the  $\pm \sigma$  region. This good agreement again confirms (as Figure 5.6) that the damping factors  $\epsilon_D$  (see Table 5.1) for the three laser irradiance values were well determined and that equation (2.86) correctly models the physics.

To conclude, the temperature dependence of the Stern-Volmer constant  $K_{SV}(T)$  can be expressed as

$$K_{SV}(T) = (1.39 \pm 0.03) \cdot 10^{-2} \text{ L mg}^{-1} \text{ } ^\circ\text{C}^{-1} \cdot T + (0.167 \pm 0.006) \text{ L mg}^{-1}, \quad (5.13)$$

where  $T$  is the water temperature in °C in the range between 17 °C and 27 °C. The temperature of the water during the gas exchange experiments varied between 20 °C and 23.5 °C due to seasonal changes of the room temperature. Hence, the measured temperature range between 17 °C and 27 °C fully covers the range of the water temperatures during the experiments. The

temperature dependence corresponds to a relative change per Kelvin of

$$\frac{\frac{\partial K_{SV}}{\partial T}}{K_{SV}(20^\circ\text{C})} = 3.1 \frac{\%}{\text{K}}. \quad (5.14)$$

From the generalized Stern-Volmer equation (5.2)

$$c = \left( \frac{\Phi_0}{\Phi} - 1 \right) \cdot \frac{1}{K_{SV} \cdot \epsilon_D}, \quad (5.15)$$

it follows that the relative error for the measured O<sub>2</sub> concentration due to a change of the temperature is

$$\frac{\frac{\partial c}{\partial T}}{c} = -3.1 \frac{\%}{\text{K}}. \quad (5.16)$$

at a temperature of 20°C. Assuming the average temperature of the water is 19°C, but a local fluctuation in the measuring region leads to a warming-up of 1 K. Hence, the Stern-Volmer constant  $K_{SV}$  for 19°C is used, which is 3.1% too low, according to equation (5.14). The calculated O<sub>2</sub> concentration will be overestimated about 3.1%. Errors in the determination of the O<sub>2</sub> concentration due to temperature fluctuations of the water are regarded in Section 3.1.3, where all effects that influence the precision of the measuring method are considered.

### 5.3. Photobleaching Test

The photon flux  $\Phi$  emitted by a fluorophore can be reduced by photobleaching [Crimaldi, 1997]. That means that some molecules of the fluorophore lose their ability to fluoresce after being subjected to laser illumination. Strong excitation light leads to either permanent or temporarily bleaching of the fluorophore molecules.

The effect of permanent photobleaching was tested for the Ru complex with a measurement over 13 hours. The Ru complex was solved in deionized water (VE-water<sup>5</sup>) in a small cubic cuvette (125 cm<sup>3</sup>) and excited with a focussed laser (Section 4.2.2) at the highest power available in the continuous wave mode. The photon flux  $\Phi$  and the temperature in the cuvette are shown in Figure 5.9. In the first 20 minutes of the 13 hour measurement, the photon flux  $\Phi$  decreased about 2%. For the rest of the measurement, the signal loss was on the order of the noise level of about 0.5%. In the case of permanent photobleaching, the photon flux  $\Phi$  should have been decaying exponentially over time (see [Crimaldi, 1997]) to a value of zero. As an exponential decay could not be observed for the measurement even after 13 hours, there is no significant permanent photobleaching. This finding is consistent with the statement in the book of Lakowicz [2006], that the class of metal-ligand complexes (to which the Ru complex belongs to) displays a high chemical and photochemical stability.

The decay within the first 20 minutes of the measurement can be explained by the rise of the

---

<sup>5</sup>VE-water: from the German expression “vollentsalztes Wasser”

## 5. Characterization of the Ruthenium Complex Indicator

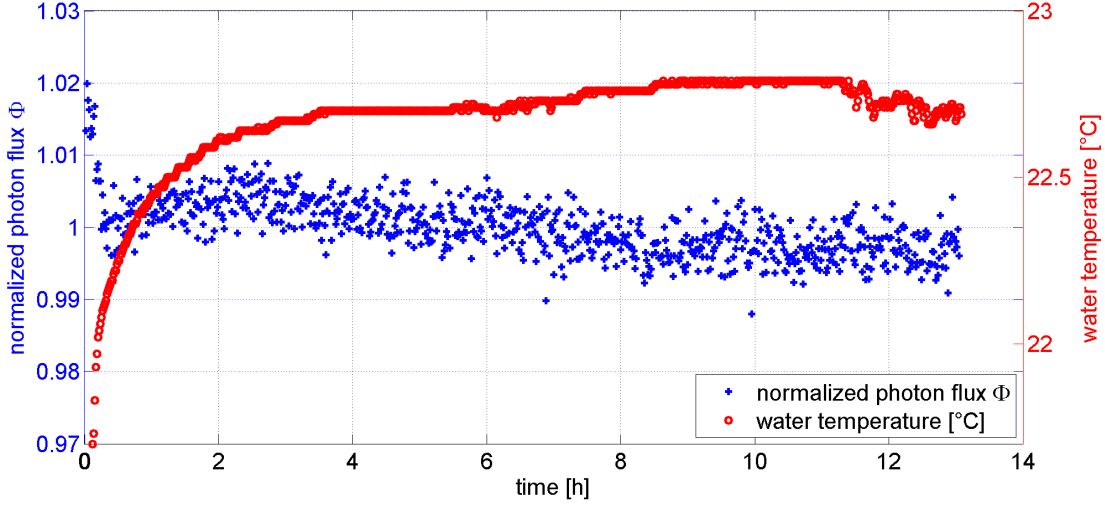


**Figure 5.9.:** Time series of the measured photon flux  $\Phi$  emitted by the Ru complex and excited with a laser. The cuvette was open to the air so that the  $O_2$  concentration of the water was in equilibrium with the  $O_2$  concentration in the air at standard conditions.

water temperature within the small volume that is directly illuminated by the laser. An increase of the temperature in the measuring section leads to a higher Stern-Volmer constant  $K_{SV}$  (see Section 5.2.3) and thus to a lower photon flux  $\Phi$ . The measured change in the normalized photon flux  $\Phi$  is consistent with the change of the water temperature which was measured in the corner of the cuvette. The relative change of the photon flux  $\Phi$  within the first 20 minutes is about

$$\frac{d\Phi}{\Phi} \approx -0.02.$$

From the generalized Stern-Volmer equation (5.2), we obtain the following equation for a change of the Stern-Volmer constant  $dK_{SV}$

$$dK_{SV} = \left( \frac{1}{c \cdot \epsilon_D} + K_{SV} \right) \cdot \frac{d\Phi}{\Phi}. \quad (5.17)$$

At the beginning of the measurement, the temperature was around 22 °C, which corresponds to a Stern-Volmer constant of  $K_{SV} = 0.473 \text{ L mg}^{-1}$ . The  $O_2$  concentration was  $c = 8.4 \text{ mg L}^{-1}$  and the damping factor  $\epsilon_D \approx 0.7$ . In conclusion, the change of the Stern-Volmer constant  $K_{SV}$  within the first 20 minutes should be  $dK_{SV} = 0.0129 \text{ L mg}^{-1}$ . According to equation (5.13), this change in the Stern-Volmer constant is caused by a temperature change  $dT$  of

$$dT \approx 0.9 \text{ K}.$$

This expected change of the temperature is on the order of magnitude of the measured temperature change (Figure 5.9). However, the measured temperature change is smaller than the calculated temperature change. The reason might be that the measured equilibrium temper-

ature in a corner of the cuvette is smaller than the temperature at the heat source (the laser region), due to heat dissipation to the air and the sidewalls of the cuvette.

In conclusion, a significant permanent photobleaching effect was not observed. However, the effect of temporarily bleaching as measured by Saylor [1995] was not ruled out with the test presented in this section.



## 6. Calibration

The laser-induced fluorescence (LIF) method (Section 3.1.1) was applied at the Heidelberg linear wind-wave tunnel (Section 4.1.1) for O<sub>2</sub> invasion experiments (Section 7.3.1). The calibration of the LIF setup is shown in this chapter including i) the optical calibration of the camera with lens in Section 6.1, ii) the measurement of the damping factor  $\epsilon_D$  (equation (2.87)) in Section 6.2, and iii) the calibration of the photon flux  $\Phi_0$  in absence of O<sub>2</sub>, emitted by the fluorophore, in Section 6.3.

### 6.1. Calibration of the Optical Setup

For a quantitative evaluation of the LIF images, the magnification of the optical system was measured. The PSF<sup>1</sup> was measured to determine the achievable resolution of the optical system.

#### 6.1.1. Magnification of the Optical System

The reproduction scale was measured with a Ronchi ruling<sup>2</sup> with a stripe density of 100 lines per inch (or 3.937 line pairs per mm). For the calibration, the Ronchi ruling was positioned in the water as the conditions have to be the same as for the measurements. The Ronchi ruling was illuminated from the backside with a red LED. This was achieved by putting the LED into a waterproof glass box. A diffusor plate was mounted in front of the LED to improve the homogeneity of the light distribution. The Ronchi ruling was attached outside the glass box.

Prior to the calibration, the camera and the laser had to be set up in their final positions and the camera lens was focused on the laser line. After that, the Ronchi ruling was put on the exact position of the laser line in the water in the focal plane of the camera. A calibration picture of the Ronchi ruling is shown in Figure 6.1.

The reproduction scale in horizontal direction of the image was calculated by detecting the horizontal positions of the stripes. This was done with the image processing software Heurisko<sup>®</sup>. The pixel size in object coordinates was measured to be

$$(6.151 \pm 0.001) \mu\text{m pixel}^{-1}. \quad (6.1)$$

---

<sup>1</sup>PSF stands for point spread function. The PSF is the image of a point-shaped object. For more details refer to the digital image processing book from Jähne [2005].

<sup>2</sup>A Ronchi ruling is an optical target with alternating bars and intervals of constant width, named after Vasco Ronchi. Figure 6.1 shows an image of a Ronchi ruling.

## 6. Calibration

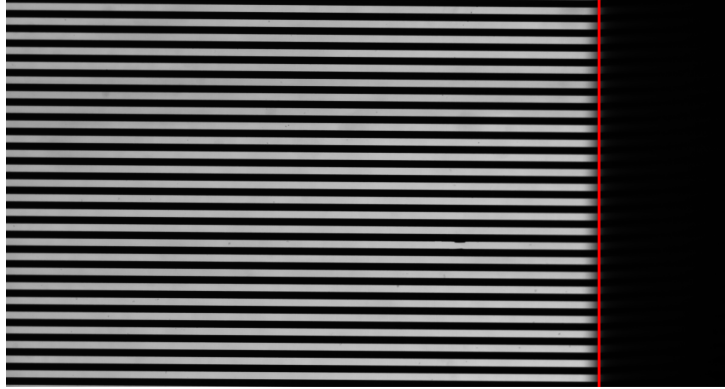


**Figure 6.1.:** Full frame camera picture ( $1088 \times 2048$  pixels) of the Ronchi ruling in the tunnel, filled with water. The camera was tilted 90 degrees to the left. The water surface is depicted with the red line.

With the pixel size of the camera (Section 4.2.4) of  $5.5 \mu\text{m}$ , we obtain a magnification factor  $\beta$

$$\beta = 0.894 \quad (6.2)$$

and a reproduction scale of 1:1.118 of the optical system.

### 6.1.2. Image Sharpness

In this section it is shown, how the width of the point spread function (PSF) of the optical system was measured. This was done under the same conditions as the measurements (same camera position, orientation, magnification, and aperture) at the tunnel filled with water. As described in the previous section, the Ronchi ruling was placed at the position of the laser line. The Ronchi ruling was tilted, so that one image column sees a sharp image of the stripes. Figure 6.2 shows a few lines over the full width of the camera picture of the tilted target.

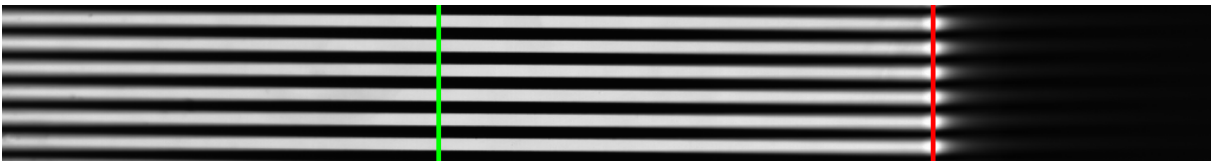


**Figure 6.2.:** Part of a camera picture of the tilted Ronchi ruling. The red line indicates the water surface. The sharpest horizontal profile is indicated with the green line.

The width of the PSF  $H(x)$  is determined here by taking the derivative of the Ronchi ruling in the direction of the image columns. A profile of the Ronchi ruling along an image column is described with the Heaviside step function  $\Theta(x)$ . The image  $g(x)$  of this profile is the convolution of the PSF  $H(x)$  of the optical system with the Heaviside step function  $\Theta(x)$ .

$$g(x) = \int_{-\infty}^{\infty} H(x') \cdot \Theta(x - x') dx' \quad (6.3)$$

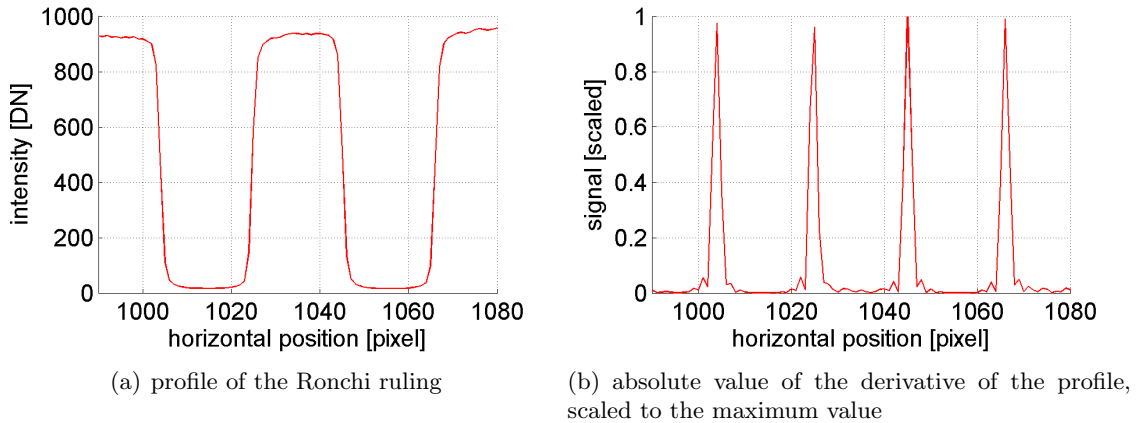


**Figure 6.3.:** Profile and derivative along an image column of the imaged Ronchi ruling (Figure 6.2).

The derivative of the profile  $g(x)$

$$\begin{aligned}
 \frac{\partial}{\partial x} g(x) &= \frac{\partial}{\partial x} \int_{-\infty}^{\infty} H(x') \cdot \Theta(x - x') dx' \\
 &= \int_{-\infty}^{\infty} H(x') \cdot \delta(x - x') dx' \\
 &= H(x)
 \end{aligned} \tag{6.4}$$

is the point spread function  $H(x)$ .

Figure 6.3(a) shows an imaged profile of the Ronchi ruling along an image column (the function  $g(x)$ ). The profile was evaluated by subtracting the dark image. We can see that the edges are not sharp due to the blurring of the image with the PSF. The derivative of the profile was calculated using a recursive lowpass correction filter with a weighted least-squares optimization. The filter was taken from the book [Jähne, 2004, table 12.4, R=2]. Figure 6.3(b) shows the absolute value of the derivative of the profile in Figure 6.3(a).

According to Pentland [1987], the point spread function is best approximated by a two-dimensional Gaussian function. For our case of a one-dimensional profile, a one-dimensional Gaussian function was used. The PSF of the optical system can be approximated with a Gaussian function with a standard deviation of

$$\sigma_{\text{obj}} = 8.3 \mu\text{m} \tag{6.5}$$

in object coordinates. This value was obtained by fitting a Gaussian function to each of the peaks in Figure 6.3(b) and calculating the mean width of the Gaussian fit functions. This measure was identified for every column of the image of the Ronchi ruling (Figure 6.2). The Gaussian function with the smallest width was taken for the best approximation of the PSF of the optical system.

## 6.2. Calibration of the LIF Saturation

A precise determination of the damping factor  $\epsilon_D$

$$\epsilon_D(\vec{x}) = \frac{E_{\text{sat}}}{E(\vec{x}) + E_{\text{sat}}} \quad (6.6)$$

is crucial to calculate the  $\text{O}_2$  concentration from the LIF images with equation (3.1). The damping factor  $\epsilon_D$  depends on laser irradiance  $E(\vec{x})$  and saturation irradiance  $E_{\text{sat}} = \frac{\gamma}{\sigma_a}$  (equation (2.75)). Each time the laser irradiance  $E(\vec{x})$  changes due to a change of the laser collimation, the damping factor  $\epsilon_D(\vec{x})$  has to be determined new. For the measurement of the Stern-Volmer constant  $K_{\text{SV}}$  (Section 5.2.1) at the test wind-wave tunnel, the damping factor  $\epsilon_D$  was only determined for a small region of the laser where the irradiance was constant. The systematic LIF measurements were performed at the Heidelberg linear wind-wave tunnel. Therefore, the laser collimation for the LIF measurements was changed compared to the Stern-Volmer measurements and had to be repeated. For the LIF measurements, the dependence of the position  $\vec{x}$  of the damping factor  $\epsilon_D(\vec{x})$  had to be measured, because the laser irradiance changed within the measuring section.

A method to determine the damping factor  $\epsilon_D$  is presented in Section 3.2.2. This method was applied for 26 laser power values  $P$  between 0 mW and 80 mW and at five values of  $\text{O}_2$  concentrations between  $0.6 \text{ mg L}^{-1}$  and  $8.7 \text{ mg L}^{-1}$ . Figure 6.4 shows a typical calibration picture of the laser line with a used sensor area of  $50 \times 2048$  pixels, the same area as used during the LIF measurements. For the calibration pictures, the water level in the tank was higher as during the

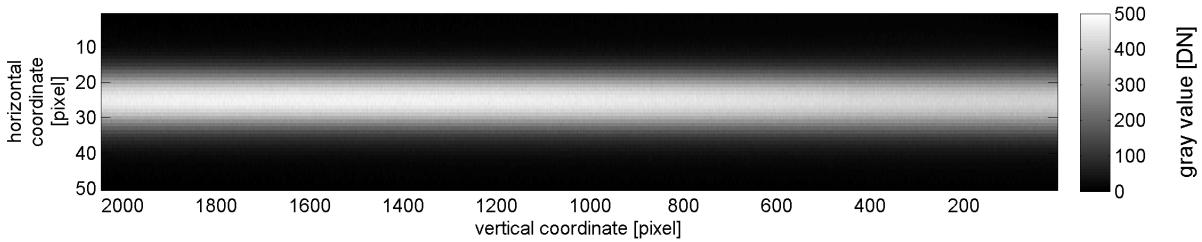


**Figure 6.4.:** Calibration picture of the laser line. As in the previous shown camera pictures, the camera is tilted 90 degrees to the left. The water surface is not visible as it is above the field of view of the camera.

LIF measurements, so that also the positions above the mean water level are calibrated. This is important to calculate the concentration for the case of a wavy water surface.

The saturation laser power  $P_{\text{sat}}$  was calculated pixelwise, as shown for the Stern-Volmer calibration in the Figures 5.3 and 5.4. The damping factor  $\epsilon_D(\vec{x})$  was calculated using equation (3.11) for a laser power  $P$  of 41.59 mW, that was used for the LIF measurements. Figure 6.5 shows the damping factor  $\epsilon_D$  for the central line of the laser and for a line three pixels away from the center. The figure shows that the damping factor  $\epsilon_D$  is lower for the central laser position. This is expected from equation (6.6) as the laser irradiance  $E$  is highest in the center of the laser line. The damping factor  $\epsilon_D(\vec{x})$  drops towards the water surface as the laser is better focused near

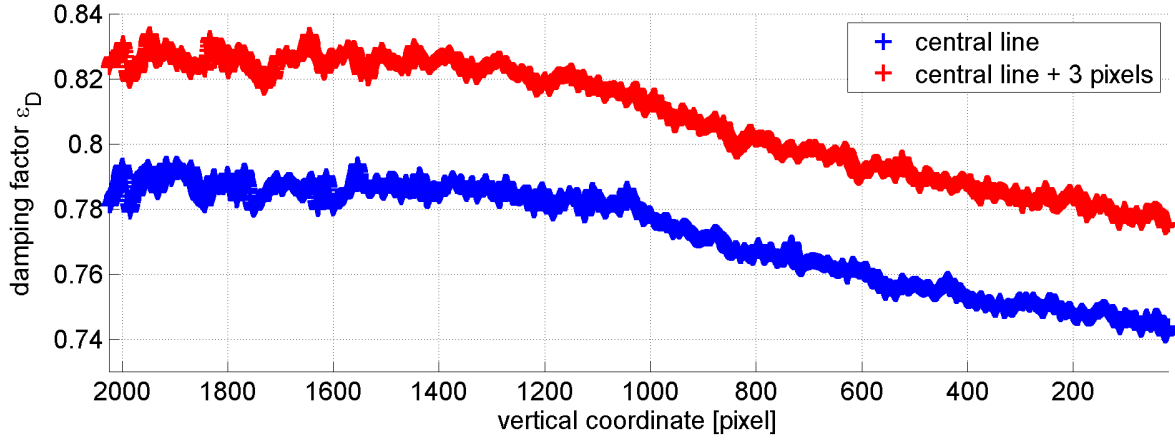


**Figure 6.5.:** Damping factor  $\epsilon_D$  with respect to the sensor position for i) the central laser line and ii) 3 pixels right of the laser line.

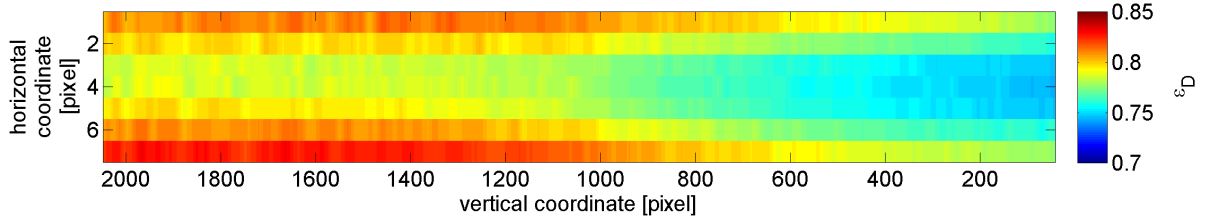


**Figure 6.6.:** Colormap of the damping factor  $\epsilon_D(\vec{x})$  for all laser positions ( $7 \times 2048$  pixels) used in the further data processing steps.

the surface (around vertical coordinate 100), leading to a higher laser irradiance  $E$ .

The value of the damping factor  $\epsilon_D$  was only determined in the region of the laser beam that was used for the further data analysis in the seven central pixels of the laser beam. A colormap of this region is shown in Figure 6.6.

### 6.3. Calibration of the LIF Signal in Absence of Oxygen

The determination of the photon flux  $\Phi_0$  without  $O_2$  is essential in order to calculate  $O_2$  concentrations with the LIF measurements according to equation (3.1):

$$c = \left( \frac{\Phi_0}{\Phi} - 1 \right) \cdot \frac{1}{K_{SV} \cdot \epsilon_D} \quad (6.7)$$

The procedure how to measure the photon flux  $\Phi_0$  is given in Section 3.2.3.

The photon flux  $\Phi$  depends on laser irradiance  $E$  and has to be calibrated independently for every pixel. For the calibration, the calibration pictures were taken at a laser power  $P$  of 41.59 mW, that was used for the LIF measurements, and at five different  $O_2$  concentration values in the water. The calibration data is part of the dataset used to calculate the damping factor  $\epsilon_D(\vec{x})$ . Figure 6.7 shows the measurement of the photon flux  $\Phi_0$  as an example for one pixel in

## 6. Calibration

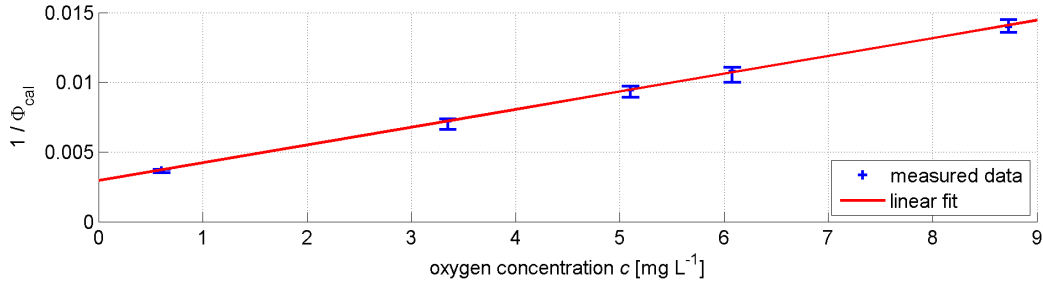


**Figure 6.7.:** Oxygen concentration with respect to the inverse calibration photon flux  $\Phi_{\text{cal}}^{-1}$ . The offset of the linear fit is the inverse photon flux  $\Phi_0^{-1}$ .

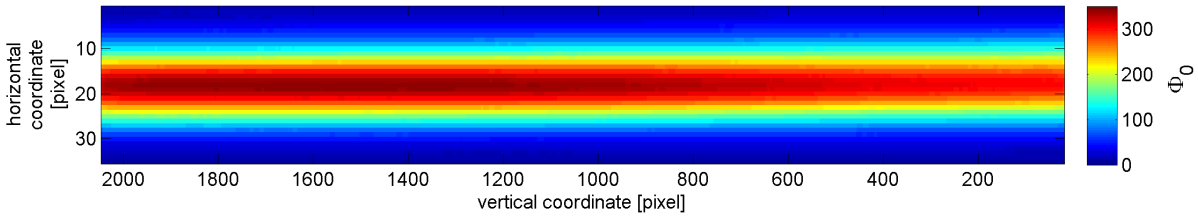


**Figure 6.8.:** Colormap of the calibrated photon flux  $\Phi_0$  without  $\text{O}_2$  at a laser power of 41.59 mW.

the center of the laser line. As explained in Section 3.2.3, equation (3.12)

$$\frac{1}{\Phi_{\text{cal}}} = \frac{1}{\Phi_0} \cdot (1 + K_{\text{SV}} \cdot \epsilon_{\text{D}} \cdot c_{\text{cal}}) \quad (6.8)$$

is fitted to the data. The photon flux  $\Phi_0$  is obtained as the offset of the linear fit.

Figure 6.8 shows a colormap of the photon flux  $\Phi_0$  for the full width and 35 lines of the image sensor. The signal  $\Phi_0$  drops towards the water surface. The reason for this effect is that the laser irradiance  $E$  near the surface (right side of the picture) is higher than in deeper regions (left side of the picture). Therefore, less molecules of the Ru complex near the water surface are excited than in the deeper regions on the left side of Figure 6.8. Accordingly, the photon flux  $\Phi_0$  near the water surface is lower compared to the water bulk. This fact is also shown by the colormap of the damping factor  $\epsilon_{\text{D}}(\vec{x})$  in Figure 6.6. To imagine the propagation of the laser beam, a visualization of the cross section of the laser beam along the light path is shown in Figure 4.8.

## 7. Experiments

The experiments conducted in the framework of this thesis are organized in three parts. Before the systematic LIF measurements were conducted, preparatory experiments were performed to measure the Stern-Volmer constant  $K_{SV}$  of the Ru complex and to optimize the LIF setup (Section 7.1). Section 7.2 depicts the measurement of the forcing parameters, friction velocity  $u_*$  and mean square slope  $\langle s^2 \rangle$ , with respect to fetch  $X$  and wind engine frequency  $F^1$  of the Heidelberg linear wind-wave tunnel. In Section 7.3, the main gas exchange experiments are described. LIF measurements were conducted to study the temporal development of Oxygen ( $O_2$ ) concentration profiles, mean  $O_2$  concentration profiles,  $O_2$  concentration fluctuation profiles, and the local transfer velocity  $k_{LIF}$ . For comparison, the bulk transfer velocity  $k_b$  was determined with the mass balance method. In contrast to the local transfer velocity  $k_{LIF}$ , the bulk transfer velocity  $k_b$  is an averaged value over the total water surface.

### 7.1. Preparatory Experiments

This section provides only an overview of the preparation steps with links to the corresponding section with further information.

A calibration of the Stern-Volmer constant  $K_{SV}$  of the Ru complex had to be performed in order to measure  $O_2$  concentrations with the LIF method. Section 5.2 describes the measurement of the Stern-Volmer constant  $K_{SV}$  and its temperature dependence.

To optimize the LIF setup (Section 4.2), the laser beam collimation was measured. With a beam expander, the laser beam was focused, so that the beam waist is located at the water surface. This was important to achieve a high depth resolution and to optimize the SNR of the measured photon flux  $\Phi$ . The measurements of the laser beam collimation are described in Section 4.2.3.

The LIF measurements (Section 7.3.1) were carried out with the laser in the pulsed mode because it was found that using the laser in the cw (continuous wave) mode leads to large RMS fluctuations  $\Phi'_{RMS}/\bar{\Phi}$  of the emitted photon flux  $\Phi$  by the fluorophore on the order of 10%. This effect was examined and is described in Section 3.1.2. A low duty cycle of the laser helps to minimize the RMS fluctuations. The higher the wind speed, the higher is the acceptable duty cycle of the laser due to a faster local flow velocity of the water in the measuring volume. During

---

<sup>1</sup>The wind engine frequency  $F$  given in this section and the following chapters is the frequency of the *Sinamics G110* frequency converter.

## 7. Experiments

the preparatory experiments, the lowest possible laser pulse rate was determined for which the surface detection algorithm was still applicable.

For the LIF measurements, the laser power  $P$  was 41.6 mW, which corresponds to about 50 % of the available power, because it was observed that a reduction of the laser irradiance lowers the RMS fluctuation  $\Phi'_{\text{RMS}}/\bar{\Phi}$  of the photon flux  $\Phi$ . The SNR at 50 % of the available power was sufficient for the measurements.

### 7.2. Measurement of Forcing Parameters

Common parameters that are used for the parametrization of the gas transfer velocity are the friction velocity  $u_*$ , the wind speed 10 m above the water surface  $u_{10}$ , the mean square slope  $\langle s^2 \rangle$ , and the kinetic energy flux TKE [Wanninkhof et al., 2009]. At the Heidelberg linear wind-wave tunnel, where the gas exchange experiments were performed, the friction velocity  $u_*$  and the mean square slope  $\langle s^2 \rangle$  are accessible parameters. The adjustable parameters during the LIF measurements are the fetch  $X$  and the wind engine frequency  $F$ . The parameters  $u_*$  and  $\langle s^2 \rangle$  were systematically measured as a function of the wind engine frequency  $F$  and the fetch  $X$ . The measurements and the results for the friction velocity  $u_*$  are described in Section 7.2.1. In Section 7.2.2, the mean square slope  $\langle s^2 \rangle$  is presented as a result of the wave measurements.

#### 7.2.1. Wind Speed and Friction Velocity

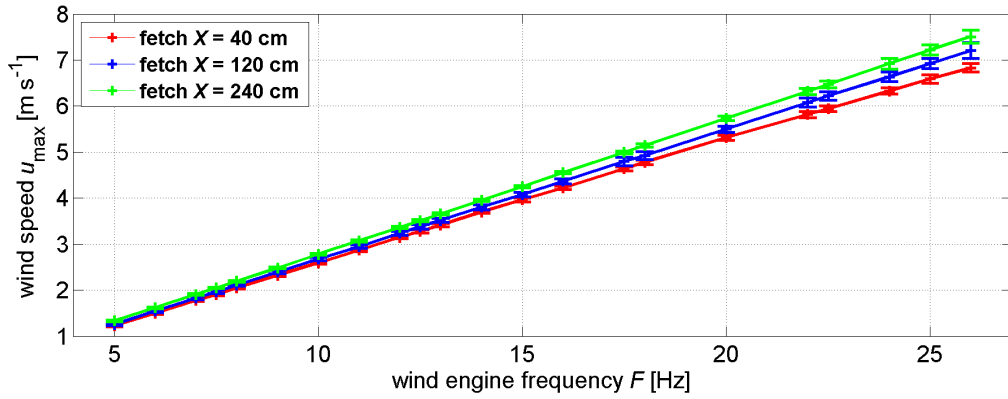
To obtain the friction velocity  $u_*$ , wind profiles were measured for wind engine frequencies  $F$  between 4 Hz and 26 Hz in steps of 1 Hz at a fetch  $X$  between 40 cm and 240 cm in steps of 20 cm<sup>2</sup>. The wind profiles were measured with a Pitot tube, see Section 3.4. During the wind profile measurements, the lower limit of the Pitot tube was at a distance  $z$  between 2 mm and 5 mm from the mean water surface, depending on the wave height. The height of the Pitot tube was changed with increments of 0.5 mm, 1 mm, and 5 mm up to a height of about 20 mm, 55 mm, and 160 mm, respectively. At each height, 20 values of the differential pressure were measured. The data was processed as described in Section 8.1. The results of the friction velocity  $u_*$  for the measured fetch and wind conditions are shown in Section 9.1. An overview of the wind speed  $u_{\text{max}}$  and the friction velocity  $u_*$  is given in Figures 7.1(a) and 7.1(b), respectively. The reference wind speed  $u_0$  is determined from a linear fit to the wind speed  $u_{\text{max}}$  at the maximum measured fetch position of 240 cm:

$$u_0(F) = -0.145 \frac{\text{m}}{\text{s}} + F \cdot 0.2934 \frac{\text{m}}{\text{s}} \frac{1}{\text{Hz}}. \quad (7.1)$$

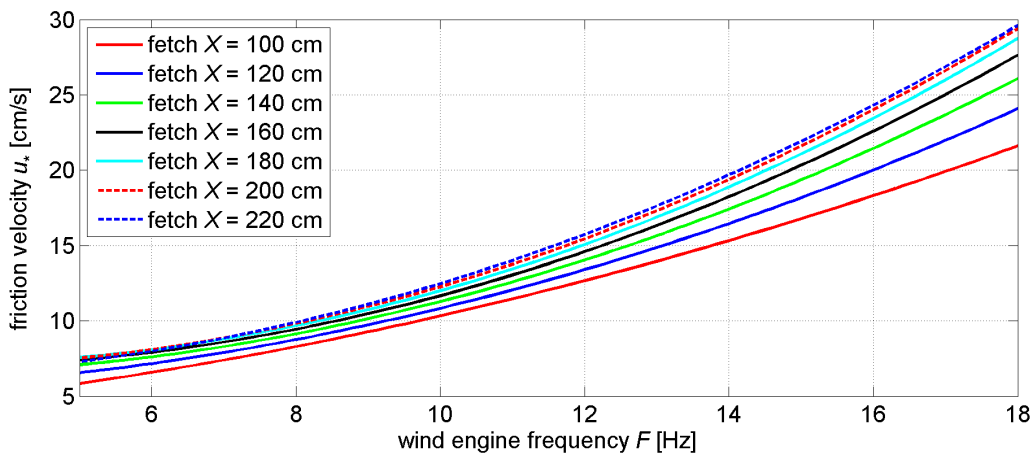
The reference wind speed  $u_0$  is used in this study to specify the wind speed. The friction velocities  $u_*$  used for the parametrization of the transfer velocities  $k_{\text{LIF}}$  in Section 9.6.3 are shown in Figure 7.1(b).

---

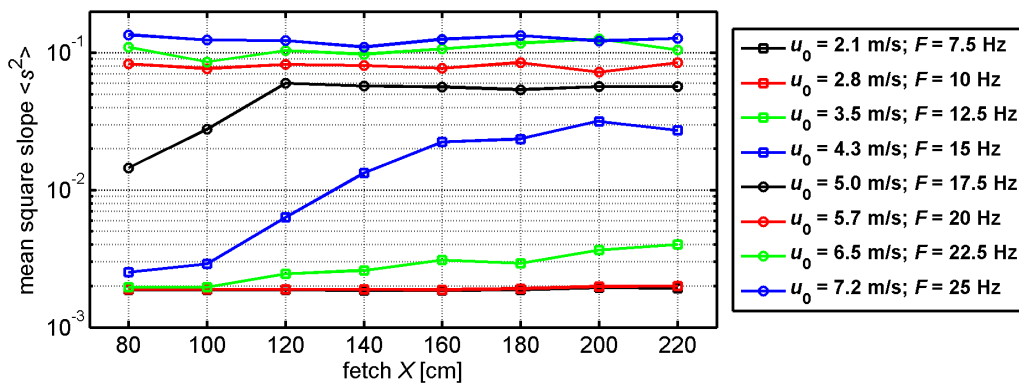
<sup>2</sup>The systematic measurements of wind profiles were conducted by Maximilian Bopp.



(a) Maximum wind speed  $u_{\max}$  with respect to the frequency  $F$  of the wind engine for the fetch  $X$  of 40 cm, 120 cm, and 220 cm.



(b) Friction velocity  $u_*$  with respect to the wind engine frequency  $F$  for fetch  $X$  between 100 cm and 220 cm.



(c) Mean square slope  $\langle s^2 \rangle$  with respect to the fetch  $X$ , measured at different wind speeds  $u_0$  as indicated in the legend.

**Figure 7.1.:** Overview of the forcing parameters with respect to wind engine frequency  $F$  and fetch  $X$ .

### 7.2.2. Wave Measurements

The distribution of the energy in the wave field in the linear tank was measured by Roland Rocholz [Rocholz et al., 2012]. From these measurements only the mean square slope,  $mss$ , is used in this thesis. Mean square slope  $mss$  is directly proportional to the energy density of capillary waves, which mainly constitute the roughness of the water surface. Therefore, mean square slope  $mss$  is a prominent parameter for a physically based parametrization of gas exchange.

Mean square slope values  $mss$  were measured with a wave imaging technique which gives images of water surface slope in  $x$ - and  $y$ -direction, i.e.  $[\partial_x, \partial_y]^T \eta(x, y, t) = [s_x(x, y, t), s_y(x, y, t)]^T$ , where  $\eta$  is the water surface elevation. The mean square slope is the sum of the variances of the  $x$ - and  $y$ -component of the surface slope:

$$mss \equiv \langle s^2 \rangle \equiv \langle s_x^2 \rangle + \langle s_y^2 \rangle. \quad (7.2)$$

Since the surface slope is imaged, the measurement technique is referred to as the *imaging slope gauge*, or ISG for brevity. The setup at the Heidelberg linear wind-wave tank resembles very much the classical setup of Jähne and Riemer [1990], but the modern setup was built with a high speed camera and telecentric lens for observation, and a programmable LED array for illumination. This setup and its calibration are described in Fahle [2012].

The mean square slope  $\langle s^2 \rangle$  was ensemble averaged for a fetch  $X$  between 80 cm and 220 cm in steps of 20 cm and for wind engine frequencies  $F$  between 7.5 Hz and 25 Hz in steps of 2.5 Hz. The water surface was kept clean from surfactants by allowing the water to escape via a level drain at the downstream end of the wind tunnel. The water level was maintained constant by refilling the wind tunnel to the level which adapted itself for zero wind via the level drain. The measurements were reproducible and obtained separately from the gas exchange measurements. The results of the mean square slope measurements are displayed in Figure 7.1(c) for reference.

## 7.3. Gas Exchange Experiments

The gas exchange measurements presented in this study were performed at the Heidelberg linear wind-wave tunnel (Section 4.1.1). LIF measurements (Section 7.3.1) were performed at various combinations of fetch  $X$  and wind engine frequencies  $F$ . The fetch  $X$  was varied using a translation stage that can be shifted in wind direction, on which the LIF setup was mounted. One result of the LIF measurements is the local transfer velocity  $k_{\text{LIF}}(X, F)$  with respect to fetch  $X$  and wind engine frequency  $F$ . For comparison, the bulk transfer velocity  $k_b(F)$  was determined with the mass balance method (Section 3.3) by measuring the temporal change of the  $\text{O}_2$  concentration in the bulk during the invasion process of  $\text{O}_2$  for different wind engine frequencies  $F$  (see Section 7.3.2). The LIF and the bulk measurements were not performed at the same time. However, the results are comparable since the conditions of the friction velocity

**Table 7.1.:** Summary of the conditions of the wind engine frequency  $F$  and fetch  $X$  at which the LIF measurements were performed. The letters A, B, and C indicate the set of data: A is the measurement at fetch 140 cm, B the fetch dependent measurement, and C is the measurement with a low duty cycle of the laser.

$F$ [Hz]	5	6	7	8	9	10	11	12	13	14	15	16	17	17.5	18 - 26
$X = 100$ cm	B					B					B			B	
$X = 120$ cm											B			B	
$X = 140$ cm	A	A	A	A	A	A	A	A	A	A	A	A	A	B	A
$X = 160$ cm											B			B	
$X = 200$ cm											B			B	
$X = 220$ cm	B/C					B					B			B	

**Table 7.2.:** Laser pulse rates and corresponding camera frame rates and laser duty cycles depending on the wind engine frequency  $F$  during the  $O_2$  invasion measurements (valid for data set A and B). The duty cycles were calculated based on a pulse length of 0.45 ms.

wind engine frequency $F$ [Hz]	5 - 14	15	16 - 17	17.5 - 18
laser pulse rate / camera frame rate [Hz]	500	750	1000	1200
duty cycle of laser [%]	22.5	33.75	45	54

$u_*$  and the mean square slope  $\langle s^2 \rangle$  in the wind-wave tunnel are reproducible.

### 7.3.1. LIF Measurements

**Measured Conditions** LIF measurements were performed at the Heidelberg linear wind-wave tunnel (Section 4.1.1) with the setup described in Section 4.2 in three sets of data. The conditions of fetch  $X$  and wind engine frequency  $F$  for data sets A, B, and C are listed in Table 7.1. All data sets were obtained with a camera exposure time  $\tau_{\text{exp}}$  of 0.45 s and an aperture  $n_f$  of 4 in sequences containing  $10^4$  images. The images have a pixel resolution of 50 pixels  $\times$  2048 pixels and a bit depth of 10 bit. The number of sequences that was recorded at every condition of fetch  $X$  and wind engine frequency  $F$  was 5, 15, and 1 for data set A, B, and C, respectively. The camera frame rates and laser duty cycles for data set A and B are listed in Table 7.2. Data set A was recorded in the period from August, 16th to 21st 2012. Data set B was taken to measure  $O_2$  concentration profiles and transfer velocities  $k_{\text{LIF}}$  at varying fetch. It was measured in the period between October, third and fifth 2012. It turned out that the high laser pulse rate at the wind engine frequencies  $F$  of 5 Hz and 6 Hz led to an overestimated  $O_2$  concentration, as explained in Section 3.1.2. Therefore, the measurement at  $F = 5$  Hz was repeated at a lower laser pulse rate of 10 Hz with a corresponding duty cycle of 0.45 % at the fetch of 220 cm (data set C). This data set was recorded on October, 29th 2012 to study the RMS  $O_2$  concentration fluctuations (see Section 9.5). Unwanted fluctuations, as presented in Section 3.1.2, were avoided due to the low duty cycle of 0.45 % of the laser. Such a low duty cycle could only be applied at a flat water surface. In the presence of waves, a high camera frame rate is required for the detection of the water surface (see Section 8.2.2).

## 7. Experiments

**Measurement Procedure** To study the  $O_2$  transport from the air to the water, an invasion experiment was performed. The  $O_2$  concentration in the water phase was lowered, while the  $O_2$  concentration in the air remained constant. Before a LIF measurement was started, most of the  $O_2$  solved in the water was pumped out with the equilibrator until the  $O_2$  concentration reached a value of about  $2\text{ mg L}^{-1}$ . The temperature of the water in the wind-wave tunnel was adjusted to  $23^\circ\text{C}$  with the Peltier temperature control while the water was degassed. The temperature was at a constant value during all gas exchange experiments, to have a constant value for the diffusion constant  $D$  and for the Stern-Volmer constant  $K_{SV}$ . Once the water-sided  $O_2$  concentration reached the desired value of about  $2\text{ mg L}^{-1}$ , the circulation pumps and temperature control were switched off to observe no influence by convection processes and flow due to pumps during the measurements. The desired wind engine frequency  $F$  and fetch  $X$  were set. After waiting for several minutes, to be sure that equilibrium conditions of the wave field were established, the LIF image sequences were taken with the LIF setup (Section 4.2). The data processing of the LIF images is described in Section 8.2. The results of the LIF measurements comprise  $O_2$  concentration images in Section 9.2, mean  $O_2$  concentration profiles in Section 9.4, RMS  $O_2$  concentration fluctuation profiles in Section 9.5, and  $O_2$  transfer rates  $k_{LIF}$  in Section 9.6.

### 7.3.2. Bulk Measurements

**Measured Conditions** Oxygen transfer velocities  $k_b$  averaged over the total water surface were measured for wind engine frequencies  $F$  between 0 Hz and 26 Hz in steps of 1 Hz by measuring the temporal change of the  $O_2$  concentration in the bulk during the  $O_2$  invasion process. The measurements were conducted between August, 16th and September, first 2012.

**Measurement Procedure** Before the experiments were started, the same arrangements as for the measurement of the  $O_2$  concentration profiles (Section 7.3.1) were made. The  $O_2$  concentration in the water was lowered and the temperature of the water was set to  $23^\circ\text{C}$ . After the water-sided  $O_2$  concentration reached the desired value of about  $2\text{ mg L}^{-1}$ , the temperature control and all circulation pumps except for the measuring bypass pump were switched off. The wind engine frequency  $F$  was adjusted and the  $O_2$  concentration was measured every five seconds with the oxygen probe in the measuring bypass until the  $O_2$  concentration in the water reached equilibrium. The data processing of the bulk measurements is described in Section 8.3. In Section 9.6.2, the transfer velocities  $k_{LIF}$  obtained with the LIF measurements are compared to the bulk transfer velocities  $k_b$ .

## 8. Data Processing

Section 8.1 describes how the friction velocity  $u_*$  was obtained from the wind profile measurements. The data processing for the two methods used in this thesis to measure the local transfer velocity  $k_{\text{LIF}}$  and the bulk transfer velocity  $k_b$  of oxygen ( $\text{O}_2$ ) are explained in Sections 8.2 and 8.3, respectively.

### 8.1. Processing of the Wind Profiles

The friction velocity  $u_*$  was obtained by measurements of wind profiles at different wind speeds and varying fetch  $X$ , following the procedure presented by Troitskaya et al. [2012]. The experimental method of wind profile measurements are described in Section 3.4. The fetch  $X$  and wind engine frequencies  $F$  at which the wind profiles were measured are described in Section 7.2.1. To determine the friction velocity  $u_*$  for each condition, the product of  $u_*$  and a fit parameter  $\beta$  from the wake part of each profile is derived. In Section 8.1.1, it is shown that the wind profiles all collapse on one curve when plotting them in dimensionless coordinates. The parameter  $\beta$  is obtained by a simultaneous fit procedure in dimensionless coordinates to all measured wind profiles in Section 8.1.2.

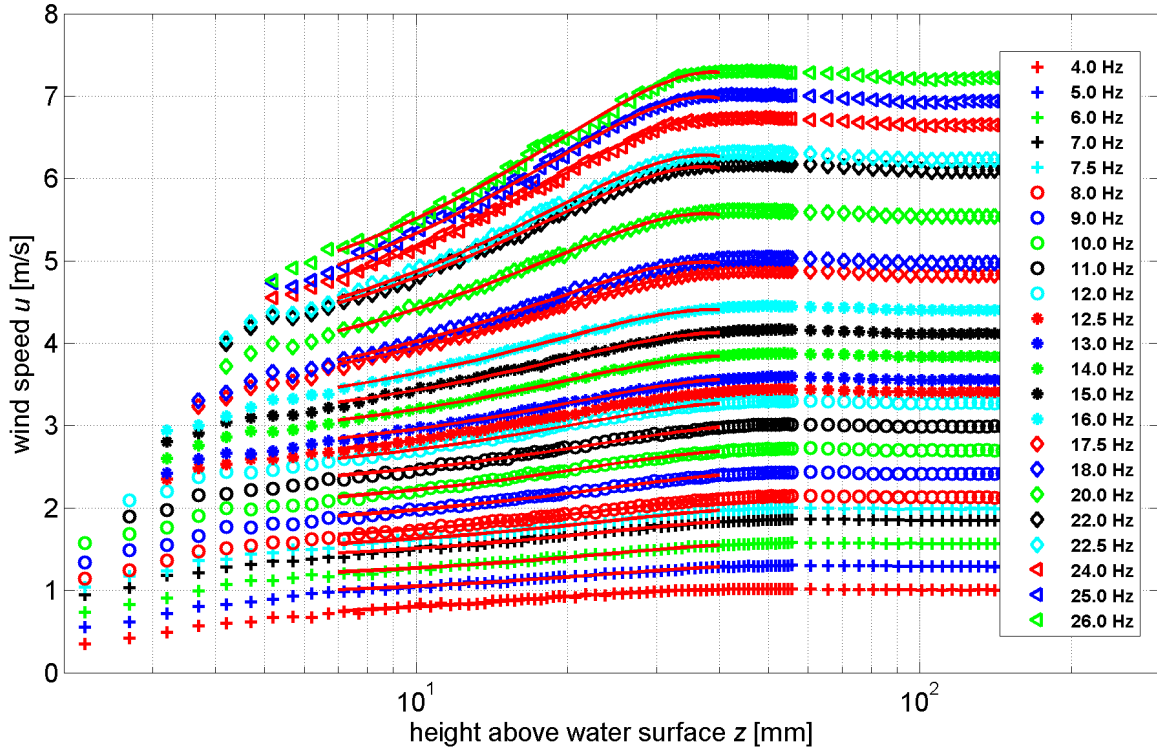
#### 8.1.1. Wind Profiles in Dimensionless Coordinates

Figure 8.1 shows the measured wind profiles at fetch  $X$  of 140 cm. Errors are omitted for a clearer presentation. A polynomial of second order (2.35)

$$u(z) = u_{\max} - \beta \cdot u_* \cdot \left(1 - \frac{z}{\delta}\right)^2, \quad (8.1)$$

is fitted to each of the wind profiles in the wake part (also referred to as outer layer in Section 2.1.3), indicated as red lines in Figure 8.1. Fitting was performed from  $0.15\delta$  to  $\delta$ , where  $\delta$  denotes the 99% boundary layer thickness. The thickness  $\delta$  was detected automatically by fitting equation (8.1) iteratively to the data so that  $\delta$  converges. With the obtained fit parameters, i.e. maximum wind speed  $u_{\max}$ , the product  $\beta \cdot u_*$ , and boundary layer thickness  $\delta$ , the profiles are plotted with the dimensionless wind speed

$$\frac{u_{\max} - u(z)}{u_* \cdot \beta}$$



**Figure 8.1.:** Measured wind profiles at the Heidelberg linear wind-wave tunnel and at a fetch  $X$  of 140 cm for wind engine frequencies  $F$  between 4 Hz and 26 Hz. The  $x$ -axis depicts the height above the water surface without wind. The red lines are polynomials of second order fitted to each wind profile.

and the dimensionless height

$$\eta = \frac{z}{\delta}.$$

From Figure 8.2 it is evident that all profiles at fetch 140 cm are self-similar and collapse on one curve when plotted with dimensionless variables.

### 8.1.2. Determination of the Friction Velocity

To determine the friction velocity  $u_*$  at various combinations of wind speed and fetch, the three parameters  $u_{\max}$ ,  $\beta \cdot u_*$ , and  $\delta$  are retrieved from the quadratic fit function (8.1) in the wake part for each profile. Once the value of  $\beta$  is known, the friction velocity  $u_*$  can be calculated for every profile from the previously determined product  $u_* \cdot \beta$ . The parameter  $\beta$  is obtained by a fit in the fully-turbulent flow region to all measured wind profiles.

Figure 8.3 shows all measured wind profiles in dimensionless variables. Profiles of one run all collapse on one curve, but profiles of different fetch and runs do not all collapse on one curve. However, the wind profiles in Figure 8.3 show no trend with fetch. That leads to the conclusion that the deviation of some profiles (namely at fetch 160 cm, run 2) is possibly due to a systematic error in the measured height  $z$  on the order of 1 mm varying from one run to

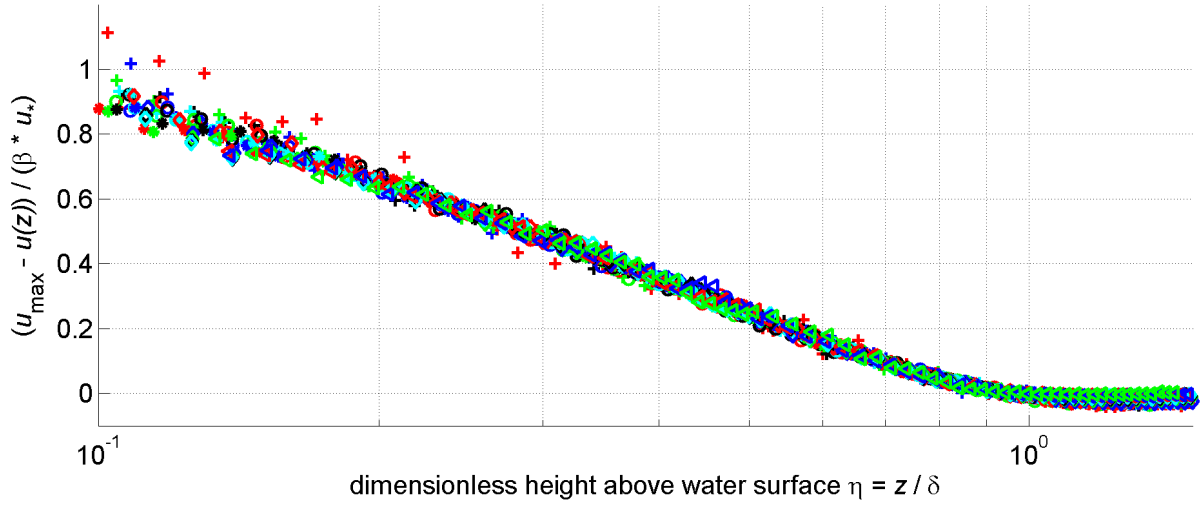


Figure 8.2.: Plot of the wind profiles shown in Figure 8.1 in dimensionless variables. For the legend see Figure 8.1.

another. It is assumed that all profiles have the same form in the fully-turbulent flow region ( $\eta < 0.15$ ) and that  $\beta$  is constant over the measured fetch conditions.

The shape of the wind profile in the logarithmic part is described by equation (2.33). In dimensionless variables, the following equation is obtained:

$$\frac{u_{\max} - u(z)}{\beta \cdot u_*} = \frac{u_{\max}}{\beta \cdot u_*} - \frac{1}{\beta \cdot \kappa} \cdot \ln\left(\frac{\eta \cdot \delta}{z_0}\right). \quad (8.2)$$

By substituting

$$z_0 = \delta \cdot \eta_0 \cdot \exp\left(-\frac{u_{\max}}{u_*} \cdot \kappa\right) \quad (8.3)$$

for the roughness parameter  $z_0$ , a simplified equation for the wind profile in dimensionless variables can be found:

$$\frac{u_{\max} - u(z)}{\beta \cdot u_*} = -\frac{1}{\beta \cdot \kappa} \cdot \ln\left(\frac{\eta}{\eta_0}\right). \quad (8.4)$$

Equation (8.4) was fitted to the total dataset (the data in Figure 8.3) from  $\eta = 0.08$  to  $\eta = 0.15$ . For von Kármán's constant  $\kappa$ , the value of 0.4 (according to Hinze [1975]) was used. The logarithmic fit function returned two parameters, the parameter  $\eta_0$

$$\eta_0 = 1.11 \pm 0.04 \quad (8.5)$$

and the parameter  $\beta$

$$\beta = 6.6 \pm 0.1. \quad (8.6)$$

With the knowledge of the parameter  $\beta$  and the previously obtained product  $\beta \cdot u_*$ , the friction velocity  $u_*$  was obtained for each measured wind speed and fetch.

## 8. Data Processing

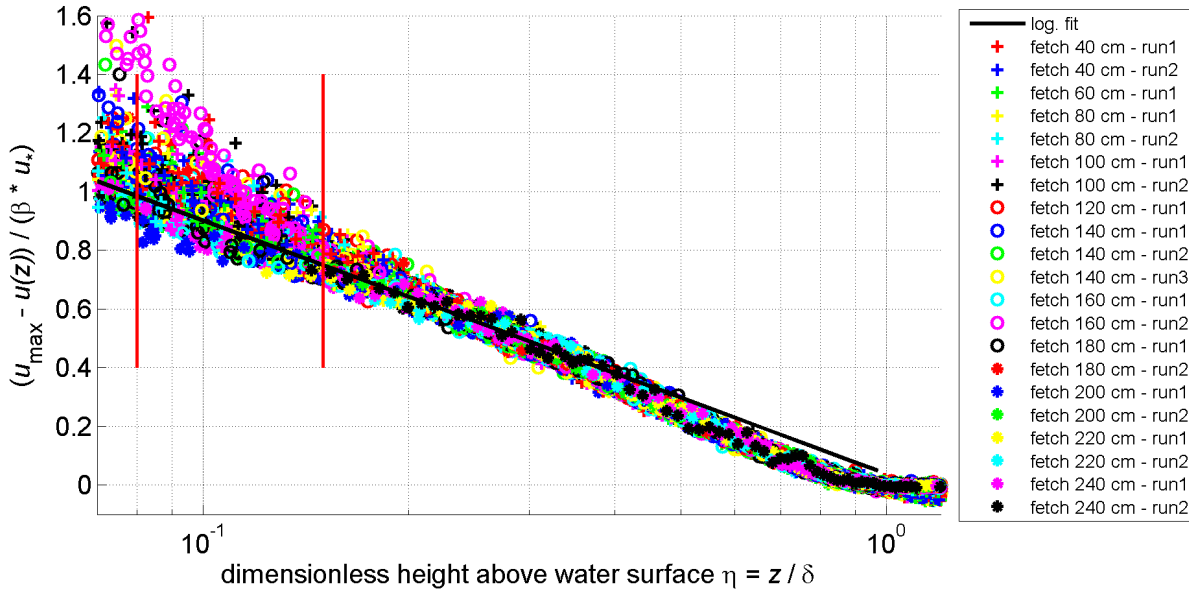


**Figure 8.3.:** Measured wind profiles at the tunnel measured for wind turbine frequencies  $F$  between 4 Hz and 26 Hz and fetches between 40 cm and 240 cm in dimensionless variables. The black line is the logarithmic fit function. The fit region is indicated by the red lines.

### 8.2. Processing of the LIF Data

Data taken during the LIF measurements is saved in digital image sequences. One sequence contains  $10^4$  single frames of  $50 \times 2048$  pixels. Every pixel represents a positive integer value with a resolution of 10 bit. In other words, the image sequences contain gray values between 0 and 1023.

Figure 8.4 shows the steps of the data processing from raw image sequences to  $O_2$  concentration images, mean concentration values, and local transfer velocities  $k_{LIF}$ . After subtracting the dark image, the one-dimensional  $O_2$  concentration profile (2048 pixels) along the laser beam is calculated for all images (Section 8.2.1). The result is a two-dimensional dataset (called  $t-z$  image) with one dimension corresponding to the time  $t$  and the other to the vertical coordinate  $z$ . The entries of such a  $t-z$  image contain floating point numbers representing the  $O_2$  concentration at a given depth and time. The  $t-z$  image allows a qualitative analysis of the  $O_2$  transport under wind-induced turbulence. In the next step, the water surface in the  $t-z$  image is detected, in order to determine the relative depth to the water surface (Section 8.2.2). To obtain a mean concentration profile for one specific fetch  $X$  and wind engine frequency  $F$ , all  $t-z$  image recorded at this condition are averaged over time in relative coordinates to the water surface, see Section 8.2.3. By the principle of ergodicity, RMS  $O_2$  concentration fluctuation profiles are obtained. With the mean  $O_2$  concentration profiles, the thickness  $\delta_{mbl}$  of the mass boundary layer is calculated (see Section 8.2.4). From this data, the local transfer velocity  $k_{LIF}$  is obtained.

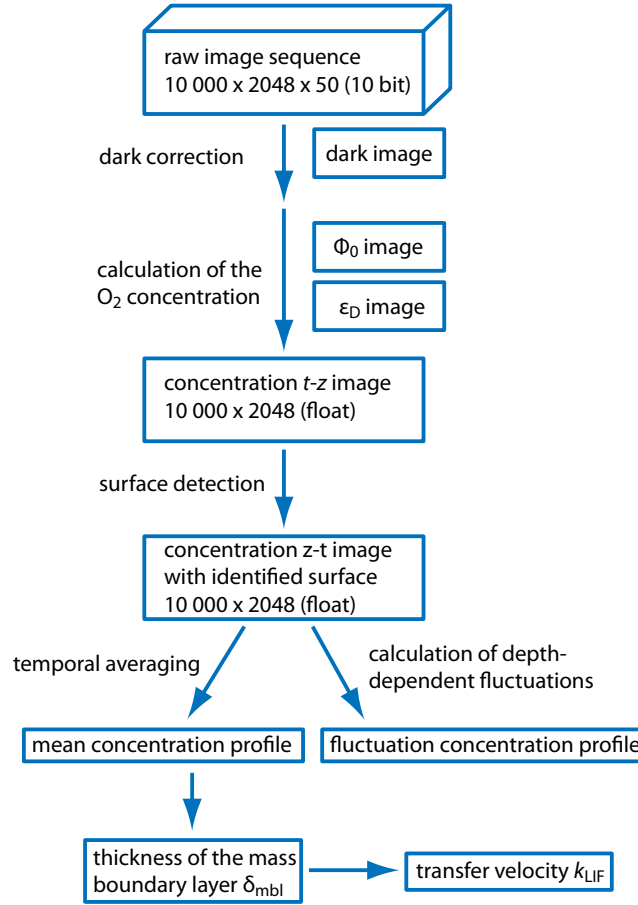


Figure 8.4.: Flow chart for the data processing of the LIF images.

### 8.2.1. Calculation of the Oxygen Concentration

Calculation of the  $O_2$  concentration  $c$  starts with subtracting the mean dark image of the camera. This was further complicated by the so called two-level noise effect of the camera. The error could be eliminated and is described in Section A.4.1. In the next step, equation (3.1)

$$c = \left( \frac{\Phi_0}{\Phi} - 1 \right) \cdot \frac{1}{K_{SV} \cdot \epsilon_D} \quad (8.7)$$

has to be applied to each pixel in the region of the laser beam.

An example of a single image is given in Figure 8.5. To see the FWHM region of the laser beam, 20 lines would be enough. To ensure, however, that the beam is always in the imaged area, 50 lines were chosen. The darker regions in the area of the laser beam in Figure 8.5 denote higher concentrations of  $O_2$ . Above the water surface, we see a reflection of the luminescent light. The reflection is tilted when the surface slope in  $x$ -direction (wind-direction) is different from zero. The camera image is the projection of the 3-dimensional distribution of the luminescent light on the 2-dimensional camera detector. Therefore, the 2-dimensional Gaussian profile of the

## 8. Data Processing

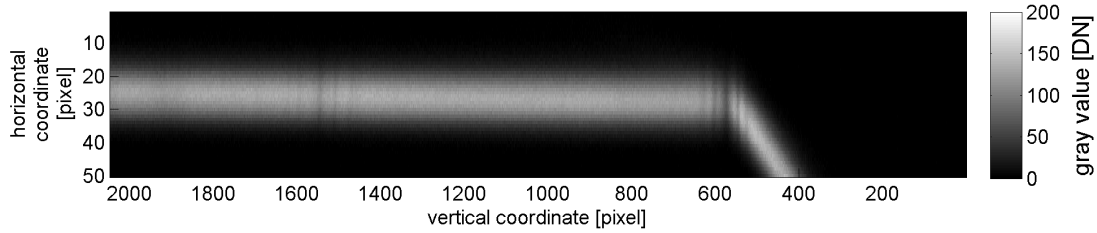
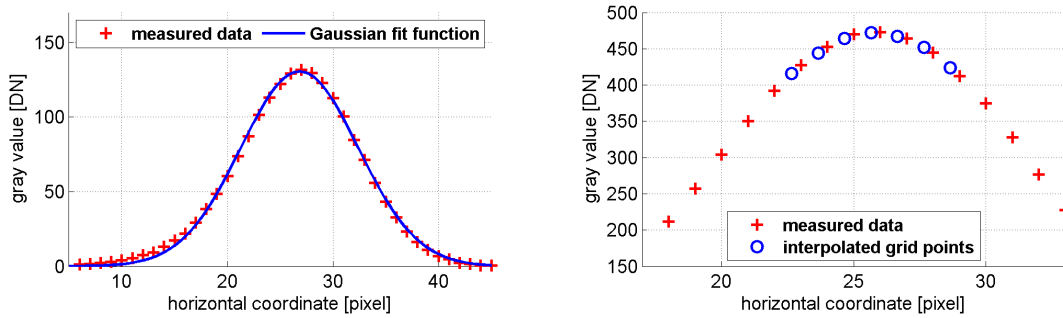


**Figure 8.5.:** Single LIF image of the laser-induced luminescent light. The camera is tilted 90 degree to the left. The surface is visible as a dark vertical line around the vertical coordinate of 600.



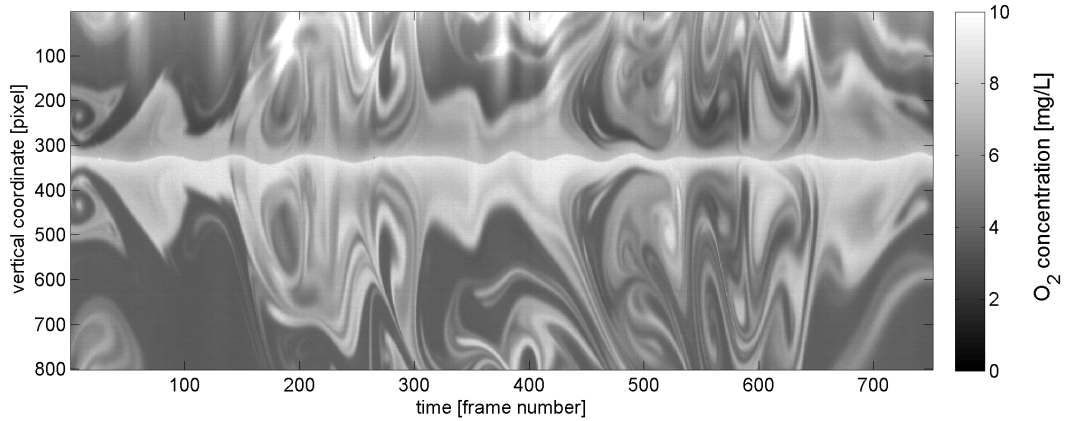
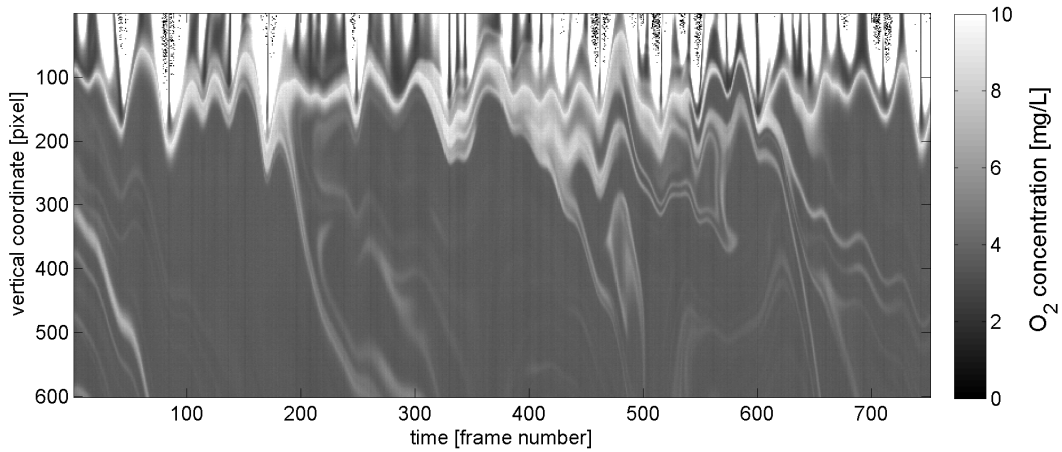
(a) Profile in horizontal direction of the LIF image in Figure 8.5. The Gaussian fit function has a standard deviation of 5.6 pixels. (b) Profile in horizontal direction of a calibration image with seven interpolated grid points around the maximum value of the Gaussian function.

**Figure 8.6.:** Profiles of LIF images in horizontal direction.

laser beam (see Figure 4.8) yields a 1-dimensional profile on the camera detector. An example of such a profile of the laser beam is shown in Figure 8.6(a). The fitted Gaussian curve has a standard deviation of  $34\ \mu\text{m}$ . The order of magnitude is in good agreement with the measured beam profile in Figure 4.9 with a standard deviation around  $25\ \mu\text{m}$ .

**Interpolation of the Centered Image** The recirculation pump causes the experimental setup to vibrate slightly which leads to lateral oscillatory motion of the laser beam by a few pixels. To correct for this effect, the beam center is determined from a Gaussian fit and the gray values at equidistant grid points are obtained by interpolation (see Figure 8.6(b)).

**Calculating the  $t$ - $z$  Picture** For the calculation of the  $\text{O}_2$  concentration from a single LIF image with equation (8.7), the photon flux  $\Phi_0$ , the damping factor  $\epsilon_D$ , the Stern-Volmer constant  $K_{SV}$  at the measured temperature, and the photon flux  $\Phi$  in the recorded LIF image are needed. The calculation of the damping factor  $\epsilon_D$  and of the photon flux  $\Phi_0$  was shown in Sections 6.2 and 6.3, respectively. Concentration values are calculated for all pixels of the vertical coordinate and for the seven central pixels of the horizontal coordinate because the signal-to-noise ratio (SNR) decreases towards the outer region of the Gaussian profile (see Figure 8.6). The obtained two-dimensional concentration image is averaged in horizontal direction, to get a one-dimensional concentration profile for each single LIF image. By calculating the  $\text{O}_2$  concentration for all images of a recorded sequence, the so-called  $t$ - $z$  image is obtained.

(a) wind speed  $u_0 = 2.8 \text{ m s}^{-1}$ ;  $F = 10 \text{ Hz}$ ; fetch  $X = 220 \text{ cm}$ (b) wind speed  $u_0 = 4.3 \text{ m s}^{-1}$ ;  $F = 15 \text{ Hz}$ ; fetch  $X = 220 \text{ cm}$ **Figure 8.7.:** Two examples of  $t$ - $z$  images for low and high surface slopes. The gray values in the images present  $\text{O}_2$  concentrations in units of  $\text{mg L}^{-1}$ .

**Properties of  $t$ - $z$  Images** Figure 8.7 shows two examples of  $t$ - $z$  images. For the case of low surface slopes (see Figure 8.7(a)), a mirrored image of the structures in the water is visible above the water surface. The mirror effect is a crucial feature used to detect the water surface as will be explained in the next section. For higher surface slopes in  $x$ -direction (wind direction), the laser line in the single LIF images is tilted at the water surface, such as the line depicted in Figure 8.5. The angle of inclination is twice the surface slope in  $x$ -direction. The evaluation routine regards only pixels around the center of the vertical laser line. In this strongly tilted case, the image above the surface within this region basically appears dark which results in exaggeratedly high concentration values after calibration with equation (8.7). In conclusion,  $t$ - $z$  images in the case of high surface slopes in  $x$ -direction show bright structures above the water surface and only a mirror image for pixels close to the water surface (see Figure 8.7(b)). A surface slope in  $y$ -direction (cross-wind direction) leads to a mirror image that is tilted out of the focal plane of the camera (see Figure 4.5). For surface slopes in  $y$ -direction greater than

## 8. Data Processing

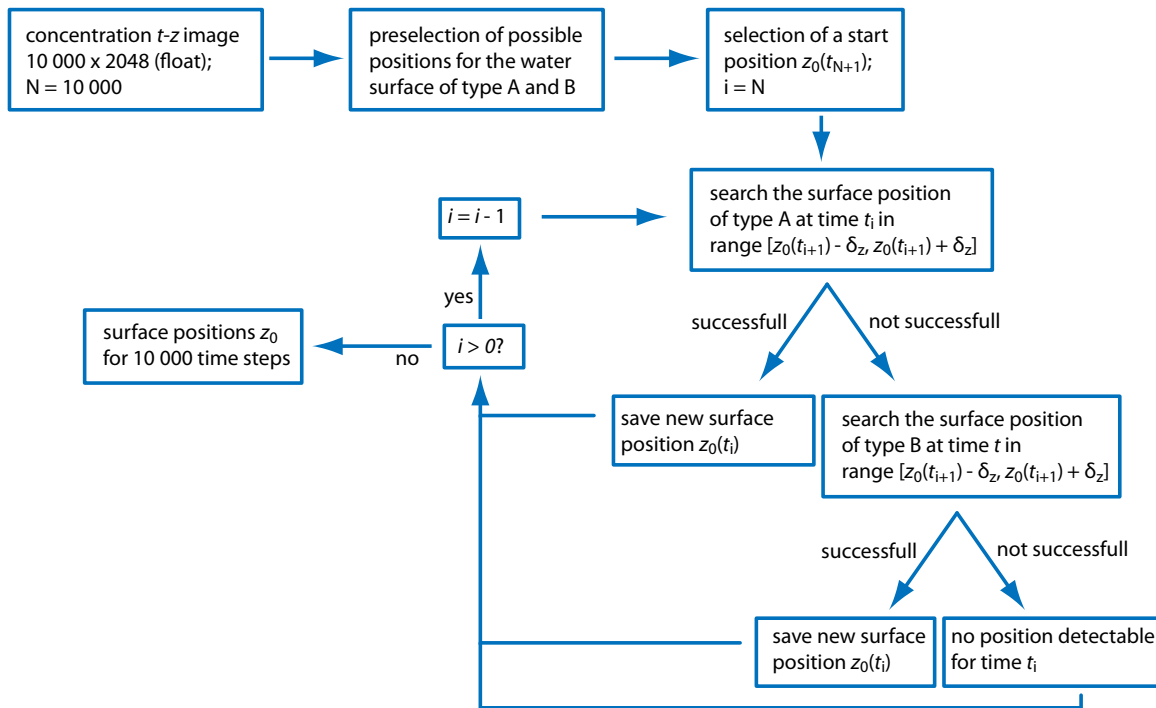


**Figure 8.8.:** Flow chart showing the structure of the surface detection algorithm.

16.5° towards the camera, the water surface is hidden<sup>1</sup>. The water surface in the  $t$ - $z$  images is visible as a continuous bright line because the concentration at the water surface is in equilibrium with the concentration in the air.

### 8.2.2. Detection of the Water Surface

The detection of the water surface in the  $t$ - $z$  images for each time step is crucial for the further data analysis in order to determine the right distance from the water surface. The algorithm requires a  $t$ - $z$  image as input and returns the surface position  $z_0$  for each time step. It is based on the idea that a mirrored image of the concentration profile is visible above the water surface. The  $O_2$  concentration at the water surface is higher than in the water bulk, as invasion experiments are performed in this study. This leads to a local maximum of the  $O_2$  concentration at the water surface for each instantaneous concentration profile. Figure 8.9 shows one concentration profile recorded with a low surface slope, and one recorded with a higher slope, both having a local maximum at the water surface. The algorithm is further based on the criteria that the  $O_2$  concentration at the water surface is in equilibrium with the concentration in the air. The third and crucial criteria used for the algorithm is that the water surface does not move more than a specified number of pixels  $\delta_z$  from one image to the next one, as the images were recorded with a high frame rate (see Table 7.2). The criteria used to detect the water surface give rise to the

<sup>1</sup>explanation for hidden surface see Section 4.2.1

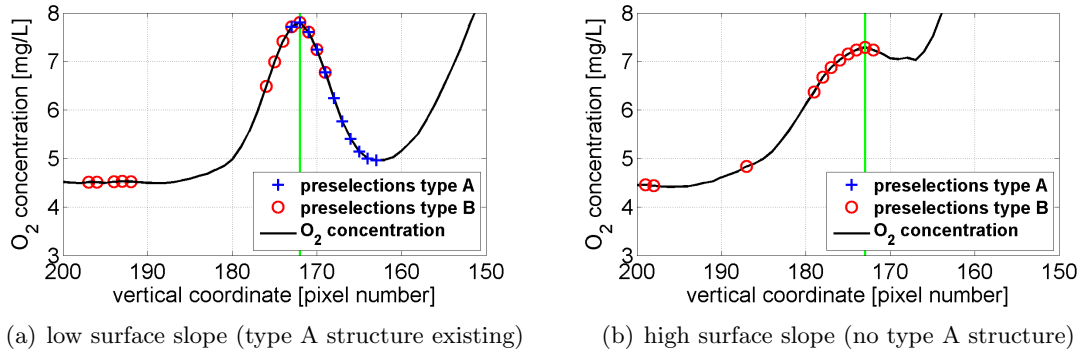


**Figure 8.9.:** Oxygen concentration with respect to the vertical coordinate for two selected time steps. The detected surface position is indicated with a green line. The preselected pixels of type A and B are indicated with blue crosses and red circles, respectively.

limit of the algorithm. For a high surface slope, the instantaneous concentration profiles show no mirrored image and conclusively no local maximum at the water surface. Another problem arises when the surface position moves more pixels than the selected distance  $\delta_z$  from one frame to the next one. The wind speed and fetch conditions for which the surface detection algorithm worked successfully, are listed in Table 9.1. The four principal steps of the surface detection algorithm are described in this section and are illustrated with the flow chart in Figure 8.8.

**Step 1: Preselection** Based on the  $t$ - $z$  image and the first two criteria outlined above (local maximum and surface concentration in equilibrium with air), a preselection of pixels is made which constitute candidates for the surface position. Two kinds of preselections are performed: type A which has to fulfill strong criteria that are only met for low surface slopes and type B with weaker criteria that are also met for higher surface slopes. Figure 8.9 shows concentration profiles for a low and a high surface slope with the indicated pixels for which preselections of type A and type B are fulfilled. The decision for the right surface position is always based on the preselections of type A, if any exists in the specified range. Otherwise, the preselections of type B are used for the selection of the surface position.

The criteria for type A are a negative first derivative of the concentration profile below a specified threshold and a concentration in a specified range around the expected surface concentration value. The range of successful positions is expanded by three pixels in each direction of the vertical coordinate. The criteria for type B are a negative second derivative of the concentration profile and a concentration in the same range as selected for type A. The example in Figure 8.9 illustrates that in the case of a low surface slope the surface position is detected by the preselected pixels of type A. For higher surface slopes, the position of the surface is detected by a preselection of type B.

The first and second derivative of the concentration profile for each time step are calculated on a smoothed  $t$ - $z$  image. The image is smoothed in the direction of the vertical coordinate using a Savitzki-Golay filter [Savitzky and Golay, 1964], which shows a better performance in

## 8. Data Processing

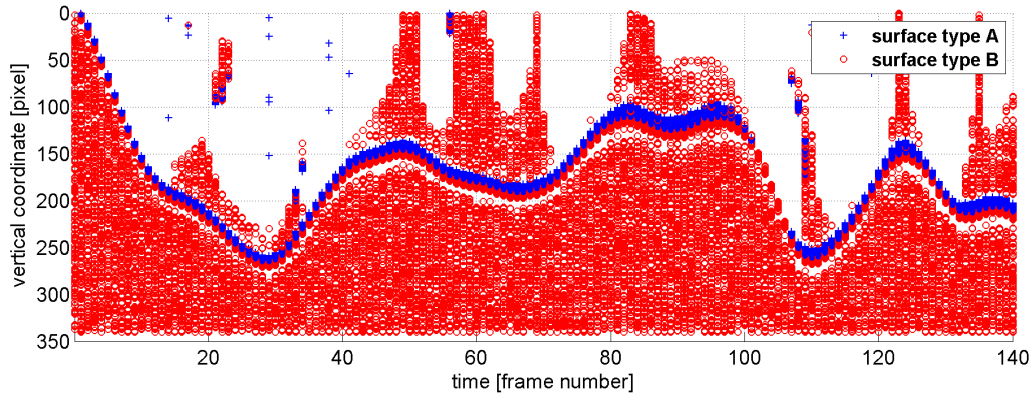


**Figure 8.10.:** Preselected pixels of type A and B for a section of a  $t$ - $z$  picture at a fetch of 220 cm and a wind engine frequency  $F$  of 15 Hz.

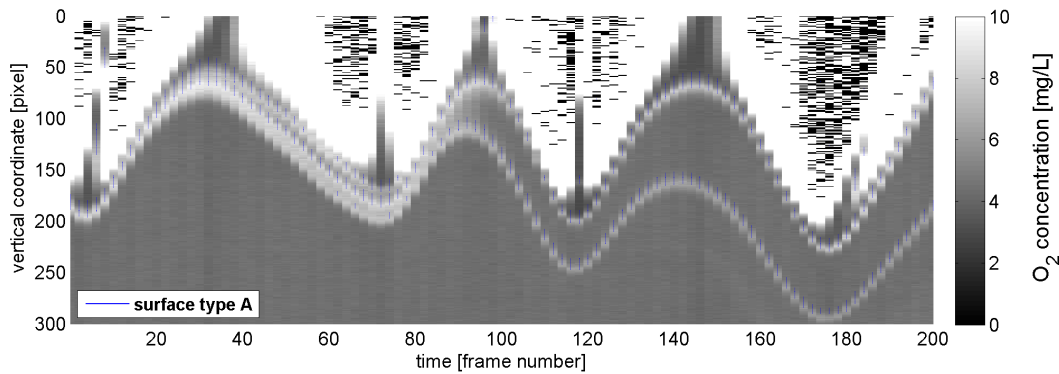


**Figure 8.11.:** Preselected pixels of type A for the case of a flow separation event.

preserving the amplitude of local maxima compared to other smoothing filters.

Figure 8.10 shows an example of preselected pixels of type A and B in a  $t$ - $z$  image. It is more likely to fulfill the requirements for type B than for type A. Preselected pixels of type B cover regions that are obviously no option to be near the surface. Therefore, the type B preselections are only taken into account if type A returns no option.

**Step 2: Selection of a Start Position** The algorithm loops through the profiles backwards in time to prevent the detection of wrong surface positions due to separation events such as the one shown in Figure 8.11. A start position  $z_0(t_{N+1})$  has to be selected manually.

**Step 3: Search the Surface Position of Type A** The position of the water surface at time step  $t_i$  is searched in the range  $[z_0(t_{i+1}) - \delta_z, z_0(t_{i+1}) + \delta_z]$ . This is done by selecting the pixel with the highest  $O_2$  concentration out of all pixels in the range which were identified as the surface position of type A. If there is at least one pixel of type A in the range, a surface position is found and saved as the surface position  $z_0(t_i)$ . The algorithm makes one step back in time ( $i = i - 1$ ) and proceeds at the beginning of step 3. If there was no pixel of type A in the specified range, the routine passes on to step 4.

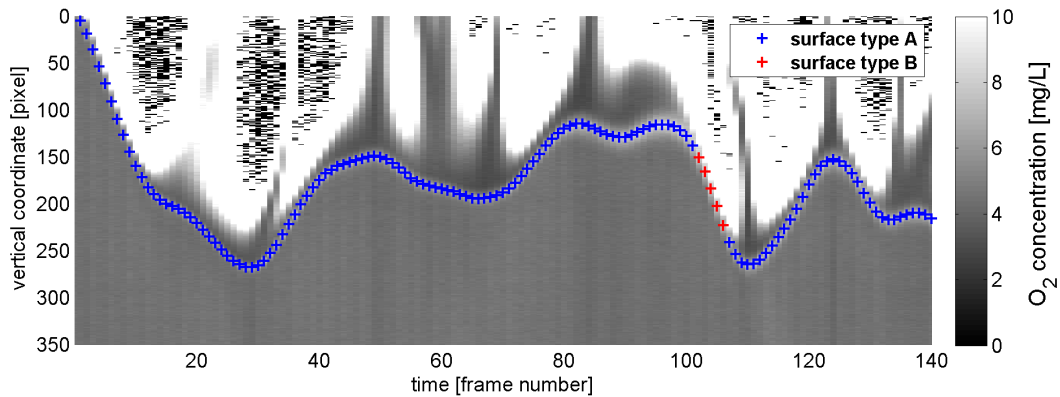


**Figure 8.12.:** Detected surface positions drawn in the section of the  $t$ - $z$  picture shown in Figure 8.10. The blue and the red marker indicate the surface of type A and B, respectively.

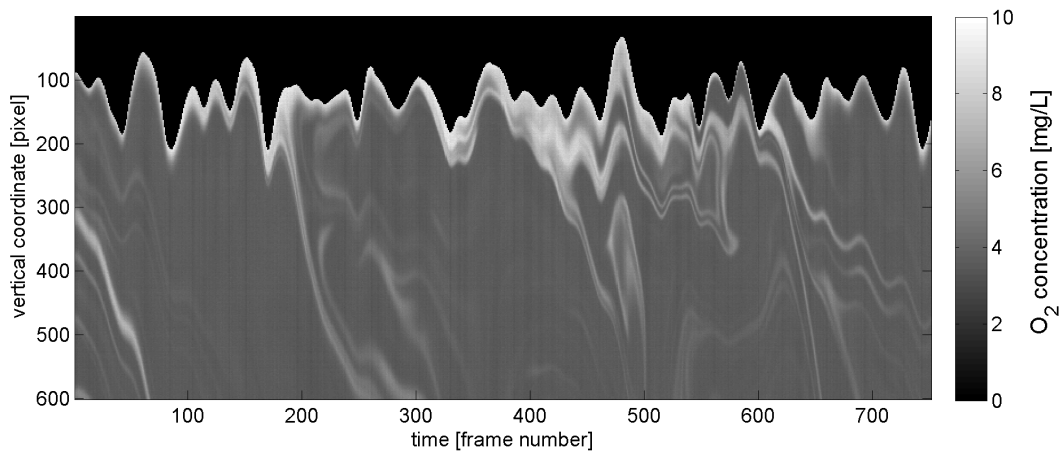


**Figure 8.13.:**  $t$ - $z$  image that was shown in Figure 8.7(b) with indicated water surface. The gray values for all positions above the water surface are set to zero.

**Step 4: Search the Surface Position of Type B** The position of the water surface at time step  $t_i$  is searched now for all pixels of type B in the range  $[z_0(t_{i+1}) - \delta_z, z_0(t_{i+1}) + \delta_z]$ , by selecting the position of the pixel with the highest  $O_2$  concentration. If there is at least one pixel of type B in the range, the surface position is identified and saved as the surface position  $z_0(t_i)$ . The algorithm proceeds one step backwards in time ( $i = i - 1$ ) and the routine passes on to the beginning of step 3. If no surface can be identified, the profile index is tagged to be disregarded in the later analysis. In the successive iteration step, the last successful detected surface position is used.

Figure 8.12 shows the detected surface positions for the same  $t$ - $z$  image as shown in Figure 8.10. It is seen that the surface position of type B is only needed in the fastest moving section of the water surface in vertical direction. Figure 8.13 shows the  $t$ - $z$  image depicted in Figure 8.7(b) with the water surface indicated, by setting the  $O_2$  concentration above the water surface to zero.

### 8.2.3. Calculating Mean Concentration Profiles

All gas transfer models considered in this thesis and interesting quantities like the local transfer velocity  $k_{\text{LIF}}$  are based on mean concentration profiles. These are obtained by averaging the  $t$ - $z$  images along the time coordinate.

In the presence of waves, the scale of the wave amplitude is larger than the thickness  $\delta_{\text{mbl}}$  of the mass boundary layer, as will be shown in Section 9.2. Therefore, the surface elevation due to waves has to be taken into account when concentration profiles are averaged. This is done by transforming the vertical coordinate of the  $\text{O}_2$  concentration profiles to the relative depth to the water surface. The correct coordinate system to measure the water depth under a wavy surface would be a curvilinear coordinate system. The approximation of using the relative depth to the water surface is justified here.

The curvilinear coordinate system follows the temporal and spatial development of the water surface. The transformation of the coordinate system from the laboratory system to the wave following system was proposed by Hsu et al. [1981]. They perform a vertical transformation of the form

$$z = z^* + f(z^*) \cdot \eta(t), \quad (8.8)$$

where  $z^*$  is the depth in the transformed coordinate system ( $z^* = 0$  at the water surface),  $\eta$  is the surface elevation, and  $f(z^*)$  is a function, which decreases monotonically from 1 at the water surface ( $z^* = 0$ ) to 0 at the boundary of the flow (the bottom of the water tank). A further approximation is done, that the surface elevations are small compared to the water depth. This leads to the simplified vertical transformation [Troitskaya et al., 2011]

$$z^* = z - \eta(t). \quad (8.9)$$

In this approximation,  $z^*$  is the relative depth to the water surface. Figure 8.14 shows a  $t$ - $z$  image in the transformed coordinate system, where the vertical coordinate is represented in the relative depth to the water surface.

One has to account for the laser beam being tilted by an angle  $\alpha = 16.5$  degree (see Figure 4.4). Therefore, a measured distance in the image is converted into a depth  $z$  by a factor of  $\cos \alpha$ . Accordingly, the vertical transformation of the data used in this study is

$$z^* = (z - \eta(t)) \cdot \cos \alpha. \quad (8.10)$$

In the following,  $z$  will be used for the relative depth to the water surface instead of  $z^*$  for simplicity.

The mean concentration profile

$$\bar{c}(z) = \frac{1}{N} \cdot \sum_{i=1}^N c(z, t_i) \quad (8.11)$$

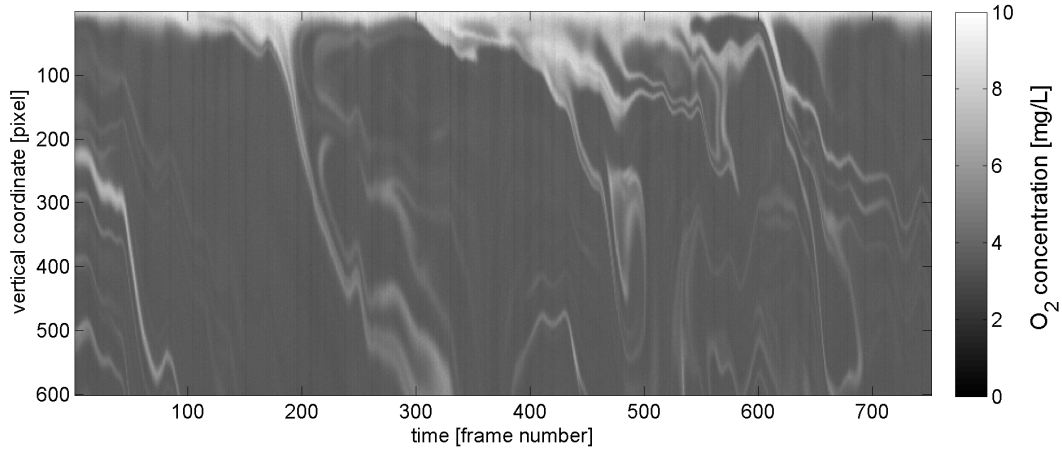


**Figure 8.14.:** Same  $t$ - $z$  image as shown in Figure 8.13 in the transformed coordinate system. The gray values in the image present  $O_2$  concentrations in units of  $\text{mg L}^{-1}$ .

is calculated from vertically transformed single profiles, where  $N$  is the number of frames recorded at a given wind speed and fetch, namely 5 000 or 15 000, depending on the data set (see Section 7.3.1). Profiles for which the surface could not be detected are excluded from averaging.

#### 8.2.4. Determination of the Boundary Layer Thickness

The thickness of the mass boundary layer  $\delta_{\text{mbl}}$  is defined by equation (2.21)

$$\delta_{\text{mbl}} = \frac{\Delta c}{-\left. \frac{\partial \bar{c}(z)}{\partial z} \right|_{z=0}}, \quad (8.12)$$

with the concentration difference  $\Delta c$  between the water surface and the water bulk. The derivative of the mean concentration profile at the water surface  $\left. \frac{\partial \bar{c}(z)}{\partial z} \right|_{z=0}$  and the concentration difference  $\Delta c$  are determined from mean concentration profiles  $\bar{c}(z)$ . One has to distinguish between two different approaches to determine the thickness  $\delta_{\text{mbl}}$  of the mass boundary layer.

If the thickness of the mass boundary layer  $\delta_{\text{mbl}}$  is significantly bigger than the optical resolution of the camera lens, the direct application of definition (8.12) provides a good estimate of  $\delta_{\text{mbl}}$ . The derivative  $\left. \frac{\partial \bar{c}(z)}{\partial z} \right|_{z=0}$  is obtained by a linear fit in the steepest region of the concentration profile  $\bar{c}$ , depicted as a green line in Figure 8.15(a). The so-called tangent method is reasonable in the shown example because the mass boundary layer is well resolved and the linear fit is performed in a region containing more than 150 data points. A constant function is fitted to the concentration profile in the bulk of the water below a depth, where the concentration  $\bar{c}(z)$  assumes a constant value (see the blue line in Figure 8.15(a)). The thickness of the mass boundary layer  $\delta_{\text{mbl}}$  is the depth where the two fit functions intersect. The tangent method yields a boundary layer thickness  $\delta_{\text{mbl}}$  for the case of a thickness  $\delta_{\text{mbl}}$  much greater than the resolution of the optical system without using a model prediction.

When the linear region of the concentration profile  $\bar{c}(z)$  at the water surface comprises only a

## 8. Data Processing

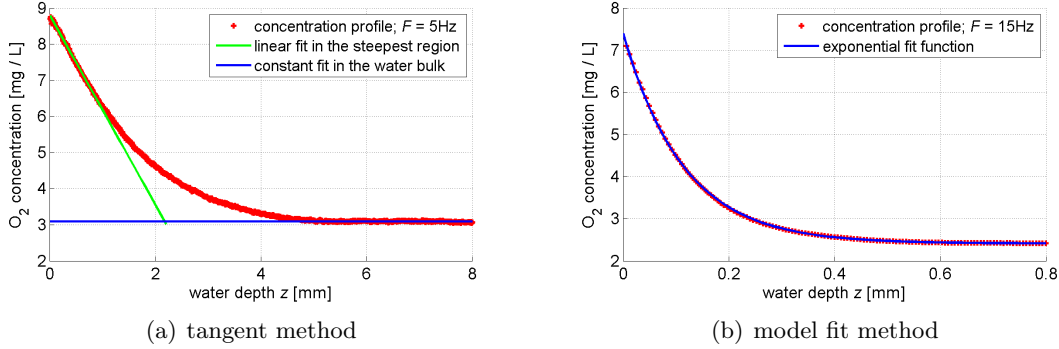


**Figure 8.15.:** Two methods to calculate the thickness of the mass boundary layer  $\delta_{\text{mbl}}$  at different wind speeds.

few data points, as shown in Figure 8.15(b), the determination of the derivative  $\left. \frac{\partial \bar{c}(z)}{\partial z} \right|_{z=0}$  from a tangent fit is defective. Instead, a model function that describes the form of the concentration profile is used. Possible functions are the four predicted functions by the small eddy model and the surface renewal model for a rigid and a free interface (see Sections 2.2.2 and 2.2.3). A benefit of the model fit method is that the data of the complete concentration profile  $\bar{c}(z)$  is used compared to using only the linear sections for the tangent method. Figure 8.15(b) shows a concentration profile with an exponential fit function, which is the model prediction of the surface renewal model for a Schmidt number exponent  $n$  of 0.5.

Both methods are needed for their individual range where they are most applicable. In Section 9.4.1, the predicted functions of the surface renewal model and the small eddy model will be tested with the measured concentration profiles. The thickness of the mass boundary layer  $\delta_{\text{mbl}}$  in Section 9.6.1 is calculated by using the model that describes the data best.

**Calculation of the Local Transfer Velocity** The local transfer velocity  $k_{\text{LIF}}$  is calculated from the mass boundary layer thickness  $\delta_{\text{mbl}}$  for a measured image sequence using equation (2.23)

$$k = \frac{D}{\delta_{\text{mbl}}}, \quad (8.13)$$

where  $D$  is the diffusion constant of  $\text{O}_2$ . The value of  $D$  is  $2.1 \cdot 10^{-5} \text{ cm}^2 \text{ s}^{-1}$  at a temperature of  $25^\circ\text{C}$  [Cussler, 2009]. To obtain the value of the diffusion constant  $D$  at  $23^\circ\text{C}$  (the temperature of the water during the experiments), a proportionality of  $D$  to the temperature is assumed, as suggested by the Stokes-Einstein equation [Cussler, 2009], yielding:

$$D(23^\circ\text{C}) = 2.086 \cdot 10^{-5} \text{ cm}^2 \text{ s}^{-1}. \quad (8.14)$$

This value differs less than 0.7% from the diffusion constant at  $25^\circ\text{C}$ . This deviation is certainly below the uncertainty in  $D(25^\circ\text{C})$  itself, which justifies the approximation of a linear temperature dependence.

### 8.3. Processing of the Bulk Measurements

The bulk measurements were performed in order to determine the transfer velocity  $k_b$  integrated over fetch using a mass balance method (see Section 3.3). The  $O_2$  concentration in the water bulk was measured every 5 seconds, as described in Section 7.3.2. A typical dataset is shown in Figure 8.16. By fitting equation (3.16)

$$c(t) = \alpha \cdot c_a + (c_0 - \alpha \cdot c_a) \cdot \exp\left(-\frac{k_b}{h_{\text{eff}}} \cdot t\right) \quad (8.15)$$

to the measured data, three parameters are obtained: the initial  $O_2$  concentration  $c_0$ , the  $O_2$  concentration in equilibrium with air  $\alpha \cdot c_a$ , and the quotient of the transfer velocity and the effective height  $\frac{k_b}{h_{\text{eff}}}$ . The effective height  $h_{\text{eff}} = \frac{V}{A}$  of the water is calculated from the total water volume and the water surface area  $A$ . The values given in Section 4.1.1 yield an effective height  $h_{\text{eff}}$  of 8.71 cm. The result of the bulk transfer velocities  $k_b$  is shown in Section 9.6.2.

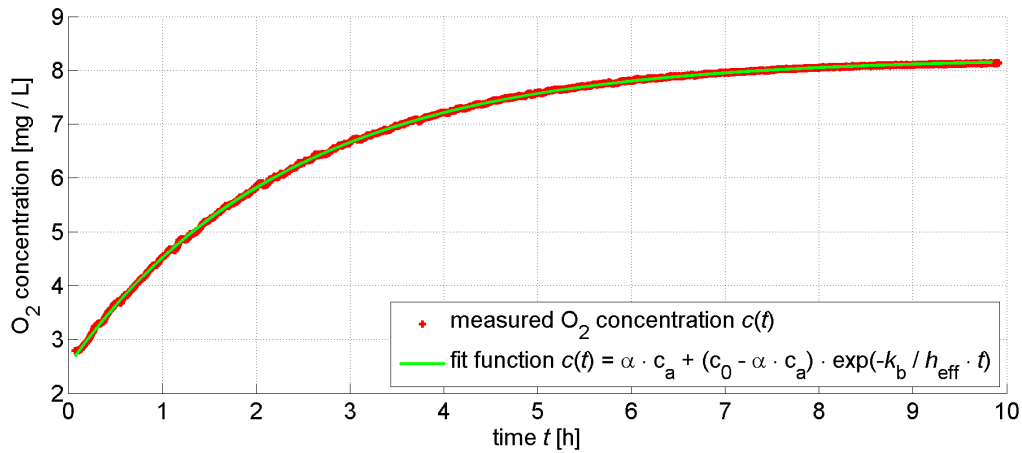


**Figure 8.16.:** Temporal development of the  $O_2$  concentration in the water bulk during an invasion experiment at a wind speed  $u_0$  of 2.8 m/s. The  $O_2$  concentration in the water was lowered to about  $2.8 \text{ mg L}^{-1}$  before the measurement was started. The equilibrium with the  $O_2$  concentration in the air was reached after about 10 hours.



## 9. Results

This section presents the results regarding gas and momentum transfer at the wind-driven air-water interface. Results concerning the oxygen quenching effect were presented in Section 5.2.2.

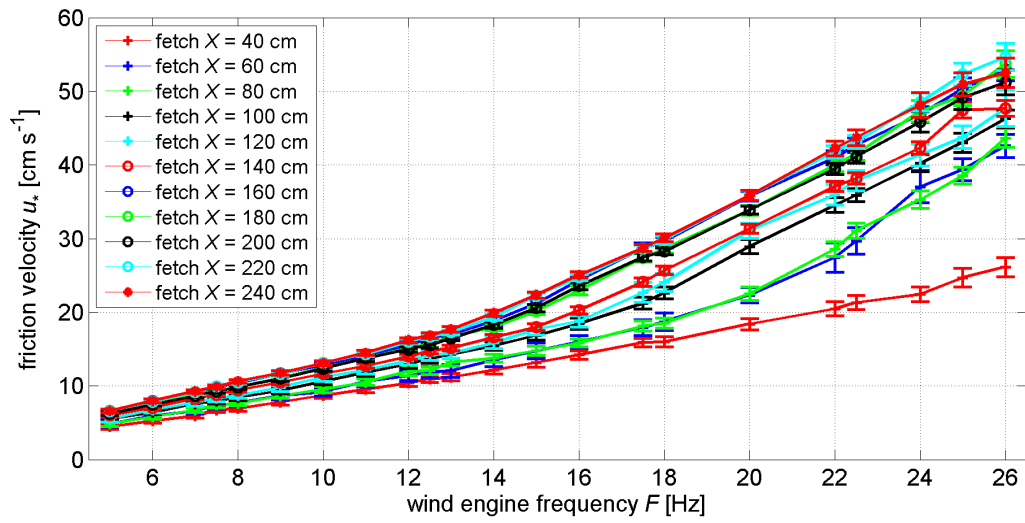
Section 9.1 presents the results from the wind profile measurements and shows the wind and fetch dependence of the friction velocity. In Section 8.2, the steps were presented that lead from raw camera pictures to  $t$ - $z$  images, showing the temporal development of oxygen ( $\text{O}_2$ ) concentration profiles, and further to mean  $\text{O}_2$  concentration profiles, the aqueous mass boundary layer thickness  $\delta_{\text{mbl}}$ , and the local transfer velocity  $k$ . Here, the results of systematic measurements performed at various fetch and wind speed combinations are presented in the order introduced in the flowchart in Figure 8.4. Before going to the detailed data analysis, a few exemplifying  $t$ - $z$  images are shown in Section 9.2 to illustrate the transfer process of  $\text{O}_2$  below the wind-driven water surface. Section 9.3 presents results of the surface detection algorithm. Mean  $\text{O}_2$  concentration profiles for a flat and wavy interface are presented and compared to models in Section 9.4. As a further result, depth-dependent fluctuations in the  $\text{O}_2$  concentration  $c'$  are presented in Section 9.5. From the mean  $\text{O}_2$  concentration profiles, transfer velocities at various fetch and wind speed combinations are calculated in Section 9.6. These transfer velocities are compared with results from mass balance measurements (Section 9.6.2). In Section 9.6.3, parametrizations of the measured transfer velocities  $k_{\text{LIF}}$  with the friction velocity  $u_*$ , the mean square slope  $\langle s^2 \rangle$ , and the wind speed  $u_0$  are presented.

### 9.1. Wind and Fetch Dependence of the Friction Velocity

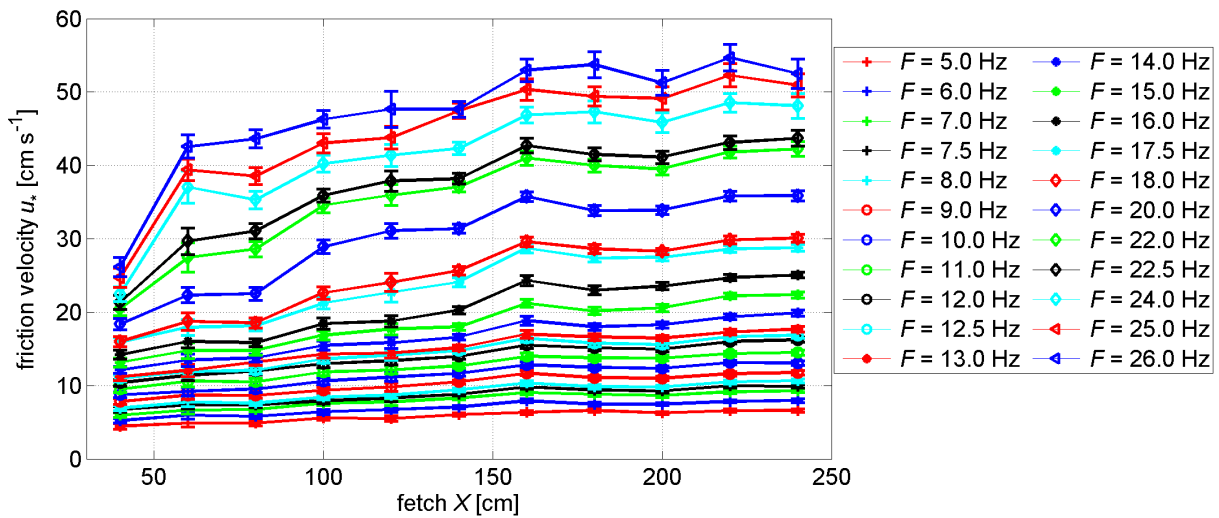
The friction velocity  $u_*$  is obtained from wind profiles, as presented in Section 8.1.2. The results for the friction velocity  $u_*$  with respect to wind engine frequency  $F$  and fetch  $X$  are shown in Figure 9.1(a) and Figure 9.1(b), respectively. Figure 9.1(b) indicates a rising friction velocity  $u_*$  with fetch. A fetch dependent friction velocity  $u_*$  was also observed by other authors (e.g. [Caulliez et al., 2008]). This effect can be explained with increasing mean square slope with fetch as the wave measurements in Section 7.2.2 show. Once the wave field is fully developed, the friction velocity  $u_*$  reaches an equilibrium value.

It is obvious that the determined values of the friction velocity  $u_*$  are defective because the values of  $u_*$  show fluctuations. To parametrize the transfer velocities  $k_{\text{LIF}}$  with the friction velocity in Section 9.6.3, a function describing  $u_*(F, X)$  is needed. To obtain a meaningful relation between the friction velocity  $u_*$  and the parameters  $X$  and  $F$ , the values have to be

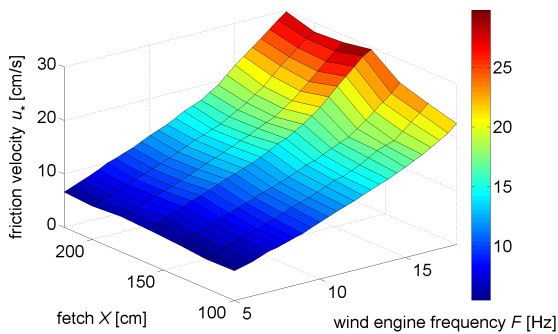
9. Results



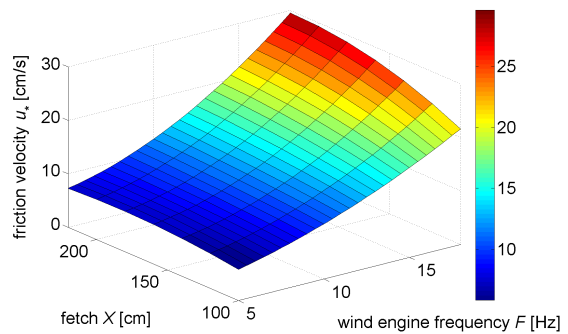
(a) Friction velocity  $u_*$  with respect to wind engine frequency  $F$  for fetch  $X$  between 40 cm and 240 cm.



(b) Friction velocity  $u_*$  with respect to fetch  $X$  for wind engine frequencies  $F$  between 5 Hz and 26 Hz.



(c) measured values of  $u_*$



(d) fitted values of  $u_*$

**Figure 9.1.:** Overview of the determined values of the friction velocity  $u_*$  with respect to wind engine frequency  $F$  and fetch  $X$ .

smoothed. To smooth the data, polynomials of second order were fitted to the data in both dimensions of fetch  $X$  and wind engine frequency  $F$ . The fit is only performed in the range  $5 \text{ Hz} < F < 17.5 \text{ Hz}$  and  $100 \text{ cm} < X < 220 \text{ cm}$ , where local transfer velocities were obtained (see Table 9.3). A comparison with the determined values for the friction velocity and the fitted values is shown in Figures 9.1(c) and 9.1(d), respectively.

## 9.2. Oxygen Concentration Images

Examples of the temporal development of  $\text{O}_2$  concentration profiles for different wind speeds, presented as images showing the  $\text{O}_2$  concentration with respect to depth and time (the so-called  $t$ - $z$  pictures), are shown in this section. Figure 9.3 displays the  $\text{O}_2$  concentrations in gray values with a limited range from  $0 \text{ mg L}^{-1}$  to  $10 \text{ mg L}^{-1}$ , as indicated by the colorbar. The parts in the images above the water surface are set to a gray value of zero for the images where the water surface was detected automatically. For comparison, rendered images of the wave field<sup>1</sup> at comparable conditions are shown in Figure 9.3. For the visualization of the wave field, the WaveVis rendering software, described in [Wanner, 2010], was used. In the following five paragraphs, a distinction is made for different wave field and wind speed conditions with focus on the limits of the LIF measurement technique. Moreover, these examples already provide insights into the processes which control the gas invasion for the different turbulence conditions.

**Flat Water Surface** Figure 9.2(a) shows a  $t$ - $z$  picture at a wind speed  $u_0$  of  $1.3 \text{ m s}^{-1}$  at a fetch of 200 cm. An image of the wave field is not shown here because the surface is absolutely flat. The thickness  $\delta_{\text{mbl}}$  of the mass boundary layer is about 2 mm. No turbulent structures can be observed in the aqueous mass boundary layer. At intervals of 500 ms, we see vertical stripes in the  $t$ - $z$  picture. This effect is due to a problem of the camera (see Section A.4.2).

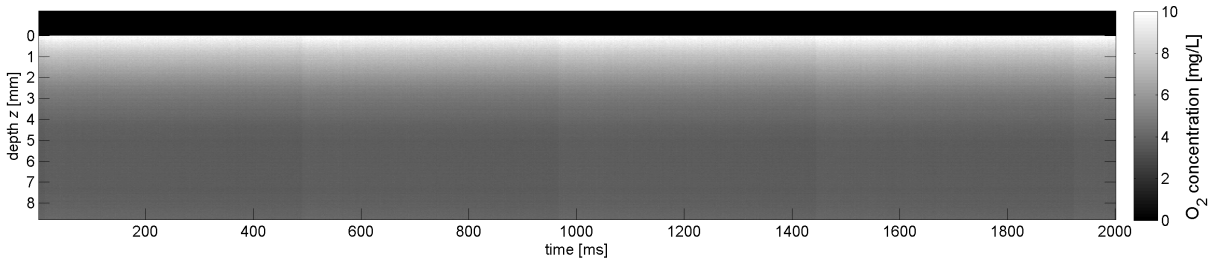
**First Undulation of the Water Surface** Figure 9.2(b) shows a  $t$ - $z$  picture at a wind speed  $u_0$  of  $2.8 \text{ m s}^{-1}$  and a fetch of 220 cm. Undulations of the water surface in the range of  $\pm 0.2 \text{ mm}$  can be observed due to the high optical resolution of  $6.2 \mu\text{m}$ , whereas in the images of the wave field (Figure 9.3(a)) these small undulations are hardly observable. In comparison with the  $t$ - $z$  image at the wind speed of  $1.3 \text{ m s}^{-1}$ , turbulent structures are present, which lead to a high contrast in the images. The invasion process of  $\text{O}_2$  is visible as zones with enriched  $\text{O}_2$  concentration being transported into deeper zones of the water.

**Capillary Waves with Small Amplitude** The Figures 9.2(c) and 9.3(b) were taken at a wind speed of  $4.3 \text{ m s}^{-1}$  and at a fetch of 220 cm. In the  $t$ - $z$  image, capillary waves<sup>2</sup> with a frequency of about 50 Hz are visible. The algorithm to detect the water surface (Section 8.2.2) is still

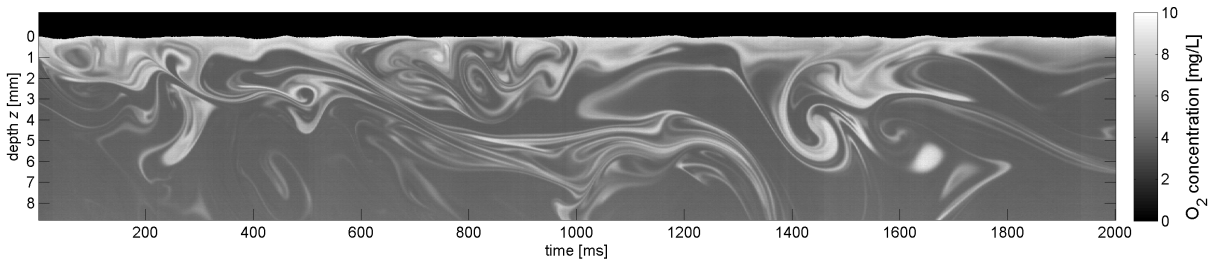
<sup>1</sup>The wave field was measured with the ISG, see Section 7.2.2.

<sup>2</sup>Capillary waves are named after the restoring force to reestablish the equilibrium state [Kinsman, 1965].

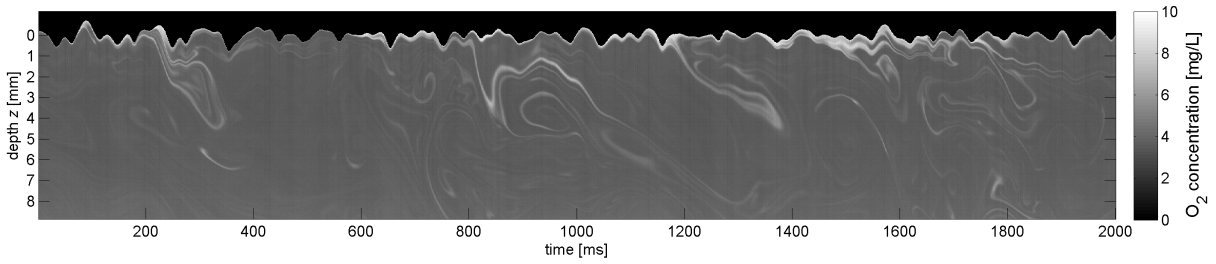
## 9. Results



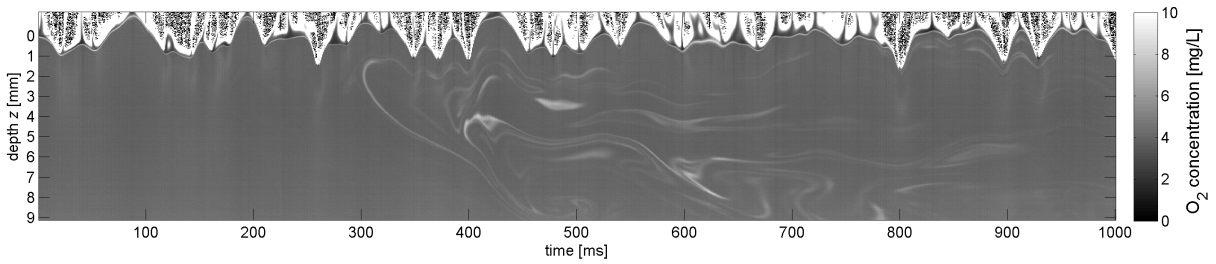
(a) wind speed  $u_0 = 1.3 \text{ m s}^{-1}$ ;  $u_* = 7.3 \text{ cm s}^{-1}$ ;  $F = 5 \text{ Hz}$ ; fetch  $X = 220 \text{ cm}$ ; frame rate 500 Hz



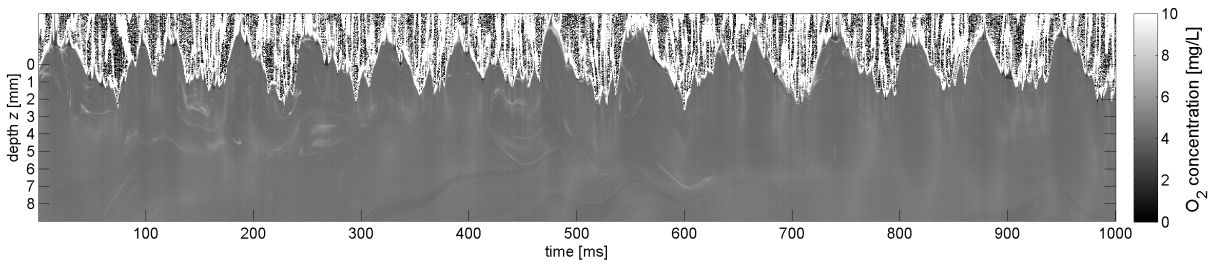
(b) wind speed  $u_0 = 2.8 \text{ m s}^{-1}$ ;  $u_* = 12.5 \text{ cm s}^{-1}$ ;  $F = 10 \text{ Hz}$ ; fetch  $X = 220 \text{ cm}$ ; frame rate 500 Hz



(c) wind speed  $u_0 = 4.3 \text{ m s}^{-1}$ ;  $u_* = 22.2 \text{ cm s}^{-1}$ ;  $F = 15 \text{ Hz}$ ; fetch  $X = 220 \text{ cm}$ ; frame rate 750 Hz



(d) wind speed  $u_0 = 5.0 \text{ m s}^{-1}$ ;  $u_* = 28.2 \text{ cm s}^{-1}$ ;  $F = 17.5 \text{ Hz}$ ; fetch  $X = 220 \text{ cm}$ ; frame rate 1200 Hz



(e) wind speed  $u_0 = 7.5 \text{ m s}^{-1}$ ;  $u_* = 48.1 \text{ cm s}^{-1}$ ;  $F = 26 \text{ Hz}$ ; fetch  $X = 140 \text{ cm}$ ; frame rate 1900 Hz

**Figure 9.2.:** Five  $t$ - $z$  pictures showing the  $\text{O}_2$  concentration in gray values between  $0 \text{ mg L}^{-1}$  and  $10 \text{ mg L}^{-1}$  with respect to time and water depth  $z$  at different wind speeds.

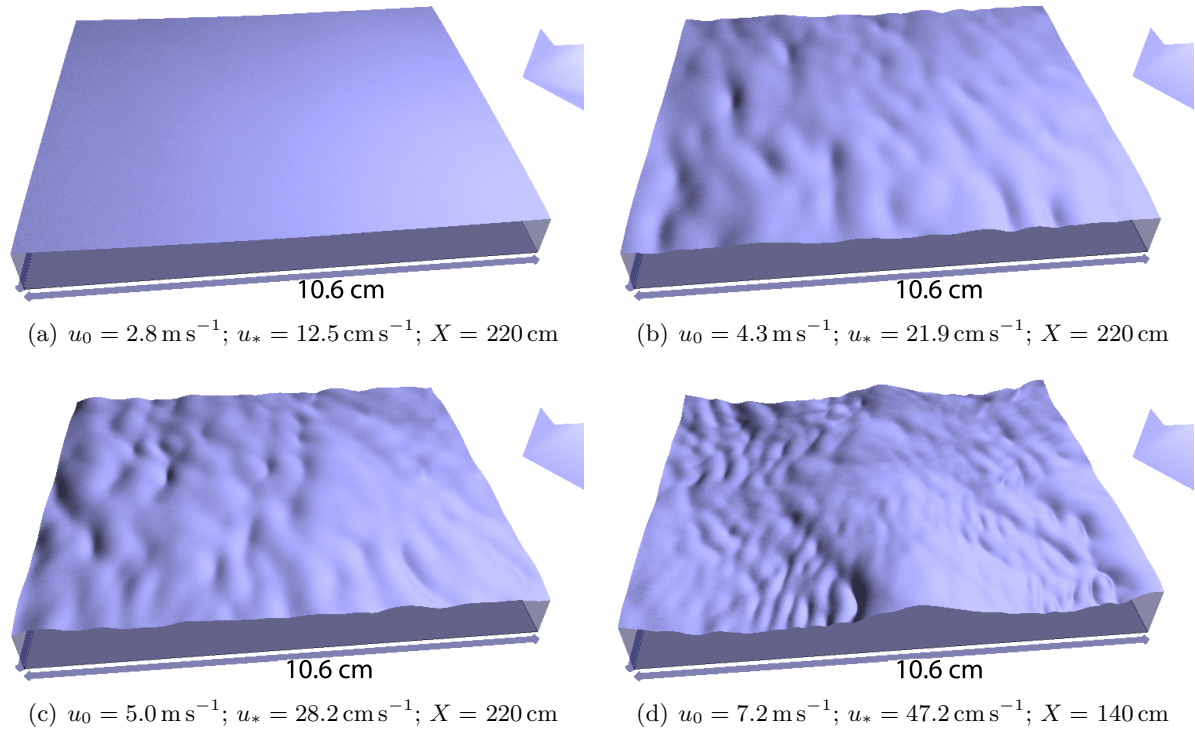


**Figure 9.3.:** Images of the wave field, measured with the ISG (Section 7.2.2) and visualized with the WaveVis rendering software [Rocholz et al., 2011]. Wind direction from right to the left, as the arrow indicates. The field of view is approximately  $10.6 \times 7.9 \text{ cm}^2$ .

working for these conditions, since the maximum slope of the water surface is small enough to see a mirror image in each single profile (Section 8.2.2). The layer close to the surface which is enriched with  $\text{O}_2$  is visible as a bright line right beneath the water surface. Its thickness is much smaller compared to the  $t$ - $z$  pictures at lower wind speed, namely about  $60 \mu\text{m}$ , as we will see in Section 9.6.1. Oxygen is transported from the air into the water in jet-like events, emerging at the water surface. The wave visualization picture shows the existence of capillary ripples, see Figure 9.3(b).

**Capillary Waves - No Surface Detection** When the surface slope exceeds the limits of the measuring setup (Section 4.2.1), no mirror image of the water-sided  $\text{O}_2$  image is seen for most of the time steps and the algorithm to detect the surface position fails. Even a manual selection of the surface position is not possible in the steep part of a wave. For  $t$ - $z$  pictures of that kind, no systematic data evaluation was performed, as the water surface has to be known to calculate the water depth  $z^*$  in transformed coordinates relative to the water surface (Section 8.2.3). As an example for this case, Figure 9.2(d) shows a  $t$ - $z$  image taken at the wind speed of  $5 \text{ m s}^{-1}$  and at a fetch of 220 cm. Above the water surface, we see mostly white regions, resulting from a low luminescence signal that was converted with equation (8.7) to an overestimated  $\text{O}_2$  concentration. Figure 9.3(c) shows the corresponding wave visualization.

## 9. Results

**Table 9.1.:** The check marks indicate the conditions of wind speed (in units of the wind engine frequency  $F$ ) and fetch  $X$ , where data was taken and the surface detection algorithm worked successfully.

$F$ [Hz]	5	6	7	8	9	10	11	12	13	14	15	16	17	17.5
fetch $X = 100$ cm	✓					✓					✓			✓
fetch $X = 120$ cm											✓			
fetch $X = 140$ cm	✓	✓	✓	✓	✓	✓	✓	✓	✓	✓	✓	✓	✓	
fetch $X = 160$ cm											✓			
fetch $X = 200$ cm											✓			
fetch $X = 220$ cm	✓					✓					✓			

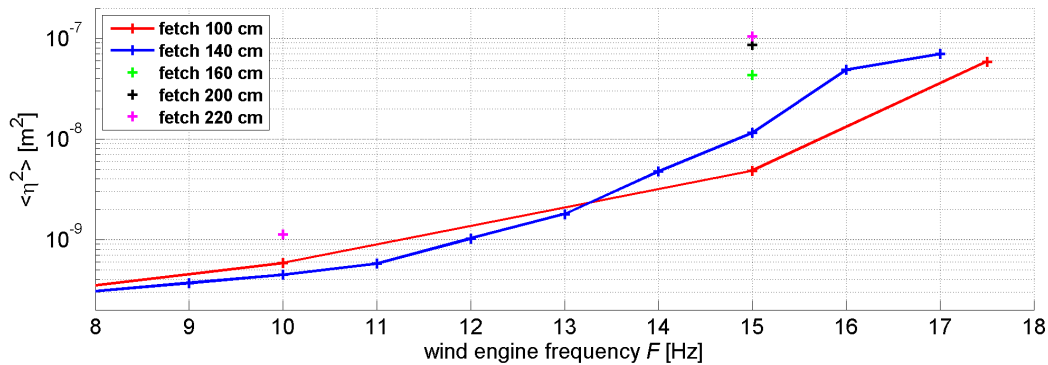


**Figure 9.4.:** Mean squared wave height  $\langle \eta^2 \rangle$  with respect to wind engine frequency  $F$  for different fetch  $X$ .

**Gravity-Capillary Waves** At a wind speed of  $7.5 \text{ m s}^{-1}$  and a fetch of 140 cm, the  $t$ - $z$  image in Figure 9.2(e) shows a wave amplitude of about 2 mm with a high range of surface slopes that makes the detection of the water surface impossible. This case can not be used for the further data analysis, as the previous example. We can see gravity-capillary waves with a frequency on the order of 10 Hz in the transition region between gravity and capillary waves [Thorpe, 2009, p. 3-11]. Figure 9.3(d) shows a gravity-capillary wave with parasitic capillary waves on the forward face of the wave.

### 9.3. Results of the Surface Detection Algorithm

The algorithm to detect the position of the water surface in the images obtained from the LIF measurements is described in Section 8.2.2. As mentioned in that section, the algorithm works only for moderately wave slopes. Table 9.1 shows all measured conditions of wind speed and fetch, where measurements were performed and the surface detection algorithm was successful. All the results from the LIF measurements that are shown in the following sections of this chapter originate from data measured at the indicated conditions. For a fetch  $X$  of 100 cm, the surface could be detected up to a wind engine frequency of 17.5 Hz. With increasing fetch, the limit dropped down to a wind engine frequency  $F$  of 15 Hz, as the wave amplitude and mean square slope  $\langle s^2 \rangle$  grow with fetch. The mean squared wave height  $\langle \eta^2 \rangle$  was calculated out of the detected surface positions for each condition that is marked in Table 9.1. Figure 9.4 shows

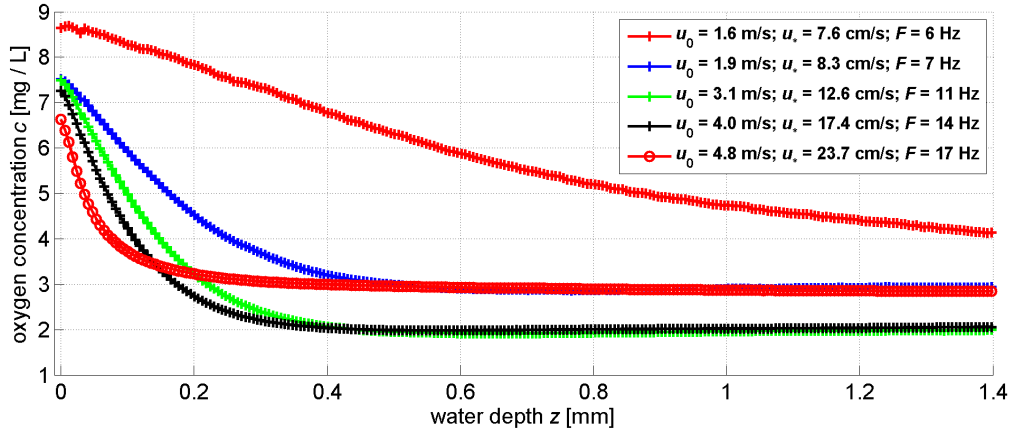


**Figure 9.5.:** Measured mean oxygen concentration  $c$  with respect to water depth  $z$ . The values were obtained by averaging 50000 single concentration profiles.

the results of the of the mean squared wave heights. The mean squared wave height  $\langle \eta^2 \rangle$  rises monotonically with wind speed, as the measurement at the fetch of 140 cm shows. The data at the wind engine frequency of 15 Hz shows a rising mean squared wave height  $\langle \eta^2 \rangle$  with fetch.

Based on the results in Figure 9.4 and on the results of the wave measurements in Section 7.2.2, the transition from a completely smooth to a rough water surface at a fetch of 140 cm occurs for wind engine frequencies in the region  $10 \text{ Hz} < F < 15 \text{ Hz}$ . That statement is supported by the  $t$ - $z$  images in Figure 9.2. The classification of each measured condition to either a smooth or a wavy water surface is important when the data is compared with the surface renewal model and the small eddy model in the next section to distinguish between the hydrodynamic boundary conditions of a rigid interface and a free interface.

## 9.4. Mean Oxygen Concentration Profiles

This section presents mean vertical profiles of the  $\text{O}_2$  concentration and compares the results with the surface renewal model and the small eddy model. The used method to obtain mean  $\text{O}_2$  concentration profiles was presented in Section 8.2.3. Mean concentration profiles were calculated for each condition of the systematic measurements, where the water surface could be detected (see Table 9.1). The mean profiles shown in this section were all measured at a fetch of 140 cm, as measurements with fine increments in the wind speed were only taken at this position.

Figure 9.5 shows mean  $\text{O}_2$  concentration profiles that were obtained from measurements at a fetch of 140 cm, to present the impact of wind speed on concentration profiles. The resolution in depth  $z$  is about  $5.9 \mu\text{m}$ , resulting from the optical resolution of  $6.2 \mu\text{m}$  (see equation (6.1)) and the angle  $\alpha = 16.5^\circ$  (see Figure 4.4) of the tilted laser beam. This resolution is a significant improvement to previous studies of measurements of concentration profiles at a wavy water surface. Münsterer and Jähne [1998] achieved a resolution of  $18 \mu\text{m}$ . The resolution in the study of Falkenroth [2007] was  $25 \mu\text{m}$ . The concentration profiles show a decay from the value  $c_s$  at

## 9. Results

the water surface to the value  $c_b$  in higher water depths (the water bulk). The absolute value of the derivative of the concentration at the water surface with respect to the depth  $z$  grows with increasing wind speed. This observation is in agreement with expectations as the transfer velocity  $k$  and thus the flux density  $j$  grows with wind speed, leading to an increased gradient at the water surface due to equation (2.22)

$$j_c = -D \left. \frac{\partial \bar{c}}{\partial z} \right|_{z=0}. \quad (9.1)$$

For a wind speed  $u_0$  of  $1.6 \text{ m s}^{-1}$  (red crosses), the  $\text{O}_2$  concentration at the water surface  $c_s$  is higher compared to the other presented profiles. The reason is that the flow velocity of the water at this wind speed is so low that a fluid particle spends more time in the laser region than the time interval  $\tau_{\text{off}}$  between two successive laser pulses, as described in Section 3.1.2. In conclusion, equation (3.2)

$$\tau_{\text{off}} > \frac{d}{v_1}, \quad (9.2)$$

with the laser beam diameter  $d$  and the local fluid velocity  $v_1$ , is not satisfied locally. This leads to a lower photon flux  $\Phi$  compared to the case of higher flow velocity in which equation (9.2) would be satisfied. According to equation (3.1)

$$c = \left( \frac{\Phi_0}{\Phi} - 1 \right) \cdot \frac{1}{K_{\text{SV}} \cdot \epsilon_{\text{D}}}, \quad (9.3)$$

the resulting  $\text{O}_2$  concentration is overestimated. All concentration profiles, measured at a wind speed  $u_0$  between  $1.9 \text{ m s}^{-1}$  and  $4.5 \text{ m s}^{-1}$  including the ones not shown in the figure coincide at the water surface. This indicates that the flow velocity of the water is large enough to satisfy equation (9.2). The concentration  $c_b$  in the water bulk differs for each profile as the water was degassed before each measurement leading to a non-reproducible  $\text{O}_2$  concentration in the water. For the concentration profile measured at a wind speed  $u_0$  of  $4.8 \text{ m s}^{-1}$  (red circles), the concentration  $c_s$  at the water surface is lower than for the other wind speeds. This is due to an error in the surface detection that occurs at high wave slopes, as explained in Section 8.2.2.

### 9.4.1. Fit of the Models to the Data

A quantitative analysis of how well the surface renewal model and the small eddy model describe the data is given in this paragraph. The test was done by fitting the four functions predicted by the two models with boundary conditions of a rigid wall and a free interface (see equations (2.53) to (2.59)) to the mean concentration profiles. The fit was performed with the unscaled concentration profiles to make no a priori assumptions about the parameters  $\delta_{\text{mbl}}$ ,  $c_s$ , and  $c_b$ . The model functions were converted from the dimensionless concentration  $c_+$  and depth  $z_+$  to the dimensional quantities  $c$  and  $z$ . The free fit parameters were  $c_s$ ,  $c_b$ , and  $\delta_{\text{mbl}}$ . The range of the fitting procedure was from depth  $z = 0$  to  $z = 4 \delta_{\text{mbl}}$ , using the value of  $\delta_{\text{mbl}}$  determined

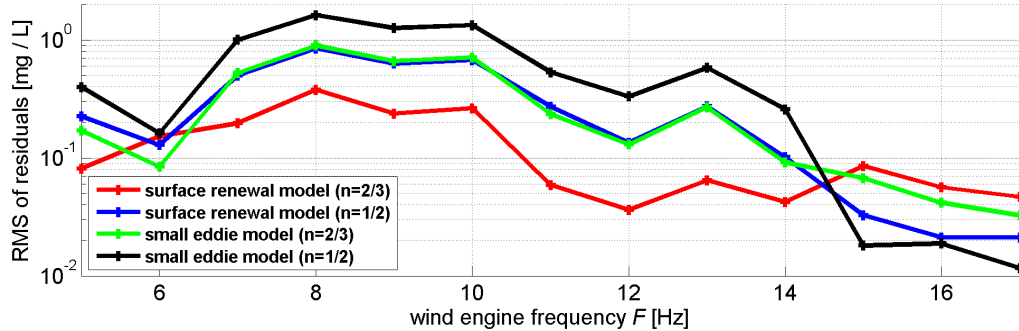


**Figure 9.6.:** RMS values of the residuals from the four fit functions (see legend) with respect to the frequency of the wind engine  $F$  at which the dataset was taken.

by the tangent method, as explained in Section 8.2.4. The root mean square (RMS) value of the residuals was used to determine which model describes the data best. Figure 9.6 shows the RMS of the residuals of the four functions and the concentration profiles measured at a fetch of 140 cm.

Up to a wind engine frequency  $F$  of 14 Hz, the surface renewal model for the Schmidt number exponent  $n$  of  $2/3$  describes the data best, with one exception at 6 Hz. A transition happens from 14 Hz to 15 Hz, above which the surface renewal model for  $n = 2/3$  is the worst description of the data compared to the other models. The data from 15 Hz to 17 Hz is best described with the small eddy model for  $n = 1/2$ , followed by the surface renewal model for  $n = 1/2$ . However, the result depends on the range of the performed fit. By not taking into account the uppermost  $50 \mu\text{m}$  below the water surface, the surface renewal model for  $n = 1/2$  describes the data better than the small eddy model for  $n = 1/2$ . To interpret the data in Figure 9.6, the state of the wave field at the given wind speeds is taken into account. The transition from a completely smooth to a rough water surface at a fetch of 140 cm occurs for wind engine frequencies between  $10 \text{ Hz} < F < 15 \text{ Hz}$ , as shown in Section 9.3. Accordingly, the transition in the shape of the concentration profiles that Figure 9.6 proposes coincides with the onset of waves, what is in agreement with the predictions of the surface renewal as well as the small eddy model.

In conclusion, for a flat water surface, the measured averaged concentration profiles are best described by the surface renewal model for a rigid interface. For a wavy water surface, a determination between the surface renewal model and the small eddy model is not possible. Table 9.2 shows the obtained mass boundary layer thickness  $\delta_{\text{mbl}}$  and surface concentration  $c_s$  obtained from the fit procedures with the models. The obtained values cannot be used as a criterion to rule out one of the models for a wavy water surface because both models achieve reasonable values.

For the case of flat water surface, a similar result was achieved in the studies of Münsterer and Jähne [1998] (see Figure 1.2) and Falkenroth [2007]. They showed that the surface renewal model for  $n = 2/3$  describes their data best. To the best of the author's knowledge, only one study by Münsterer [1996] examined concentration profiles at a wavy water surface under wind-

## 9. Results

**Table 9.2.:** Results of the mass boundary layer thickness  $\delta_{\text{mbl}}$  and the surface concentration  $c_s$  obtained from the fits with the surface renewal model (SR) and the small eddy model (SE) to the mean concentration profiles. Up to wind engine frequencies  $F = 14$  Hz, the model functions for a Schmidt number exponent of  $n = 2/3$  were used to perform the fit. For  $F = 15$  Hz to  $F = 17$  Hz, the model functions for  $n = 1/2$  were taken.

$F$ [Hz]	6	7	8	9	10	11	12	13	14	15	16	17
$\delta_{\text{mbl}}$ (SE) [ $\mu\text{m}$ ]	1141	238	224	198	191	196	184	182	156	124	105	69
$\delta_{\text{mbl}}$ (SR) [ $\mu\text{m}$ ]	1123	248	231	207	200	197	186	178	156	103	82	56
$c_s$ (SE) [ $\text{mg L}^{-1}$ ]	8.8	7.7	7.7	7.7	7.8	7.6	7.4	7.5	7.4	7.1	7.1	6.7
$c_s$ (SR) [ $\text{mg L}^{-1}$ ]	8.7	7.7	7.6	7.7	7.7	7.6	7.3	7.5	7.3	7.1	7.1	6.7

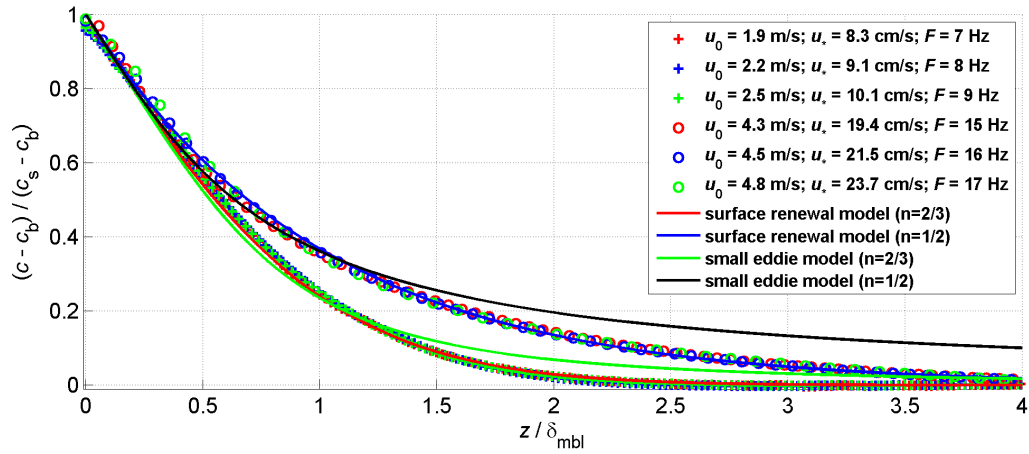
induced turbulence. In that study, a transition in the concentration profile from the surface renewal model for  $n = 2/3$  at a flat water surface to the surface renewal model for  $n = 1/2$  at a wavy water surface was found. However, a fit with the function predicted by the small eddy model was not performed in that study, as “this function is too complicated for a non-linear fitting procedure”, as they wrote. In the present study, it could be shown that the small eddy model for  $n = 1/2$  describes the profiles at a wavy water surface well, resulting in a different, yet reasonable, thickness  $\delta_{\text{mbl}}$  of the mass boundary layer. The striking agreement with the surface renewal model in the study of Münsterer [1996] is biased by the a priori scaling of the profiles by the exponential fit method, as the author himself mentions.

Oxygen concentration profiles at the air-water interface have also been measured in grid-stirred tanks in studies by Herlina and Jirka [2008] and Schulz and Janzen [2009]. A comparison with the concentration profiles obtained in this thesis is difficult due to the different method to generate the turbulence. In the study of Herlina and Jirka [2008], a good agreement with both models for  $n = 1/2$  was found, whereas Schulz and Janzen [2009] identified the best agreement with the model prediction for  $n = 2/3$ .

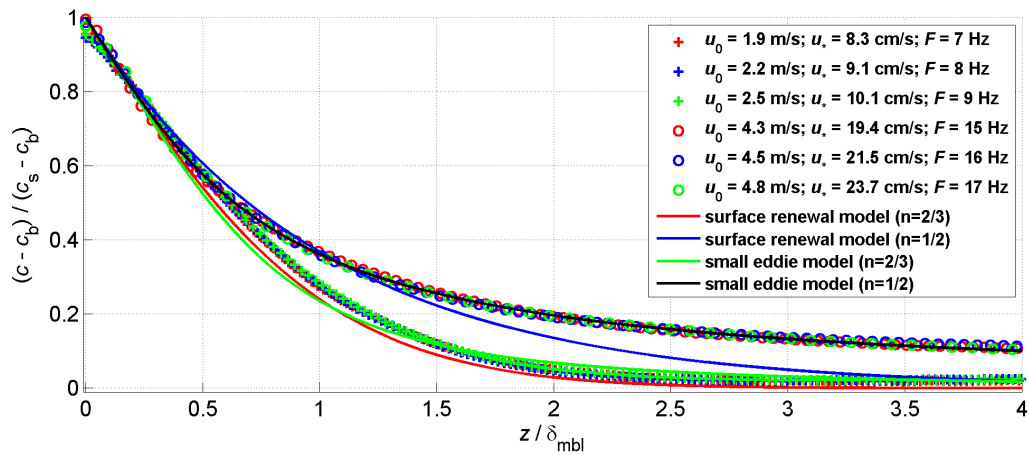
Concentration profiles in earlier studies were measured in grid-stirred tanks with oxygen microprobes by Chu and Jirka [1992], Prinos et al. [1995], and Atmane and George [2002]. The spatial resolution of the profiles obtained with this technique is about one order of magnitude lower than the resolution obtained with the non-invasive LIF technique, that was used in this thesis. Therefore, the profiles presented in this thesis are more applicable to test models by the shape of the concentration profiles.

### 9.4.2. Scaling with the Models

This section presents the averaged concentration profiles in dimensionless units. The parameters necessary for scaling ( $\delta_{\text{mbl}}$ ,  $c_s$ , and  $c_b$ ) are either obtained by fitting the surface renewal model or the small eddy model to the profiles. Depending on the state of the water surface, the predicted functions for  $n = 2/3$  or  $n = 1/2$  are fitted to the data in dimensionful units. As a result, the fit routine returns the three fit parameters  $\delta_{\text{mbl}}$ ,  $c_s$ , and  $c_b$ . This technique is more stable than the tangent method (see Section 8.2.4), as the total range of the concentration profile is considered to determine the thickness  $\delta_{\text{mbl}}$  in contrast to only a linear region near the water surface that has



(a) fit with surface renewal model



(b) fit with small eddy model

**Figure 9.7.:** Normalized mean oxygen concentration  $c_+$  with respect to the normalized depth  $z_+ = z / \delta_{mbl}$  for three wind speeds at a flat water surface and three wind speeds at a wavy water surface. The parameters for the normalization ( $\delta_{mbl}$ ,  $c_s$ , and  $c_b$ ) were obtained by fitting the functions predicted by the surface renewal model and the small eddy model to the data. The mean concentration profiles derived with the surface renewal model and the small eddy model are indicated in the plot for the two boundary conditions of a rigid interface ( $n = 2/3$ ) and a free interface ( $n = 1/2$ ).

## 9. Results

to be selected individually for each fit. Figures 9.7(a) and 9.7(b) show mean  $O_2$  concentration profiles, normalized with the parameters obtained from the fit with the surface renewal and the small eddy model functions. Three measurements at a flat water surface and three measurements at a wavy water surface are depicted. A transition in the shape of the concentration profiles is observed when the water surface changes from smooth to wavy. This is in agreement with both, the surface renewal model and the small eddy model. They both predict a change in the shape of the concentration profiles when the Schmidt number exponent  $n$  changes from  $2/3$  for a rigid interface to  $1/2$  for a free interface, as shown in Section 2.2. The figures indicate that both models, the surface renewal model and the small eddy model describe the data equally well at a wavy water surface, as long as the scaling parameters are chosen suitably.

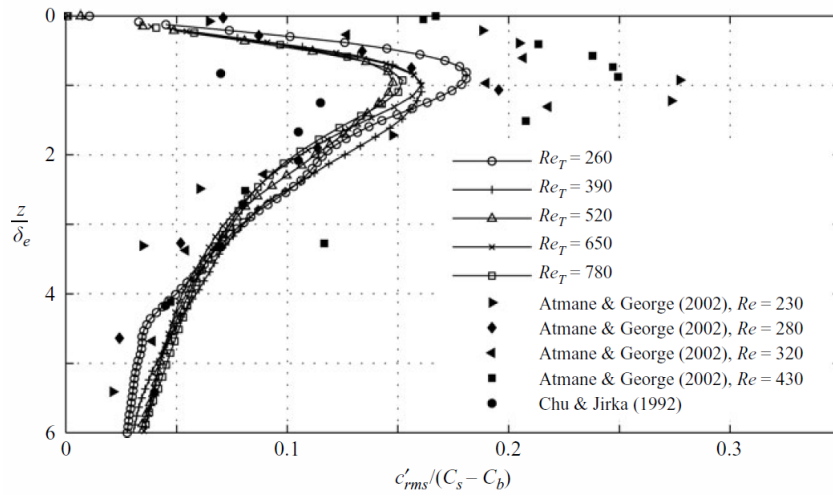
### 9.5. Fluctuation Concentration Profiles

This section presents the depth dependent root mean square (RMS)  $O_2$  concentration fluctuations  $c'$  for a smooth and a wavy water surface. The measurements give insights into interesting quantities. It is still an unresolved question if the concentration fluctuations vanish at the water surface. Figures 9.8(a) and 9.8(b) show measurements of RMS fluctuation profiles in a grid-stirred tunnel and a wind-wave tank, respectively, from previous studies by Herlina and Jirka [2008] and Münsterer [1996]. The results from the grid-stirred tank show vanishing concentration fluctuations at the water surface, whereas non-zero fluctuations were measured in the wind-wave tunnel. For a rigid air-water interface, both, the surface renewal as well as the small eddy model make the assumption of zero fluctuations at the water surface (see Sections 2.2.2 and 2.2.3). For a free interface, there are non-vanishing fluctuations at the surface according to the surface renewal model, while the small eddy model still assumes vanishing fluctuations. All recent measurements agree, that the RMS concentration fluctuations show a distinct peak. Aspects to examine are the depth and the value of the peak. In Section 2.2.4, a model was developed that predicts concentration fluctuations with respect to the water depth based on the assumptions of the surface renewal model for a rigid interface. The fluctuation concentration profile is obtained by numerical integration of equation (2.68)

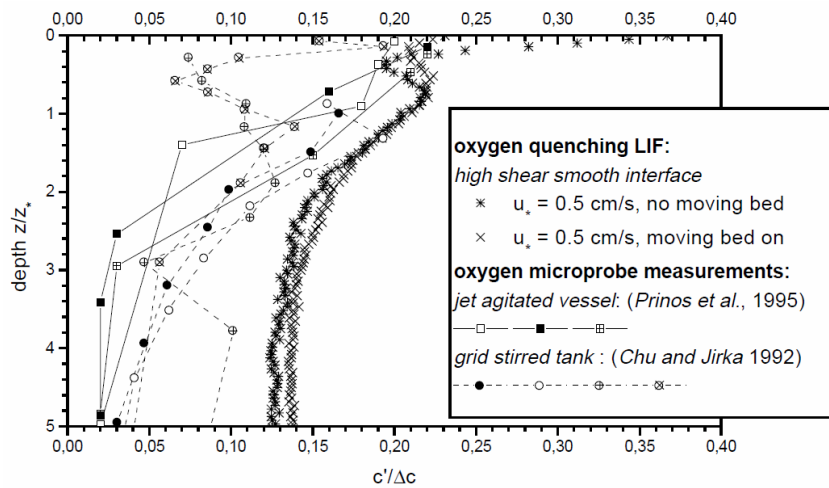
$$c_+^{\prime 2}(z_+) = \int_0^1 \operatorname{erfc}^2\left(\frac{z_+}{2\sqrt{t_+}}\right) dz_+ - \left(\int_0^1 \operatorname{erfc}\left(\frac{z_+}{2\sqrt{t_+}}\right) dz_+\right)^2. \quad (9.4)$$

The obtained results in this section are compared with this model.

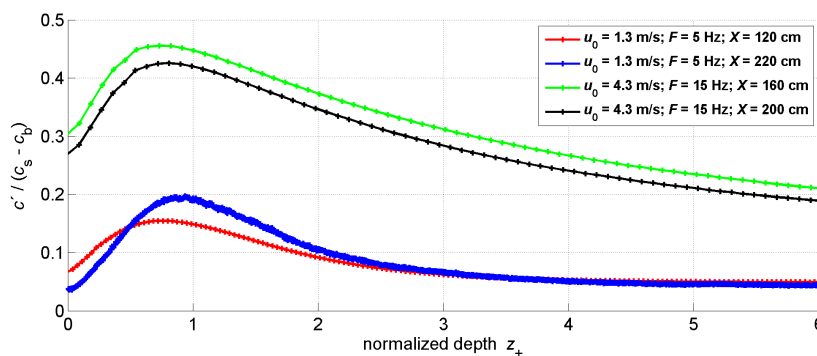
Figure 9.8(c) shows results of this thesis of the RMS  $O_2$  fluctuation concentration  $c'_+$  with respect to the water depth. Two profiles were measured at a flat water surface ( $F = 5$  Hz, red and blue profiles), the other two at a wavy water surface ( $F = 15$  Hz, green and black profiles). To scale the data, the thickness  $\delta_{\text{mbL}}$  of the mass boundary layer, the concentration at the water surface  $c_s$ , and the concentration in the water bulk  $c_b$  were used. These were obtained from the



(a) Profiles of oxygen concentration fluctuations measured in grid-stirred tanks. From Herlina and Jirka [2008].



(b) Profiles of oxygen concentration fluctuation measured in a wind-wave tunnel for a smooth water surface. From Münsterer [1996]



(c) This Figure shows own results: Profiles of oxygen concentration fluctuation measured in the Heidelberg wind-wave tunnel for a flat ( $F = 5$  Hz) and a wavy ( $F = 15$  Hz) water surface.

**Figure 9.8.:** Measured concentration fluctuation profiles with respect to the normalized water depth. Figures (a) and (b) show measurements performed in a grid-stirred tank and a wind-wave tunnel, respectively. Figure (c) presents results of this thesis.

## 9. Results

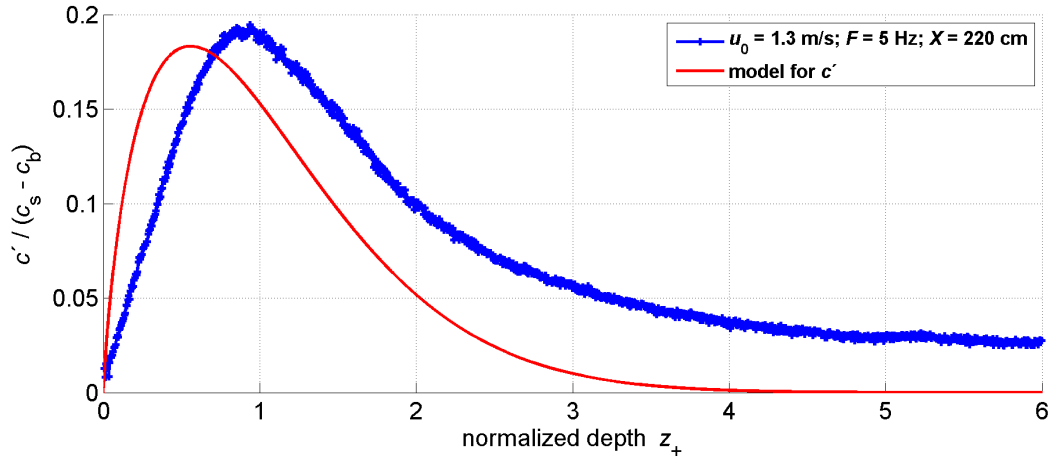


**Figure 9.9.:** Normalized oxygen concentration fluctuation profiles with respect to the normalized depth  $z_+$  measured at a flat water surface. The continuous red line shows the model for the RMS concentration fluctuation presented in Section 2.2.4.

fit procedure with the surface renewal model, which has been explained in the previous section. Profiles are expressed in terms of dimensionless depth  $z_+ = \frac{z}{\delta_{mbl}}$  and dimensionless concentration  $c'_+ = \frac{c'}{c_s - c_b}$ .

### 9.5.1. Additional Contributions to the Variance

In Section 3.1.3, effects are outlined that add up to a bias to the fluctuations by increasing the  $c'$  value. If the additional variance has no depth dependence, its contribution can be subtracted by determining the  $c'$  value in the bulk. Two of the effects, the temperature effect and the error due to a defective surface detection, show a depth dependence. The temperature effect can be suppressed effectively by using a low duty cycle of the laser. The explanation for this solution is given in Section 3.1.2. The error due to a wrong surface detection plays a role only for high wind speeds, where the detection is complicated due to high surface slopes (Section 8.2.2). Conclusively, profiles of  $c'$  with an additional variance that show no depth dependence are obtained at low wind speeds and a low duty cycle of the laser. The profile in Figure 9.8(c), recorded at a fetch of 120 cm (the blue line) is such a profile (dataset C in Table 7.1).

### 9.5.2. Fluctuations at a Flat Water Surface

For the concentration fluctuation profile recorded at a low wind speed of  $1.3 \text{ ms}^{-1}$  and a low duty cycle of 0.45 % of the laser, the contribution to the variance due additional effects (Section 3.1.3) can be subtracted to obtain the actual concentration fluctuation. This was done by determining the measured  $c'$  value in the bulk. As the concentration in the well-mixed bulk has a homogeneous concentration, the fluctuations have to vanish. Figure 9.9 shows the corrected fluctuation profile after that subtraction. The model for  $c'$  (equation (9.4)) is indicated in the same plot. The plot shows that the RMS concentration fluctuations drop to zero at the water

surface. This is in agreement with the model for  $c'$  and with the assumptions of both, the surface renewal and the small eddy model. In contradiction to the presented measurement at a flat water surface and the model description, the measurements of Münsterer [1996] (see Figure 9.8(b)) suggested that the  $O_2$  concentration fluctuations do not vanish at the water surface. The measurements of Herlina [2005] (Figure 9.8(a)) and Schulz and Janzen [2009] in grid-stirred tanks showed an indication that the RMS concentration fluctuations vanish at the water surface.

The developed model for  $c'$  underestimates the peak position of the measured profile by about 30 %. Nevertheless, the model represents the maximum value with a high precision (uncertainty below 5 %). The  $c'$  model also reflects the general shape of the profile well.

To conclude, measurements of the  $O_2$  concentration fluctuation indicate that the concentration fluctuations vanish at the water surface. These are the first measurements in a wind-wave tunnel that measured vanishing concentration fluctuations at the water surface.

### 9.5.3. Fluctuations at a Wavy Water Surface

For the concentration profiles recorded at a wavy water surface the additional effects adding up to the variance cannot be subtracted, because of a depth dependence of the effects, as discussed in Section 9.5.1. Figure 9.8(c) indicates that the  $c'$  value at the surface is higher than in the bulk. The origin of this effect can be due to actual surface renewal events, leading to non-zero fluctuations at the surface for a wavy water surface. It is also possible that the fluctuation at the surface is greater zero because of errors in the surface detection.

To the best of the author's knowledge, these are the first measurements of concentration fluctuations at a wavy water surface in a wind-wave tunnel. A peak in the RMS profile at about  $z_+ = 0.7$  is observed.

## 9.6. Oxygen Transfer Rates

This section presents obtained transfer velocities  $k_{LIF}$  and  $k_b$  that were determined with the LIF method and the mass balance method, respectively. The local transfer velocities  $k_{LIF}$  are derived from the boundary layer thickness  $\delta_{mbl}$  with equation (2.23)

$$k = \frac{D}{\delta_{mbl}}. \quad (9.5)$$

In Section 9.6.1, the obtained values of  $\delta_{mbl}$  are presented. Section 9.6.2 shows a comparison of the transfer velocities  $k_{LIF}$  and  $k_b$ . In Section 9.6.3, the parametrization of the measured transfer velocities  $k_{LIF}$  with friction velocity  $u_*$ , mean square slope  $\langle s^2 \rangle$ , and  $u_0$  are presented and compared.

## 9. Results

**Table 9.3.:** The checkmarks indicate the conditions of wind speed (in units of the wind engine frequency  $F$ ) and fetch  $X$  where data was taken, the surface detection algorithm worked successfully, and the data did not show systematic errors.

$F$ [Hz]	5	6	7	8	9	10	11	12	13	14	15	16	17	17.5
fetch $X = 100$ cm						✓					✓			✓
fetch $X = 120$ cm											✓			
fetch $X = 140$ cm			✓	✓	✓	✓	✓	✓	✓	✓	✓	✓	✓	
fetch $X = 160$ cm											✓			
fetch $X = 200$ cm											✓			
fetch $X = 220$ cm	✓										✓			

### 9.6.1. Thickness of the Mass Boundary Layer

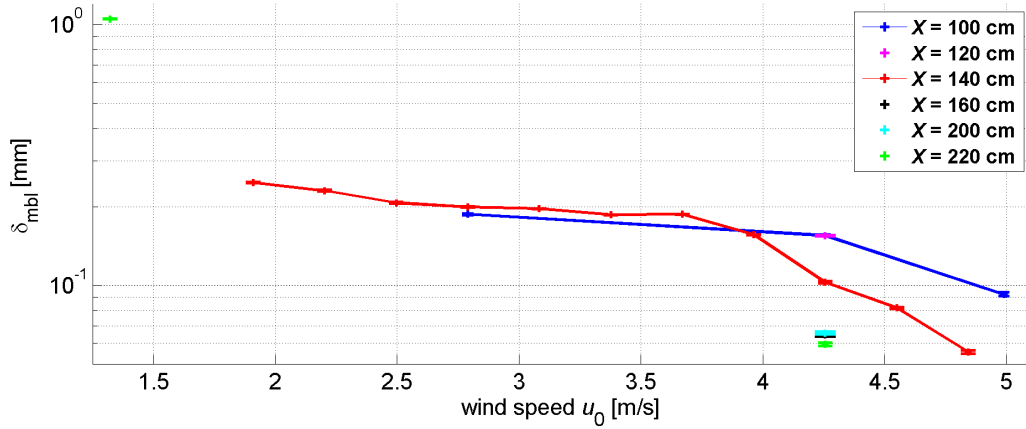
The thickness of the mass boundary layer  $\delta_{\text{mbl}}$  is calculated by fitting the predicted function by the surface renewal model to the mean concentration profiles, as explained in Section 9.4.1. All calculations in this section are based on the surface renewal model, as this model is the best description for the concentration profiles according to Section 9.4.1. Only the data that did not show systematic errors was used for the further analysis of the concentration profiles. Table 9.3 shows the conditions of fetch  $X$  and wind engine frequency  $F$ , where data without systematic errors was measured. Systematic errors in the data occur at low wind speeds, as described in Section 9.4.

Figure 9.10 shows the thickness of the mass boundary layer  $\delta_{\text{mbl}}$  with respect to wind speed  $u_0$ . The thickness  $\delta_{\text{mbl}}$  decreases with increasing wind speed  $u_0$ . This is in agreement with the theory in Section 2.1.2, as the turbulent diffusivity  $K_c$  increases with increasing shear stress, leading to a decreasing boundary layer thickness  $\delta_{\text{mbl}}$ . The fetch dependence of the boundary layer thickness  $\delta_{\text{mbl}}$  is also observed in Figure 9.10 at a wind speed of about  $4.3 \text{ m s}^{-1}$ , where data from six values of fetch is shown. We see a decreasing trend of the boundary layer thickness  $\delta_{\text{mbl}}$  with increasing fetch  $X$ . This effect is due to a growing turbulent diffusivity  $K_c$  with increasing fetch  $X$ . This is confirmed with Figure 7.1(c), that shows a growing mean square slope  $\langle s^2 \rangle$  with increasing fetch  $X$ .

### 9.6.2. Comparison with Mass Balance Measurements

In this section, transfer velocities  $k_{\text{LIF}}$  are compared with transfer velocities  $k_{\text{b}}$ , that were measured with the LIF method and the mass balance method, respectively. Figure 9.11(a) shows LIF transfer velocities  $k_{\text{LIF}}$ , measured at different fetch  $X$ , and the bulk transfer velocities  $k_{\text{b}}$  with respect to wind speed  $u_0$ . The mass balance method yields the transfer velocity  $k_{\text{b}}$ , integrated over fetch. Only the LIF method is able to measure local transfer velocities. The bulk transfer velocity  $k_{\text{b}}$  is strictly increasing with the wind speed  $u_0$ , as expected. The values measured with the LIF method are in the right order of magnitude compared with  $k_{\text{b}}$ . This is a promising sign that the LIF technique is able to measure correct local transfer velocities  $k_{\text{LIF}}$ .

The fetch dependence of the local transfer velocity  $k_{\text{LIF}}$  is shown in Figure 9.11(b). All



**Figure 9.10.:** Thickness of the mass boundary layer  $\delta_{\text{mbl}}$  with respect to wind speed  $u_0$  measured with the LIF method for different fetch  $X$ .

data in this plot was measured at the same wind speed  $u_0$ . The red line depicts the bulk transfer velocity for comparison. The fetch dependence of the transfer velocity  $k_{\text{LIF}}$  is due to the increasing turbulent diffusivity  $K_c$  with fetch, as discussed in the previous section. A strong increment in the transfer velocity  $k_{\text{LIF}}$  occurs between fetch  $X$  of 120 cm and 160 cm. The mean square slope for the same wind speed shows a dominant increment between the fetch of 100 cm and 160 cm, as depicted in Figure 7.1(c). This qualitative correlation shows that the gas transfer in the wind-wave tunnel strongly depends on fetch.

By estimating the averaged transfer velocity  $\overline{k_{\text{LIF}}}$  from the local transfer velocities, the comparability of the two techniques is tested. With the total fetch of 3.66 m (see Figure 4.1), and the assumption of a constant transfer velocity below 120 cm and above 160 cm, the average transfer velocity  $\overline{k_{\text{LIF}}}$  is about  $9 \text{ cm h}^{-1}$ . This is an overestimation of the bulk transfer velocity of about 35%. However, the method to compare  $k_{\text{LIF}}$  with  $k_b$  shows a promising potential for the validation of the local gas transfer measurements by measuring with finer increments over the total fetch. The comparison between  $k_{\text{LIF}}$  and  $k_b$  can also be used as a method to validate gas transfer models (e.g. small eddy or surface renewal), by calculating the transfer velocity  $k_{\text{LIF}}$  with the fit functions of different models.

### 9.6.3. Parametrizations of the Transfer Velocity

In this section, parametrizations of the measured transfer velocities  $k_{\text{LIF}}$  with the friction velocity  $u_*$ , the mean square slope  $\langle s^2 \rangle$ , and the wind speed  $u_0$  are presented and compared. As  $u_*$  and  $\langle s^2 \rangle$  are local phenomena, the parametrizations can only be performed for the locally measured transfer velocities  $k_{\text{LIF}}$ .

Figure 9.12 shows the local transfer velocities  $k_{\text{LIF}}$  with respect to  $u_*$ ,  $\langle s^2 \rangle$ , and  $u_0$ . The plots are all shown with a linear and semi logarithmic scale on the left side and on the right side, respectively, to facilitate the comparison. In Figures 9.12(a) and 9.12(b), the Deacon model

## 9. Results

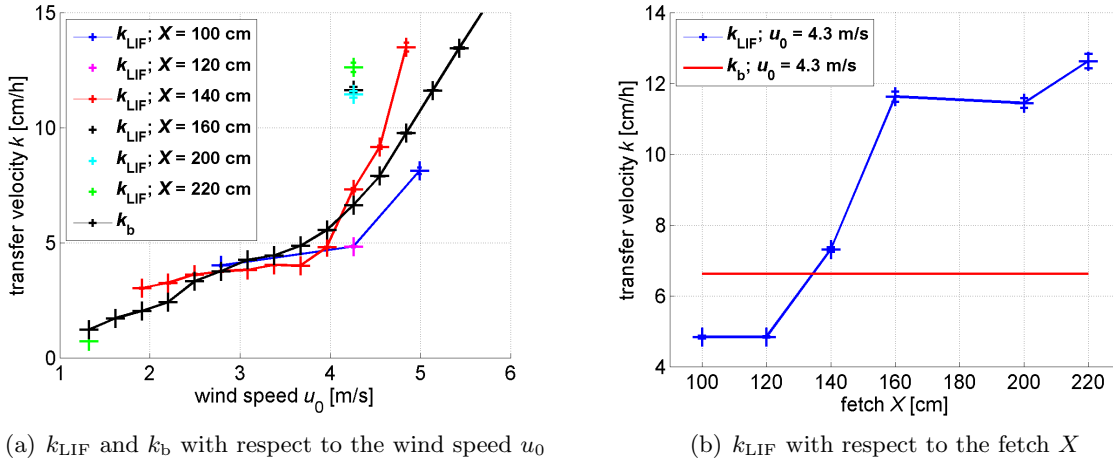


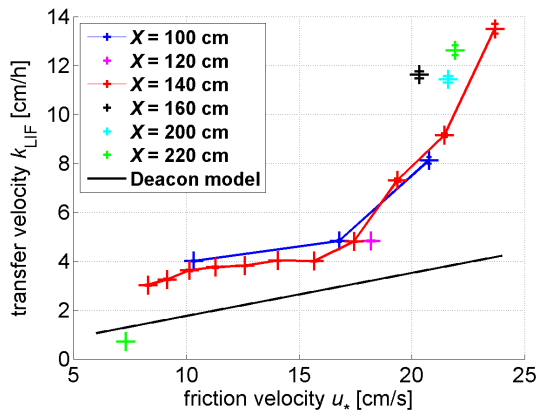
**Figure 9.11.:** Transfer velocities  $k_{LIF}$  and  $k_b$  measured with the LIF method and the mass balance method, respectively.

(Section 2.2.5) is shown for comparison<sup>3</sup>. The measured transfer velocities  $k_{LIF}$  are all above the prediction of the Deacon model, except for the value measured at the lowest wind speed. The Deacon model is a lower limit for the gas exchange at the air-water interface, because of the assumption of a rigid interface with a Schmidt number exponent of  $n = 2/3$ . The value of the transfer velocity below the Deacon model is supposedly defective because it is about 42% below the measured transfer velocity  $k_b$  with the mass balance method (see Figure 9.11(a)). Figures 9.12(c) and 9.12(d) show the local transfer velocity  $k_{LIF}$  with respect to mean square slope  $\langle s^2 \rangle$ . The mean square slope was proposed by Jähne et al. [1987] to be a suitable forcing parameter. A linear correlation of the gas transfer velocity with mean square slope was suggested by Frew et al. [2004]. The parametrization with the reference wind speed  $u_0$  in Figures 9.12(e) and 9.12(f) clearly shows that the fetch has to be considered for the local transfer velocity.

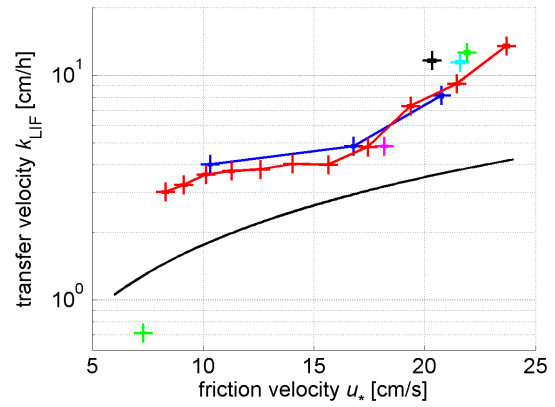
The visual comparison of the three parametrizations indicates that the gas transfer in the linear wind-wave tunnel is best described with friction velocity  $u_*$ , followed by mean square slope  $\langle s^2 \rangle$ , and wind speed  $u_0$ . The observed dataset indicates that the gas transfer is not fully described with the three measured forcing parameters. At higher fetches, transfer velocities are enhanced in all parametrizations. To be able to make a step beyond these statements, there is need for more systematic measurements at various combinations of fetch  $X$  and wind engine frequencies  $F$ .

To conclude, it was illustrated that the gas transfer is a local phenomenon that cannot be explained by the wind speed  $u_0$  alone. The parametrizations with friction velocity and mean square slope are better descriptions for the data than the wind speed  $u_0$ . The results presented here are the first systematic measurements of local gas transfer velocities  $k_{LIF}$  in a wind-wave tunnel.

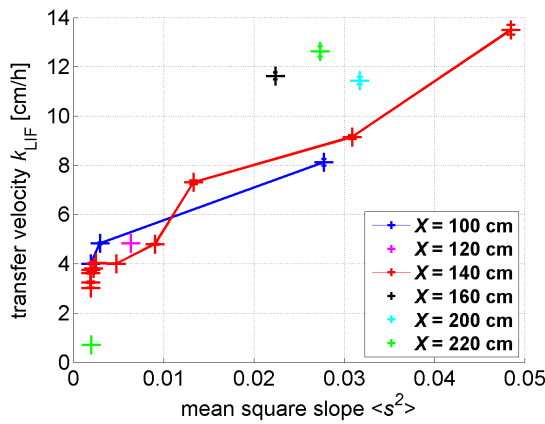
<sup>3</sup>The Schmidt number of  $O_2$  (at a temperature of 23°C in clean water) of  $Sc = 445$  was used for the calculation, according to the values of the diffusion constant and the viscosity from [Cussler, 2009] and [Yaws, 1999].



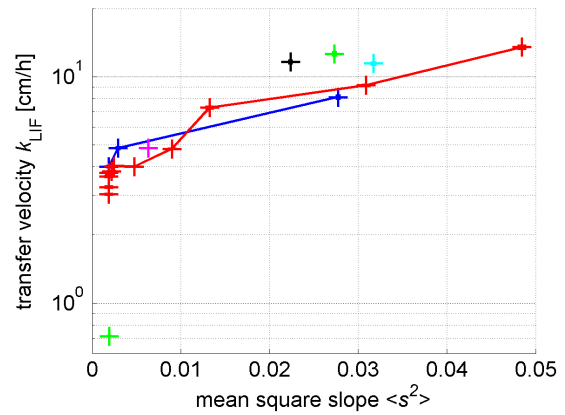
(a) parametrization with  $u_*$



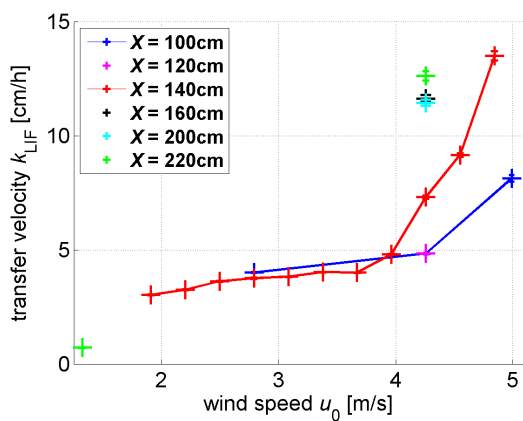
(b) parametrization with  $u_*$  - semi logarithmic plot



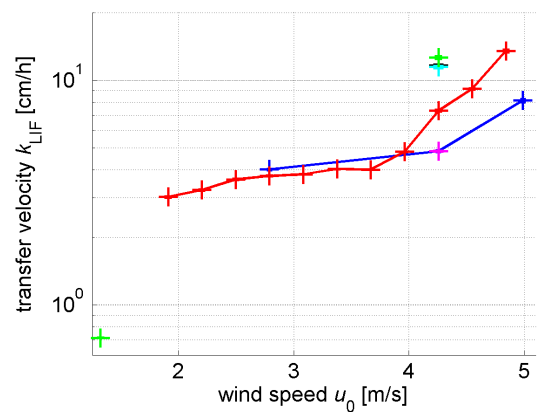
(c) parametrization with  $\langle s^2 \rangle$



(d) parametrization with  $\langle s^2 \rangle$  - semi logarithmic plot



(e) parametrization with  $u_0$



(f) parametrization with  $u_0$  - semi logarithmic plot

**Figure 9.12.:** Local transfer velocities  $k_{LIF}$  with respect to the forcing parameters  $u_*$ ,  $\langle s^2 \rangle$ , and  $u_0$ . All plots contain the same data. The plots on the left and on the right side are with a linear scale and with a semi logarithmic scale, respectively. For the parametrization with friction velocity  $u_*$ , the Deacon model (Section 2.2.5) is shown for comparison.



# 10. Conclusion and Outlook

## 10.1. Conclusion

An improved non-intrusive laser-induced fluorescence (LIF) method (Section 3.1.1) to measure vertical oxygen ( $\text{O}_2$ ) concentration profiles in the water-sided mass boundary layer has been presented in this thesis. A spatial resolution of  $6.2\ \mu\text{m}$  (Section 6.1.1) and temporal resolution of up to  $1.2\ \text{kHz}$  (Table 7.2) was achieved to be able to resolve the thin mass boundary layer and fast processes. Using the Ru complex as an oxygen indicator allowed for the visualization of  $\text{O}_2$  transport processes (Section 9.2) at the flat and wavy water surface in a linear wind-wave tunnel with 22 times higher sensitivity as possible with the commonly used PBA indicator.

Noteworthy developments in the description of the quenching mechanism have been achieved during the course of this thesis. The Stern-Volmer equation (2.89) has been generalized for arbitrary laser irradiance on the basis of rate equations (Section 2.3.4). In the original study by Stern and Volmer [1919], the approximation of a weak excitation was made. Here, it was shown that an additional damping factor  $\epsilon_{\text{D}}$ , denoting the fraction of excited molecules, needs to be included to yield the effective quenching constant, i.e.  $K_{\text{eff}} = \epsilon_{\text{D}} \cdot K_{\text{SV}}$ . Measurements showed that the generalized Stern-Volmer equation describes the quenching effect for different laser irradiance values very well (Section 5.2.2). With this new insight into the effective quenching mechanism, the Stern-Volmer constant  $K_{\text{SV}}$  of the Ru complex was measured with high precision better than 2%. Additionally, the temperature dependence of the Stern-Volmer constant  $K_{\text{SV}}(T)$  between  $17^\circ\text{C}$  and  $27^\circ\text{C}$  was measured (Section 5.2.3). The precise knowledge of the Stern-Volmer constant  $K_{\text{SV}}$  of the Ru complex allowed for the determination of absolute  $\text{O}_2$  concentrations with less systematic uncertainties than in previous studies.

A precise surface detection is crucial for the determination of averaged oxygen profiles, since the depth coordinate is measured with respect to the water surface. For a wavy water surface, the thickness of the mass boundary layer is much smaller than the root mean square surface elevation. An algorithm (Section 8.2.2) was developed to detect the water surface in the LIF image sequences for flat and wavy water conditions. This allows one to average over a large number of single  $\text{O}_2$  concentration profiles even at a moderately wavy water surface to obtain mean  $\text{O}_2$  concentration profiles with a high precision (Section 9.4).

## 10. Conclusion and Outlook

Systematic LIF measurements (Section 7.3.1) were performed at various fetch and wind speed combinations to study the gas transfer across the air-water interface at the Heidelberg linear wind-wave tunnel. From these measurements, the local transfer velocity  $k_{\text{LIF}}$  of  $\text{O}_2$  was determined from the mean  $\text{O}_2$  concentration profiles (Section 8.2.4). The wind speed dependence of the bulk transfer velocities  $k_{\text{b}}$  was measured (Section 7.3.2) and compared to the transfer velocities  $k_{\text{LIF}}$ . The measured transfer velocities  $k_{\text{LIF}}$  are in good agreement with the bulk transfer velocities  $k_{\text{b}}$  (Section 9.6.2).

The small eddy model and the surface renewal model (Section 2.2) describe the gas exchange mechanisms for a rigid and a free air-water interface. The measured mean  $\text{O}_2$  concentration profiles were used to test these models. For a flat water surface, the measured mean  $\text{O}_2$  concentration profiles are best described by the surface renewal model for a Schmidt number exponent  $n$  of  $2/3$  (Section 9.4.1). For a wavy water surface, both models for the Schmidt number exponent  $n$  of  $1/2$  are a good description for the concentration profiles and a distinction between the small eddy model and the surface renewal model is not possible (Section 9.4.1). Further, the measured mean  $\text{O}_2$  concentration profiles also show a transition in the shape with the onset of waves. This transition is in agreement with predicted concentration profiles by the surface renewal model when the air-water interface changes from a rigid to a free state. This transition was observed with a higher precision than in previous studies due to the improvements discussed in the measurement technique.

Vertical profiles of the  $\text{O}_2$  fluctuation were calculated in addition to profiles of the mean  $\text{O}_2$  concentration (Section 9.5). In the case of a flat water surface, the data shows evidence that the  $\text{O}_2$  concentration fluctuations vanish at the water surface (Section 9.5.2). This is in agreement with the small eddy model and the surface renewal model for a rigid air-water interface, as well as with measurements in grid-stirred tanks. A model for the vertical profiles of concentration fluctuations was developed, based on the assumptions of the surface renewal model for a rigid air-water interface (Section 2.2.4). According to this model, the peak position of the concentration fluctuation profile is at a depth of about 56 % of the mass boundary layer thickness, which is about 30 % below the measured peak position.

In the case of a wavy water surface, the determined concentration fluctuations did not vanish at the water surface. Presumably this is due to the limited spatial resolution and additional error sources at the water surface (Section 3.1.3), rather than  $\text{O}_2$  concentration fluctuations greater than zero.

Gas exchange parametrizations based on data from linear tanks show the difficulty of integrating over inhomogeneous conditions. Therefore, systematic measurements of wind profiles at various fetch and wind speed combinations (Section 7.2.1) in the Heidelberg linear wind-wave tunnel were conducted, that enabled the determination of the total momentum flux (Section 9.1).

These measurements and the wave measurements by a co-worker allowed for the parametrization of gas transfer velocities  $k_{\text{LIF}}$  with common forcing parameters: friction velocity, mean square slope of the water surface, and wind speed. Section 9.6.3 shows that the measured local transfer velocities are best described with the friction velocity. To the best of the author's knowledge, this thesis presents the first results from a systematic study of local gas transfer velocities with respect to fetch and friction velocity in a wind-wave tunnel. The developed method shows a promising potential to gain new insights about parameter dependencies of gas exchange.

## 10.2. Outlook

It is still an ongoing debate whether gas transfer velocities can be scaled to heat transfer velocities [Asher et al., 2004; Atmane et al., 2004; Jähne et al., 1989]. The developed LIF method combined with the *active controlled flux technique* (ACFT) [Schimpf et al., 2011], available in our group, offers the possibility to compare local gas transfer velocities to local heat transfer velocities in the Heidelberg linear wind-wave tunnel.

The extension of the developed one-dimensional LIF method to two dimensions and eventually three dimensions is planned in upcoming projects [Kräuter, 2015; Trofimova, 2015]. These methods will give new insights in the three dimensional structure of transport phenomena at the air-water interface, such as second-order currents or small scale Langmuir circulations.

A simultaneous measurement with the LIF method and the imaging slope gauge (ISG) (Section 7.2.2) offers the possibility to study the influence of local phenomena related to small scale breaking waves on the local gas transfer velocity.



## Bibliography

- W. Asher, H. Liang, C. Zappa, M. Loewen, M. Mukto, T. Litchendorf, and A. Jessup. Statistics of surface divergence and their relation to air-water gas transfer velocity. *Journal of Geophysical Research*, 117(C5):C05035, 2012.
- W. Asher and T. Litchendorf. Visualizing near-surface concentration fluctuations using laser-induced fluorescence. *Experiments in Fluids*, 46:243–253, 2009.
- W. E. Asher, A. T. Jessup, and M. A. Atmane. Oceanic application of the active controlled flux technique for measuring air-sea transfer velocities of heat and gases. *J. Geophys. Res.*, 109:C08S12, 2004.
- W. E. Asher and J. F. Pankow. Prediction of gas/water mass transport coefficients by a surface renewal model. *Environmental Science & Technology*, 25(7):1294–1300, 1991.
- M. A. Atmane, W. Asher, and A. T. Jessup. On the use of the active infrared technique to infer heat and gas transfer velocities at the air-water free surface. *J. Geophys. Res.*, 109:C08S14, 2004.
- M. A. Atmane and J. George. Gas transfer across a zero-shear surface: a local approach. In E. Saltzman, M. Donelan, W. Drennan, and R. Wanninkhof, editors, *Gas Transfer at Water Surfaces*, volume 127 of *Geophysical Monograph*. American Geophysical Union, 2002.
- F. N. Castellano and J. R. Lakowicz. A water-soluble luminescence oxygen sensor. *Photochemistry and Photobiology*, 67(2):179–183, Feb 1998.
- G. Caulliez, V. Makin, and V. Kudrayavtsev. Drag of the water surface at very short fetches: observations and modelling. *Journal of Physical Oceanography*, 38:2038–2055, 2008.
- C. R. Chu and G. H. Jirka. Turbulent gas flux measurements below the air-water interface of a grid-stirred tank. *Int. J. Heat Mass Transfer*, 35(8):1957–1968, 1992.
- M. Coantic. A model of gas transfer across air–water interfaces with capillary waves. *Journal of Geophysical Research*, 91:3925–3943, 1986.
- J. P. Crimaldi. The effect of photobleaching and velocity fluctuations on single-point lif measurements. *Experiments in Fluids*, 23:325–330, 1997. 10.1007/s003480050117.

## Bibliography

- E. L. Cussler. *Diffusion - Mass Transfer in Fluid Systems*. Cambridge University Press, Cambridge, 3 edition, 2009.
- P. V. Danckwerts. Significance of a liquid-film coefficients in gas absorption. *Ind. Eng. Chem.*, 43:1460–1467, 1951.
- E. L. Deacon. Gas transfer to and across an air-water interface. *Tellus*, 29:363–374, 1977.
- J. Demas and D. Taylor. On the intersystem crossing yields in ruthenium (ii) and osmium (ii) photosensitizers. *Inorganic Chemistry*, 18(11):3177–3179, 1979.
- M. A. Donelan and R. Wanninkhof. Gas transfer at water surfaces - concepts and issues. In M. A. Donelan, W. M. Drennan, E. S. Saltzman, and R. Wanninkhof, editors, *Gas Transfer at Water Surfaces*. American Geophysical Union, 2002.
- S. R. Duke and T. J. Hanratty. Measurements of the concentration field resulting from oxygen absorption at a wavy air–water interface. In B. Jähne and E. C. Monahan, editors, *Air-water Gas Transfer, Selected Papers from the Third International Symposium on Air-Water Gas Transfer*, Hanau, 1995.
- P. Fahle. Diplomarbeit, Institut für Umwelphysik, Universität Heidelberg, Germany, 2012. started 10.10.2011.
- A. Falkenroth. *Visualisation of Oxygen Concentration Profiles in the Aqueous Boundary Layer*. Dissertation, Fakultät für Chemie und Geowissenschaften, Univ. Heidelberg, 2007.
- N. M. Frew, E. J. Bock, U. Schimpf, T. Hara, H. Haußecker, J. B. Edson, W. R. McGillis, R. K. Nelson, B. M. McKeanna, B. M. Uz, and B. Jähne. Air-sea gas transfer: Its dependence on wind stress, small-scale roughness, and surface films. *J. Geophys. Res.*, 109:C08S17, 2004.
- T. Förster. *Fluoreszenz Organischer Verbindungen*. Vandenhoeck & Ruprecht, Göttingen, 1951.
- E. . S. Group. Emva standard 1288 - standard for characterization of image sensors and cameras, 2010.
- P. Harriott. A random eddy modification of the penetration theory. *Chem. Eng. Sci.*, 17:149–154, 1962.
- E. Hecht. *Optik*. Oldenbourg, München, 5 edition, 2009.
- Herlina. *Gas Transfer at the Air–Water Interface in a Turbulent Flow Environment*. PhD thesis, University of Karlsruhe, 2005.
- I. Herlina and G. H. Jirka. Experiments on gas transfer at the air–water interface induced by oscillating grid turbulence. *J. Fluid. Mech.*, 594:183–208, 2008.

- A. Herzog. *Imaging of Water-sided Gas-Concentration Fields at a Wind-Driven, Wavy Air-Water Interface*. Dissertation, Institut für Umweltphysik, Fakultät für Physik und Astronomie, Univ. Heidelberg, 2010.
- J. W. Hiby, D. Braun, and K. H. Eickel. Eine Fluoreszenzmethode zur Untersuchung des Stoffübergangs bei der Gasabsorption im Rieselfilm. *Chemie-Ing.-Techn.*, 39:297–301, 1967.
- R. Higbie. The rate of absorption of a pure gas into a still liquid during short periods of exposure. *Trans. Am. Inst. Chem. Eng.*, 31:365–389, 1935.
- J. O. Hinze. *Turbulence*. McGraw-Hill series in mechanical engineering. McGraw-Hill, New York, 2nd edition, 1975.
- D. T. Ho, R. Wanninkhof, P. Schlosser, D. S. Ullman, D. Hebert, and K. F. Sullivan. Toward a universal relationship between wind speed and gas exchange: Gas transfer velocities measured with  $^3\text{He}/\text{SF}_6$  during the southern ocean gas exchange experiment. *Journal of Geophysical Research*, 116, 2011.
- C. T. Hsu, E. Y. Hsu, and R. L. Street. On the structure of turbulent flow over a progressive water wave: theory and experiment in a transformed, wave-following co-ordinate system. *Journal of Fluid Mechanics*, 105:87–117, 1981.
- B. Jähne. *Zur Parametrisierung des Gasaustauschs mit Hilfe von Laborexperimenten*. Dissertation, Institut für Umweltphysik, Fakultät für Physik und Astronomie, Univ. Heidelberg, 1980. IUP D-145.
- B. Jähne. *On the transfer processes at a free air-water interface*. Habilitation thesis, Institut für Umweltphysik, Fakultät für Physik und Astronomie, Univ. Heidelberg, 1985. IUP D-200.
- B. Jähne. From mean fluxes to a detailed experimental investigation of the gas transfer process. In S. C. Wilhelms and J. S. Gulliver, editors, *2nd International Symposium on Gas Transfer at Water Surfaces - Air-Water Mass Transfer, Minneapolis 1990*, pages 244–256. ASCE, 1991.
- B. Jähne. *Practical Handbook on Image Processing for Scientific and Technical Applications*. CRC Press, Boca Raton, FL, 2 edition, 2004.
- B. Jähne. *Digital Image Processing*. Springer, Berlin, 6 edition, 2005.
- B. Jähne. personal communication. 2012.
- B. Jähne, P. Libner, R. Fischer, T. Billen, and E. J. Plate. Investigating the transfer process across the free aqueous boundary layer by the controlled flux method. *Tellus*, 41B(2):177–195, 1989.
- B. Jähne, K. O. Münnich, R. Böisinger, A. Dutzi, W. Huber, and P. Libner. On the parameters influencing air-water gas exchange. *J. Geophys. Res.*, 92:1937–1950, Feb. 1987.

## Bibliography

- B. Jähne and K. Riemer. Two-dimensional wave number spectra of small-scale water surface waves. *J. Geophys. Res.*, 95(C7):11531–11646, 1990.
- B. Kinsman. *Wind Waves: Their Generation and Propagation on the Ocean Surface*. Prentice-Hall, Englewood Cliffs, 1965.
- K. E. Krall. *Laboratory Investigations of Air-Sea Gas Transfer under a Wide Range of Water Surface Conditions*. Dissertation, Institut für Umweltphysik, Fakultät für Physik und Astronomie, Univ. Heidelberg, 2013.
- C. Kräuter. Aufteilung des transferwiderstands zwischen luft und wasser beim austausch flüchtiger substanzen mittlerer löslichkeit zwischen ozean und atmosphäre. Diplomarbeit, Institut für Umweltphysik, Fakultät für Physik und Astronomie, Univ. Heidelberg, 2011.
- C. Kräuter. Dissertation, Institut für Umweltphysik, Fakultät für Physik und Astronomie, Univ. Heidelberg, 2015. started 01.01.2012.
- J. R. Lakowicz. *Principles of Fluorescence Spectroscopy*. Springer, 3. edition, 2006.
- W. K. Lewis and W. G. Whitman. Principles of gas absorption. *Industrial and Engineering Chemistry*, 16:1215–1220, 1924.
- T. Münsterer. *LIF Investigation of the Mechanisms Controlling Air–Water Mass Transfer at a Free Interface*. Dissertation, Institut für Umweltphysik, Fakultät für Physik und Astronomie, Univ. Heidelberg, 1996.
- T. Münsterer and B. Jähne. LIF measurements of concentration profiles in the aqueous mass boundary layer. *Exp Fluids*, 25:190–196, 1998.
- J. F. Pankow, W. E. Asher, and E. J. List. *Carbon dioxide transfer at the gas-water interface as a function of system turbulence*, pages 101–111. Springer Netherlands, 1984.
- A. P. Pentland. A new sense for depth of field. *Pattern Analysis and Machine Intelligence, IEEE Transactions on*, PAMI-9(4):523–531, july 1987.
- S. B. Pope. *Turbulent Flows*. Cambridge University Press, 6 edition, 2009.
- P. Pringsheim. *Fluorescence and Phosphorescence*. Interscience Publisher, 1949.
- P. Prinos, M. Atmane, and J. George. Gas-flux measurements and modelling below an air-water interface. In B. Jähne and E. C. Monahan, editors, *Air-water Gas Transfer, Selected Papers from the Third International Symposium on Air–Water Gas Transfer*, pages 49–57, Hanau, 1995. Aeon.
- H. Reichardt. Vollständige Darstellung der turbulenten Geschwindigkeitsverteilung in glatten Leitungen. *Zeitschrift für angewandte Mathematik und Mechanik*, 31:208–219, 1951.

- R. Rocholz, P. Fahle, and B. Jähne. High speed and high resolution wave imaging to investigate the initial generation of wind waves at very small fetch. WISE (Waves In Shallow Environments) 2012, 19th International Conference, Barcelona, Spain, 16-20 April 2012.
- R. Rocholz, S. Wanner, U. Schimpf, and B. Jähne. Combined visualization of wind waves and water surface temperature. In S. Komori, W. McGillis, and R. Kurose, editors, *Gas Transfer at Water Surfaces 2010*, pages 496–506, 2011.
- W. Roedel. *Physik unserer Umwelt: die Atmosphäre*. Springer-Verlag, 3 edition, 2000.
- R. Sander. Compilation of henry’s law constants for inorganic and organic species of potential importance in environmental chemistry (version 3), 1999.
- A. Savitzky and M. J. E. Golay. Smoothing and differentiation of data by simplified least squares procedures. *Analytical Chemistry*, 36(8):1627–1639, 1964.
- J. Saylor. Photobleaching of disodium fluorescein in water. *Experiments in Fluids*, 18:445–447, 1995. 10.1007/BF00208467.
- U. Schimpf, L. Nagel, and B. Jähne. First results of the 2009 sopran active thermography pilot experiment in the baltic sea. In S. Komori, W. McGillis, and R. Kurose, editors, *Gas Transfer at Water Surfaces 2010*, pages 358–367, 2011.
- H. E. Schulz and J. G. Janzen. Concentration fields near air-water interfaces during interfacial mass transport: oxygen transport and random square wave analysis. *Brazilian Journal of Chemical Engineering*, 26:527 – 536, 09 2009.
- O. Stern and M. Volmer. über die Abklingungszeit der Fluoreszenz. *Phys.Z*, 20:183–188, 1919.
- S. A. Thorpe, editor. *Encyclopedia of Ocean Sciences: Elements of Physical Oceanography*. Elsevier, 2009.
- D. Trofimova. Dissertation, Institut für Umweltphysik, Fakultät für Physik und Astronomie, Univ. Heidelberg, 2015. started 15.01.2012.
- Y. Troitskaya, D. Sergeev, O. Ermakova, and G. Balandina. Statistical parameters of the air turbulent boundary layer over steep water waves measured by the piv technique. *Journal of Physical Oceanography*, 41(8):1421–1454, 2011.
- Y. Troitskaya, D. Sergeev, A. Kandaurov, G. Baidakov, M. Vdovin, and V. Kazakov. Laboratory and theoretical modeling of air-sea momentum transfer under severe wind conditions. *Journal of Geophysical Research*, 117:C00J21, 2012.
- J. W. Walker and W. L. Peirson. Measurement of gas transfer across wind-forced wavy air–water interfaces using laser-induced fluorescence. *Exp Fluids*, 2008.

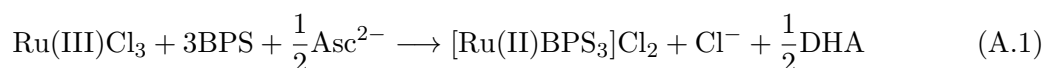
## Bibliography

- S. Wanner. Interaktives rendering von wellendaten windgetriebener wasseroberflächen und ereignisklassifizierung. Diplomarbeit, Institut für Umweltphysik, Fakultät für Physik und Astronomie, Univ. Heidelberg, 2010.
- R. Wanninkhof, W. E. Asher, D. T. Ho, C. Sweeney, and W. R. McGillis. Advances in quantifying air-sea gas exchange and environmental forcing. *Annu. Rev. Mar. Sci.*, 1:213–244, 2009.
- P. Warken. Hochauflösende lif-methode zur messung von sauerstoffkonzentrationsprofilen in der wasserseitigen grenzschicht. Diplomarbeit, Institut für Umweltphysik, Fakultät für Physik und Astronomie, Univ. Heidelberg, 2010.
- R. Winter. *Fluorescent Tracers for air-sided Concentration Profile Measurements at the Air-Water Interface*. Dissertation, Institut für Umweltphysik, Fakultät für Physik und Astronomie, Univ. Heidelberg, 2011.
- L. M. Wolff and T. J. Hanratty. Instantaneous concentration profiles of oxygen accompanying absorption in a stratified flow. *Experiments in Fluids*, 16(6):385–392, 1994.
- L. M. Wolff, Z. C. Liu, and T. J. Hanratty. A fluorescence technique to measure concentration gradients near an interface. In S. C. Wilhelms and J. S. Gulliver, editors, *Air-Water Mass Transfer, selected papers from the 2nd Int. Symposium on Gas Transfer at Water Surfaces*, pages 210–218, Minneapolis, 1991. ASCE.
- C. L. Yaws. *Chemical Properties Handbook: physical, thermodynamic, environmental, transport, safety, and health related properties for organic and inorganic chemicals*. McGraw-Hill, 1999.

# A. Appendix

## A.1. Synthesis of the Ru Complex

The synthesis of the Ru complex (see Section 5.1) was accomplished in the course of this study with the help of a chemistry student, Michael Kettner. To enable the reproduction of the experiments presented in this study, the synthesis of the Ru complex is presented here. Table A.1 shows a summary of the reagents needed for the synthesis. The reaction equation for the synthesis of the Ru complex is the following:



where DHA stands for dehydroascorbic acid. The synthesis of the Ru complex is explained in step-by-step instructions:

1. Organize the four substances listed in Table A.1 and find a magnetic mixer, a magnetic stir bar and a 250 mL beaker glass.
2. Fill the 250 mL beaker glass with 200 mL deionized water and add 1.4 g (6.75 mmol)  $\text{RuCl}_3$  while stirring with the magnetic mixer.
3. Heat the dark-brown solution until it boils.
4. Add 12 g (22.55 mmol) BPS to the boiling solution and let it boil for further 30 minutes. The evaporating water should be refilled so that the beaker glass always contains 200 mL. The color of the solution changes to a greenish brown. Instead of using a beaker glass, a

**Table A.1.:** Summary of reagents

substance	R/S statements	WGK	CAS	M [g/mol]
Ruthenium (III) Chloride	R:34; S:26-36/37/39-45 acid	3	208523-10G	207.43
Dinatrium bathophenantrolindisulfonate (BPS); Diniatrium-4,7-diphenyl-1,10-phenantrolin-disulfonat	-	3	52746-49-3	560.53
Ascorbic acid	-	1	50-81-7	176.12
NaOH-solution 2M	acid	1	1310-73-2	40

## A. Appendix

round-bottomed flask with a reflux condenser can also be used. In that case, no refilling to compensate for the evaporating water is necessary.

5. Add 7.5 g (42.61 mmol) ascorbic acid to the boiling solution. The color changes instantaneously to orange-brown. Cook the solution for another 20 minutes and always refill water to keep the volume constant at 200 mL.
6. Let the solution cool down and perform a calibration of the pH meter (two-point calibration at a pH value of 2 and 7).
7. In the last step, the cooled-down solution should be set to a pH value of 7 by adding NaOH and using the pH meter.

If bigger or smaller amounts of the Ru complex are required, the quantities of the substances should all be changed by the same factor. Less than 50 mL of water should not be used. At higher quantities, the volume of the water can be kept smaller (there is no need to use 1 L of water if all the substances are enlarged by a factor of 5 - 500 mL are sufficient).

### A.2. The Damping Factor $\epsilon_D$ - Alternative Notation

The damping factor  $\epsilon_D$  is formulated here in a different notation as in Section 2.3.4. Instead of using the laser irradiance  $E$ , the ground and excited state concentrations of the fluorophore without quencher  $n_0$  and  $n_0^*$  (see Figure 2.7), respectively, are used.

The damping factor  $\epsilon_D$  (equation (2.87))

$$\begin{aligned}\epsilon_D &= \frac{E_{\text{sat}}}{E + E_{\text{sat}}} \\ &= 1 - \frac{E}{E + E_{\text{sat}}}\end{aligned}\tag{A.2}$$

is written in a different notation, using equations (2.81) and (2.75).

$$\begin{aligned}\epsilon_D &= 1 - \frac{n_0^*}{N} \\ &= \frac{N - n_0^*}{N}\end{aligned}\tag{A.3}$$

Using the fact that the total concentration  $N$  of the fluorophore

$$N = n_0 + n_0^*\tag{A.4}$$

is the sum of the ground state and excited state concentrations without quencher  $n_0$  and  $n_0^*$ , respectively, we obtain

$$\epsilon_D = \frac{n_0}{N}.\tag{A.5}$$

This equation shows, that the damping factor is the fraction of the concentration of Ru complex molecules in the ground state  $n_0$  and the total concentration  $N$  of the Ru complex molecules.

### A.3. Stern-Volmer Plot - Further Presentation

For direct comparison with former measurements by Falkenroth [2007] and Münsterer [1996], the data of the Stern-Volmer plots for the Ru complex is presented in the form

$$\Phi = \frac{\Phi_0}{1 + K_{\text{eff}} \cdot c}, \quad (\text{A.6})$$

see equation (5.2). Figure A.1 shows the photon flux  $\Phi$  with respect to the  $\text{O}_2$  concentration. The data in this figure is the same as shown in Figures 5.5 and 5.6 in Section 5.2.2.

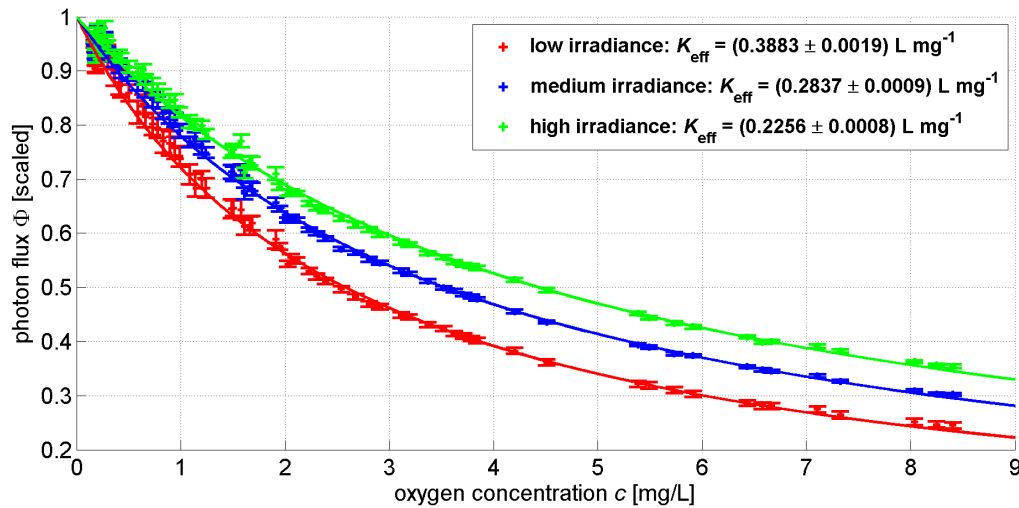


**Figure A.1.:** Photon Flux  $\Phi$  with respect to the  $\text{O}_2$  concentration measured for three laser power values (see Table 5.1). The photon flux  $\Phi$  is scaled to unity at the  $\text{O}_2$  concentration of  $0 \text{ mg L}^{-1}$ . Equation (A.6) is fitted to each of the three data sets, to obtain the effective Stern-Volmer constants  $K_{\text{eff}}$ .

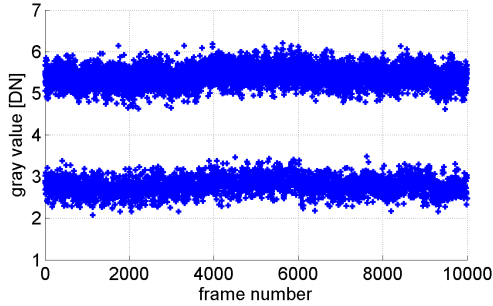
### A.4. Unforeseen Effects of the Camera

After systematic measurements had been conducted, two error sources originating from the camera (see Section 4.2.4) were discovered. Section A.4.1 presents one of the two effects, the so-called two-level noise, that could be eliminated. The other effect, the sawtooth effect, is described in Section A.4.2.

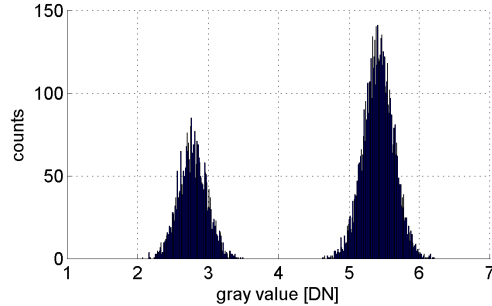
#### A.4.1. Two-Level Noise Effect

Figure A.2 shows the two-level noise effect by analyzing an image sequence containing  $10^4$  single dark images. The mean gray value of each image can be assigned to one of two levels (see

## A. Appendix

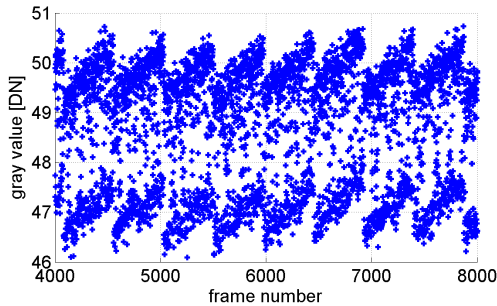


(a) Mean gray values of  $10^4$  dark images with respect to the frame number.

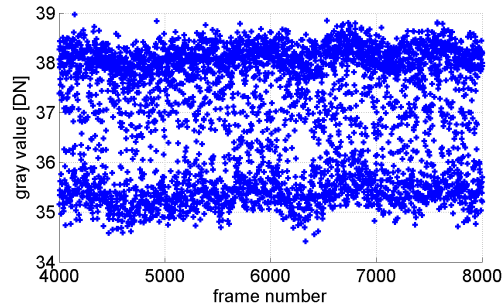


(b) Histogram of the mean gray values.

**Figure A.2.:** Analysis of the two-level noise effect with a sequence of  $10^4$  dark images.



(a) laser in the pulsed mode



(b) laser in the cw (constant wave) mode

**Figure A.3.:** Analysis of the sawtooth effect

Figure A.2(a)). The histogram in Figure A.2(b) shows that the brighter dark image appears more often than the darker one. The same measurement with another camera of the same series did not show the two-level noise effect. The effect was corrected for by calculating two dark images, one for each noise level. To each recorded image, the corresponding dark image was chosen according to the brightness in a dark area in each image.

### A.4.2. Sawtooth Effect

Figure A.3(a) shows the mean gray value of 4000 images of an image sequence recorded with the LIF setup (see Section 4.2). For the measurement, the laser was triggered to give a pulse of 0.45 ms for each camera exposure. The  $O_2$  concentration in the water was in equilibrium with the air concentration during the measurement. The mean gray value seems to have periodic variations with a sawtooth-like behaviour, additional to the two-level noise effect. The effect is possibly due to a periodic shift of the camera exposure window relative to the laser pulse. Figure A.3(b) shows a similar measurement as depicted in Figure A.3(a), with the difference that the laser was in the continuous wave (cw) mode. In this mode, the sawtooth effect does not occur.

To correct for the sawtooth effect, the phase of the sawtooth would need to be detected in

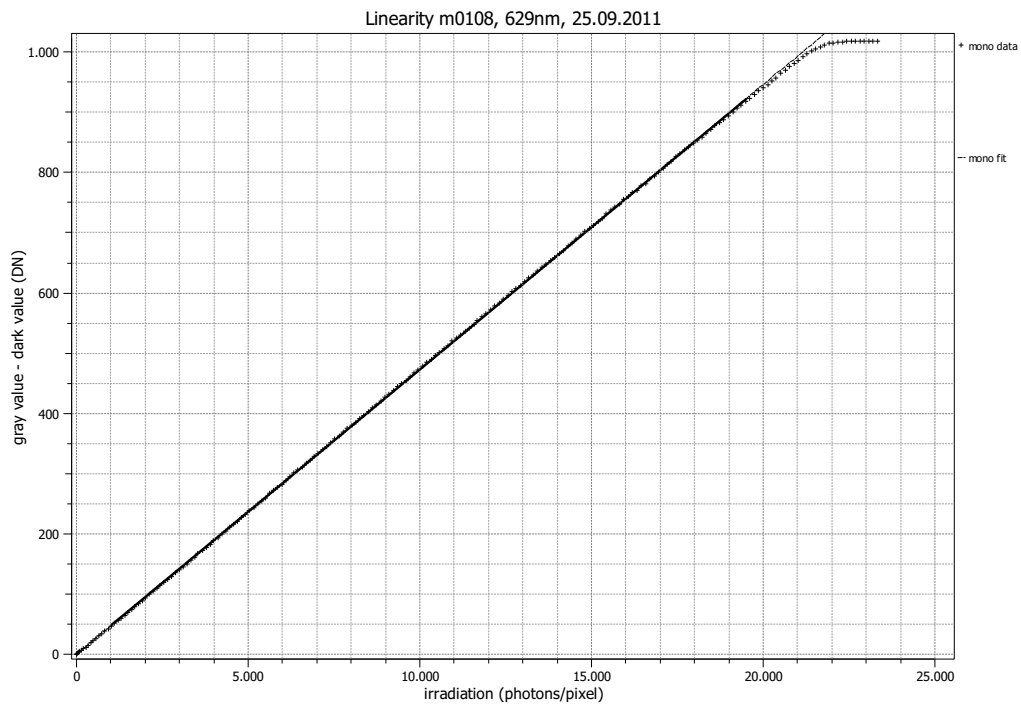
each image. This was not possible for the LIF measurements because variations of the intensity due to changes in the  $O_2$  concentration are higher than the variations due to the sawtooth effect. Even for LIF measurements recorded at a constant  $O_2$  concentration, the automatic detection of the phase was not possible because the frequency of the sawtooth showed variations. This effect can be eliminated in future measurements by using the camera in the “free run” mode and pulsing the laser with the camera output signal.

## A.5. Camera Response Calibration

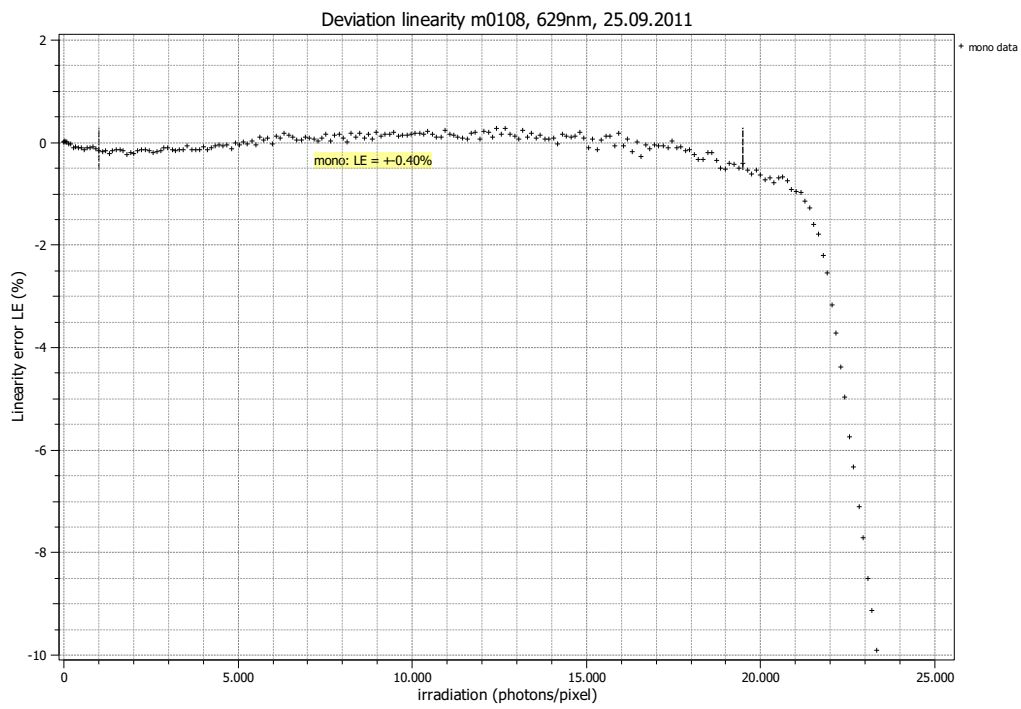
Measurements of the linear response of the camera used in this study, a *BASLER acA2000-340km* (see Section 4.2.4) were conducted at the HCI (Heidelberg Collaboratory for Image Processing) by Prof. Bernd Jähne according to the EMVA 1288 standard [Group, 2010].

Figure A.4(a) shows a measurement of the camera’s gray value depending on the irradiation (in photons per pixel). A significant deviation starts at an irradiation above 15000 photons per pixel. This fact was considered during the experiments by using only up to 80 % of the camera’s full range. Figure A.4(b) shows the deviation from the linearity response. The error in the range specified in the figure up to an irradiation of 19500 photons per pixel stays below 0.4 %.

A. Appendix



(a) camera signal with respect to the irradiation and a linear fit function



(b) deviation from the camera's linearity with respect to the irradiation

**Figure A.4.:** camera calibration

# Danksagung

An dieser Stelle möchte ich allen danken, die zum Gelingen dieser Arbeit beigetragen haben.

Mein besonderer Dank gilt Prof. Bernd Jähne für die Ermöglichung und Betreuung des interessanten Projektes in seiner Arbeitsgruppe. Danke für die vielen inspirierenden Anregungen, für die gegebenen Freiräume und die positive Arbeitsatmosphäre.

Ich bedanke mich ebenfalls herzlich bei Prof. Ulrich Platt für die Zweitkorrektur dieser Arbeit in der Weihnachtszeit. Bei Prof. Dirk Dubbers und Prof. Iring Bender danke ich, Teil des Prüfungskomitees zu sein.

Bei der gesamten Windkanal Arbeitsgruppe bedanke ich mich für den hilfsbereiten Umgang miteinander, die vielen fruchtbaren Diskussionen und die gute Stimmung. Danke an Günther Balschbach, Paulus Bauer, Maximilian Bopp, Patrick Fahle, Jonas Gliß, Heiko Heck, Alexandra Herzog, Daniel Kiefhaber, Nils Krah, Kerstin Krall, Christine Kräuter, Jakob Kunz, Wolfgang Mischler, Leila Nagel, Daniel Niegel, Roland Rocholz, Uwe Schimpf, Julian Stapf, Darya Trofimova, Björn Voss, Pius Warken und René Winter.

Roland Rocholz danke ich für die vielen hilfreichen Diskussionen über Gasaustausch, Prismen und Namensgebungen von Windkanälen und Konstanten. Danke auch für die Zusammenarbeit am linearen Kanal und das kritische und sorgfältige Korrekturlesen von vielen Teilen der Arbeit.

Bei Nils Krah bedanke ich mich für viele interessante Diskussionen, die durch sein großes physikalisches Interesse und seine schnelle Auffassungsgabe sehr wertvoll waren. Das genaue Korrekturlesen einiger Kapitel war ebenfalls sehr viel wert.

Christine Kräuter und Daniel Kiefhaber danke ich für die Bereitschaft, viele Kapitel der Arbeit Korrektur zu lesen. Daniel danke ich für viele kritische Kommentare, selbst in der Zeit während der Messkampagne im Pazifik. Danke Christine für die Unterstützung in den arbeitsintensiven Phasen mit ermunterndem Feedback.

Pius Warken danke ich für die gute Zusammenarbeit während seiner Diplomarbeit. In dieser Zeit wurden die Grundbausteine für meine Dissertation gelegt.

Bei Wolfgang Mischler bedanke ich mich für viele Diskussionen zur Optik und für das Programmieren von zahlreichen Gerätetreibern.

Alexandra Herzog danke ich für den Bau des linearen Kanals und für die Weitergabe von ihren Erfahrungen in der Anfangsphase meiner Dissertation.

Bei Cassandra Fallscheer bedanke ich mich für Sprachkorrekturen meiner englischen Arbeit von dem Schreiben der ersten Sätze an bis zu den letzten Abschnitten, die in verschlafenem Zustand geschrieben wurden.

Sami Al Najem und Sönke Schäfer danke ich für das Korrekturlesen von Teilen der Arbeit und die Aufmunterung zu Sport, auch in den arbeitsintensiven Phasen der Dissertation.

Allen nicht genannten Freunden danke ich für Ablenkung zu jeder Zeit, für unvergessliche gemeinsame Erlebnisse und für das Verständnis für mein häufiges auf die Uhr schauen in den letzten Monaten. Ganz besonderer Dank geht an meine Eltern für ihre Geduld, die mentale Unterstützung in den intensiven Phasen der Arbeit und die Förderung meiner Ideen.